Probing Topological Character and Fermi Surface of Topological Materials by Magnetotransport Measurements

AMIT VASHIST

A thesis submitted for the partial fulfillment of
the degree of Doctor of Philosophy

Department of Physical Sciences

Indian Institute of Science Education and Research (IISER) Mohali

Knowledge city , sector 81, SAS Nagar, Manauli PO, Mohali 140306, Punjab, India

October 2019

Dedicated to
my family

Declaration

The work presented in this thesis has been carried out by me under the guidance of Dr. Yogesh Singh at the Indian Institute of Science Education and Research Mohali. This work has not been submitted in part or in full for a degree, a diploma, or a fellowship to any other university or institute. Whenever contributions of others are involved, every effort is made to indicate this clearly, with due acknowledgment of collaborative research and discussions. This thesis is a bonafide record of original work done by me and all sources listed within have been detailed in the bibliography.

Amit Vashist
(Candidate)

In my capacity as the supervisor of the candidate's thesis work, I certify that the above statements by the candidate are true to the best of my knowledge.

Dr. Yogesh Singh
(Supervisor)

Acknowledgments

First of all, I would like to thank my thesis supervisor Dr. Yogesh Singh for providing me the opportunity to work under his guidance. His constant support and encouragement helps me at various stages of my graduate studies.

I would also like to thank my doctoral committee members, Dr. Sanjeev Kumar and Dr. Gautaum Sheet for their valuable suggestions. I would like to thank my collaborators Dr. S. Chakraverty, Dr. Divya Srivastava and Dr. M. Karppinen. I am very thankful to my primary school teacher Nirmala, who motivated and guided me a lot.

I would like to acknowledge XRD facility, Raman facility and SEM facility of IISER Mohali. I am thankful to Inderjit and Vivek for helping me in using the EDX facility. I thank Dr. Angshuman Roy Choudhury for SC XRD characterization of our grown single crystal samples.

I am very thankful to IISER Mohali for the generous financial support during my Ph.D. I would like to acknowledge IISER Mohali and DST India providing financial assistance for attending the SCES-2019 in the Japan.

I am very thankful to Dr. R.K. Gopal for very fruitful discussion on topological materials. I would like to thank Dr. Arnab Pariari for prompt answering my questions on research gate. I am grateful to my seniors Kavita and Aswini for introducing me various research facilities available in Novel materials Lab. I am very thankful to my friend and labmate Anzar Ali for all the discussions and support in the lab and outside the lab.

I would like to thank other previous and existing members of Novel Material Lab : Shama Monga, Pardeep Tanwer, Jaskaran Singh, Ankit Labh, Dr. Gyaneshwar, Anooja, Prins, and Kavita Chaodary for their cooperation and help in the lab and ouside the lab.

I would also like to thank my batchmates and friends Shelender Kumar, Shekhar Das, Mohammad Aslam, Anirban, Ankit, Avinash, Sudhansu, Arnab, Ramu Kumar Yadav, Shailesh, Mohd Balal, Mayank, Shubendu, Guratinder Kaur, Anshu Sirohi, Jyotsana Ojha, Harleen Kaur, Leena Agarwal, Sumit Mishra, Ritesh Kumar, Shyam Sundar Yadav, Sandeep Howladar, Soumya Datta, Soumyadip Haldar, Suman Kamboj, Aastha, Priyanka, Avtar, Inderjeet, Vivek and all others for their help and making my years enjoyable at IISER Mohali. I also want to thank my college and school time friends, Pushpa Kumari, Vijay, Sandeep, Sandeep Rana, Pawan, Amit, Baljeet, Ghansyam, Sandeep Gulia, Virender, Jitender, Rajesh, Jaiparakash and all others.

I am extremely grateful to my mother and my father for their selfless love, for showing faith in me and giving me liberty to choose what I desired. This work would not have been possible without their blessings and support. Also, I express my thanks to my younger brother Sumit Vashist for his love and support. Finally, I would like to thank my wife Neeru Sharma for her eternal support and encouragement in the final part of my thesis.

Abstract

Condensed matter physics has taken an exciting turn after the theoretical prediction and experimental realization of two and three dimensional (2D/3D) topological quantum materials, possessing a nontrivial bulk band structure characterized by topological invariants. The discovery of these quantum materials has been inspired by the fundamental concept of bulk boundary correspondence in quantum Hall effect, which is considered as first topological state of matter. This new state of matter includes many variants such as, topological insulators (TIs), Weyl and Dirac semimetals (DSMs/WSMs) and topological superconductors (TSCs). Topological insulators(TI) exhibit insulating behaviour in the bulk having conducting edge/surface states. The 2D dispersion of these Dirac states in the bulk gap forms a cone on the surface and is known as surface Dirac cone. These edge/surface states expected to be immune against scattering from non magnetic disorder and hence could be useful for spintronics devices. Topological (Dirac or Weyl) semimetals (DSM, WSM), which possess bulk bands with linear electronic dispersions in all three momentum directions, have attracted immense research interest, recently. In DSMs, doubly degenerate Dirac cones (of opposite chirality) exist and they are protected by time reversal (TRS) and inversion (IS) symmetry. If any of the above symmetries breaks that will leads to a splitting of the Dirac cones into a pair of Weyl cones with opposite chirality, thus transforming a DSM into a WSM. Topological semimetals (TSMs) are further categorized as type-I and type-II TSMs. Type-I TSMw have linear and isotropic dispersion in momentum space, while dispersion relation in type-II semimetals is tilted in a perticular momentum direction. These topological materials have been shown to exhibit exotic physical properties like extremely large magnetoresistance (MR), high mobility, small effective mass, small carrier density, negative magnetoresistance, a large value of the anomalous Hall/thermal conductivity and a Berry phase of π . In addition to TSMs, topological superconductors (TSCs) have been the focus of intense recent research due to the possibility that these materials may host Majorana fermion excitations. These Majorana excitations are of fundamental as well as technological interest and can also be utilized in fault-tolerant Quantum computation.

In this thesis, we present magnetotransport, high pressure and thermal property investigation of some topological materials. These materials include the topological insulator $Bi_{1-x}Sb_x$, topological semimetals ATe_2 (A = Pt, Pd), XBi (X = La, Pr) and a topological superconductor candidate Pd:Bi_2Te_3. Our work on these materials uncovers several interesting results: (i) observation of a strong Weyl state in the TI regime in $Bi_{1-x}Sb_x$, (ii) experimental evidence for DSM nature of ATe_2, additionally, the planar Hall effect (PHE), observed for $PtTe_2$ even though the Dirac node is 0.8 eV away from the Fermi level, (iii) first experimental realization of the topologically nontrivial state in PrBi, (iv) our heat

capacity measurements strongly indicate that the superconductivity in $PdTe_2$ is conventional in nature despite the presence of topologically nontrivial electrons contributing to the transport, (v) evidence for unconventional superconductivity in topological superconductor candidate Pd:Bi_2Te_3.

List of publications:

1. *Fermi surface topology and large magnetoresistance in the topological semimetal candidate PrBi*
   Amit Vashist, R. K. Gopal, Divya Srivastava, M. Karppinen, Yogesh Singh,
   Phys. Rev. B 99, 245131 (2019).

2. *Heat capacity evidence for conventional superconductivity in the type-II Dirac semimetal $PdTe_2$*
   Amit and Yogesh Singh,
   Phys. Rev. B 97, 054515 (2018).

3. *Type-II Dirac semimetal candidates ATe_2 (A= Pt, Pd): A de Haas-van Alphen study*
   Amit, R. K. Gopal and Yogesh Singh,
   Phys. Rev. Materials 2, 114202 (2018).

4. *The H-T and P-T phase diagram of the superconducting phase in Pd:Bi_2Te_3*
   Amit and Yogesh Singh,
   J Supercond Nov Magn (2016).

5. *The de Haas-van Alphen Effect Study of the Fermi Surface of LaBi*
   Amit Vashist, R. K. Gopal and Yogesh Singh,
   JPS Conf. Proc. 30, 011019 (2020).

6. *Observation of Chiral character deep in the topological insulating regime in Bi(1-x)Sbx*
   Amit Vashist, R. K. Gopal and Yogesh Singh,
   arXiv:1803.03825v1..

7. *Observation of planar Hall effect in Type-II Dirac semimetal $PtTe_2$*
   Amit Vashist, R. K. Singh, Neha Wadehra, S. Chakraverty, Yogesh Singh,
   arXiv:1812.06485.

8. *Conventional superconductivity in the type-II Dirac semimetal $PdTe_2$*
   , Shekhar Das, **Amit**, Anshu Sirohi, Lalit Yadav, Sirshendu Gayen, Yogesh Singh and Goutam Sheet,
   Phys. Rev. B 97, 014523 (2018).

9. *Mixed type I and type II superconductivity due to intrinsic electronic inhomogeneities in the type II Dirac semimetal $PdTe_2$*
   Anshu Sirohi, Shekhar Das, Priyo Adhikary, Rajeswari Roy Chowdhury, **Amit Vashist**, Yogesh Singh, Sirshendu Gayen, Tanmoy Das and Goutam Sheet,
   Journal of Physics: Condensed Matter (2018).

Contents

List of Figures

List of Tables

CHAPTER 1

General Introduction

1.1 Topology and Integer Quantum Hall Effect

Last decade has witnessed the theoretical prediction and experimental realization of 2D and 3D topological phases of matter [1, 2, 3]. These topological phases must be characterized by topological invariants. In mathematics, topology deals with the properties of geometrical objects that remains invariant under continuous deformation. For example, a sphere can be continuously transformed into an ellipsoid, so they are topologically equivalent. In a similar way, a coffee mug is topologically equivalent to a doughnut. But a sphere and a doughnut belong to different topological class and can be distinguished by a topological quantity known as genus (g). The genus of an object can be calculated by Gauss-Bonnet's theorem,

$$\frac{1}{2\pi}\int_{Surface} KdS = 2-2g, \tag{1.1}$$

here K is the Gaussian curvature. Gaussian curvature for a sphere of radius r can be defined as, K = $\frac{1}{r1r2}$, and this gives total curvature $\int_{Surface} KdS = 4\pi$. This suggests that for a sphere g is zero. A sphere can be continuously deform into an ellipsoid, and the value of g remains the same. Therefore, g is invariant under small and continuous transformation, and is known as topological invariant. Similar concepts apply to the band structures of electronic states of matter.

Before the experimental realization of integer quantum Hall effect (IQHE) in 1980 [4], the states of matter in condensed matter physics could be categorized by the principle of symmetry breaking. For example, according to Landau-Ginzburg theory [5], crys-

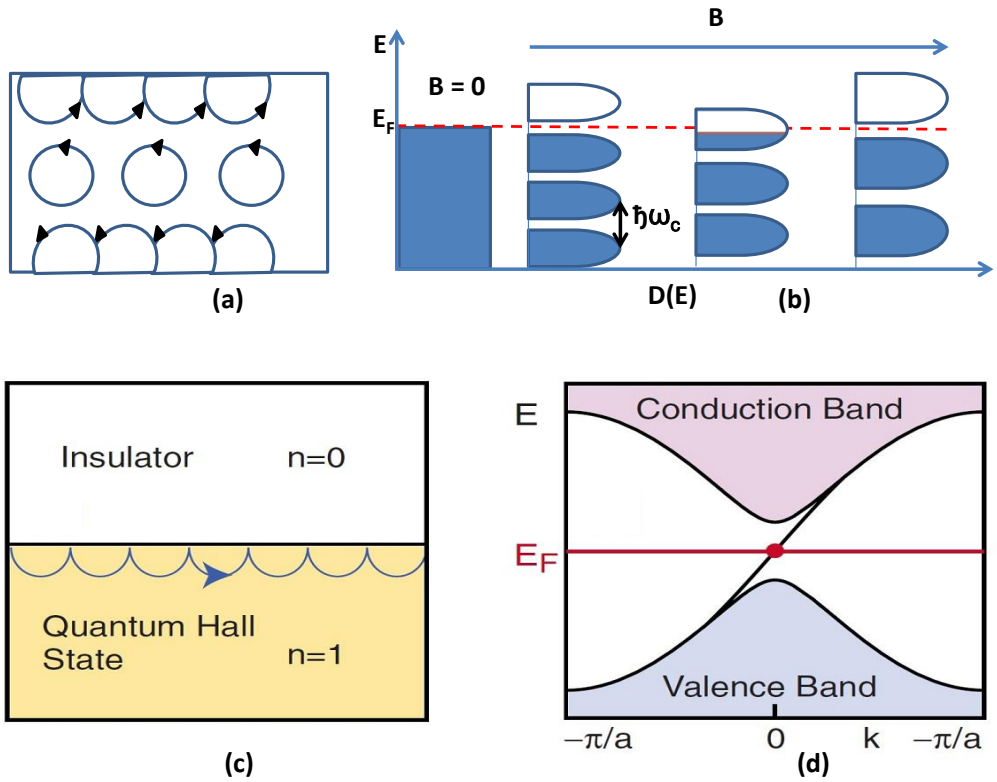

Figure 1.1: (a) Schematic of a 2D electron gas when magnetic field is applied normal to the plane of the material. (b) The emergence of Landau level and variation of the density of states across the Fermi level with the change in the magnetic field. (c) The skipping cyclotron orbit at the interface of trivial insulator and quantum Hall state. (d) A single chiral edge state which connects the valence band to the conduction band. (c), (d) Reprinted from **Rev. Mod. Phys. 82, 3045 (2010).**

talline solids breaks translational symmetry, a ferromagnet breaks rotational symmetry and a superconductor breaks guage symmetry. The symmetry breaking leads to the order parameter, which has finite value only for ordered state. IQHE can be considered as the first example of topological insulator realized without spontaneous symmetry breaking. The quantum Hall (QH) effect occurs, when an out of plane magnetic field is applied to a two dimensional electron gas. At low temperature the electrons orbit get quantized, which leads to Landau levels with energy $E_n = (n+1/2)\ \hbar\omega_c$, as shown in Figure 1.1 (b), here $\omega_c = eB/m^*$ is known as cyclotron frequency and m^* is called effective mass of carriers. The N^{th} and $(N+1)^{th}$ Landau levels are separated by energy $\hbar\omega_c$. Let us assume that N Landau levels are completely filled and others are empty. If chemical potential μ lies in between the filled and empty Landau level this condition is similar to that of an insulator. However, charge carriers at the edge of the sample form skipping orbits, as shown in figure 1.1 (a). This chiral flow of electrons at the edges lead to the finite value

of Hall conductivity (σ_{xy}) and for N filled Landau levels σ_{xy} gets quantized given by the expression,

$$\sigma_{xy} = N\frac{e^2}{h}. \tag{1.2}$$

Interestingly, the quantization in σ_{xy} can be measured to an accuracy of 1 part in 10^9.

The concept of the Berry phase [6] is very essential in the discussion of topological states of matter. It is a geometric phase acquired by a quantum state during an adiabatic cyclic process. The Bloch states $\mid u_m(k) >$, which are eigen states of Bloch Hamiltonian H(k) are invariant under the transformation, $\mid u_m(k) > \rightarrow e^{\imath\phi(k)} \mid u_m(k) >$, where k is crystal momentum in reciprocal space. This transformation calls a quantity which resembles to the electromagnetic vector potential and known as Berry connection, A_m = -$\imath$ $< u_m(k) \mid \nabla_k \mid u(k) >$. Under gauge transformation A_m transform as $A_m \rightarrow A_m + \nabla_k\ \phi(k)$, similar to electromagnetic vector potential. It also invites a gauge invariant quantity similar to magnetic flux given by $F_m = \nabla_k \times A_m$, known as Berry curvature. Now for a closed loop C, Berry phase in momentum space is defined as,

$$\gamma_c = \oint_C A_m.dk = \int_S (\nabla_k \times A_m).d^2k = \int_S F_m.d^2k. \tag{1.3}$$

The Berry has some important properties. First, Berry phase is gauge invariant quantity which makes it physically observable quantity. Second, the Berry phase for a gapless Dirac band structure is a fixed number of π. Third, it a geometric phase.

The topological perspective of QHE was explained by Thouless, Kohmoto, Nightingale and den Nijs (TKNN) [7]. TKNN realized that if we integrate the Berry curvature of a band over the Brillouin zone the result will be an integer number,

$$\int_{B.Z.} F_m.d^2k = n_m, \tag{1.4}$$

and this integer is called first Chern number. The total Chern number determined by summing the Chern number of all occupied bands is given by, n = $\sum_{m=1}^{N} n_m\ \varepsilon$ Z (where Z represents integers). The Chern number n is a topological invariant quantity also known as TKNN invariant. TKNN calculated that n is the same integer as was observed in Hall resistance, σ_{xy} = n$\frac{e^2}{h}$. It is not possible to change topological invariant quantity n under smooth deformation of a Hamiltonian. The edge states appear at the interface of QH state and a trivial band insulator (Figure 1.1 (c)) is a fundamental consequence of topological classification of the gapped band structure. These sates are chiral because they flow in one direction along a particular edge. Chiral edge states are immune to disorder due to absence of states required for backscattering and that's why Hall resistivity is precisely quantized. Topological classification separates a quantum Hall state (n = 1) from a trivial

insulator state (n = 0). In order to change the topological invariant (n), the gap has to close somewhere between a TI and trivial insulator. Therefore smooth transformation of Hamiltonian from topologically trivial to non trivial state is not possible. The bulk-boundary correspondence relates the no. of edge channel to the change in Chern number across the interface of two different topological materials, $N = \Delta n$ [1].

1.2 Quantum Spin Hall effect/2D Topological Insulators

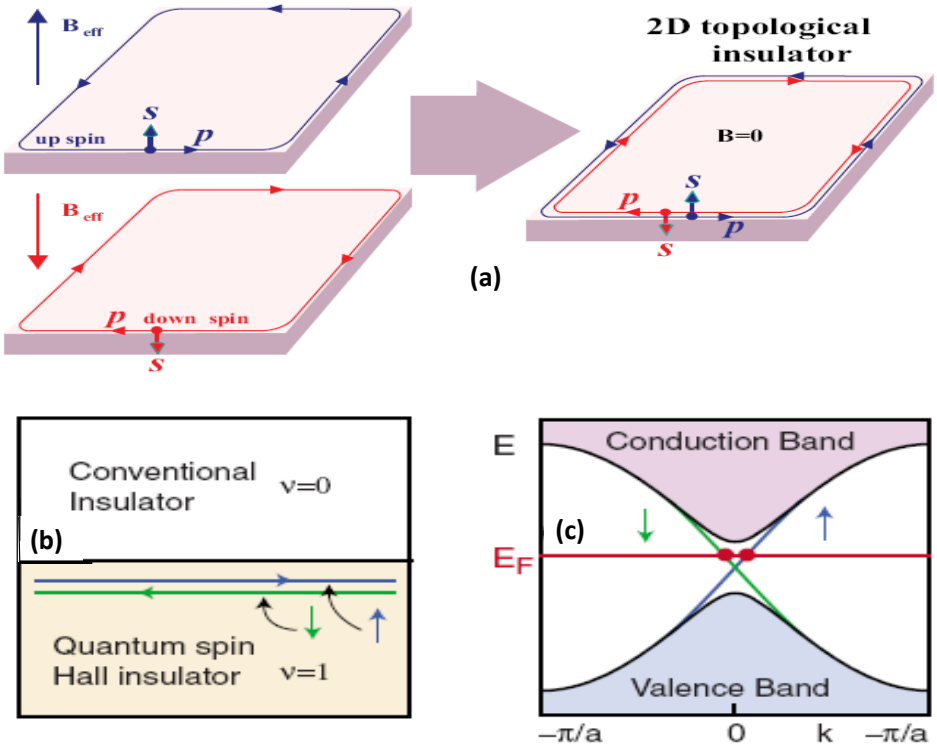

Figure 1.2: (a) Schematic representation of a QSH insulator as a superposition of two QH states. (a) Reprinted from **G. Tkachov, Topological insulators: The physics of spin helicity in quantum transport (Pan Stanford, 2015).** (b) Edge states at the interface between QSH insulator and a conventional insulator. (c) The edge state dispersion, in which up (blue arrow) and down spins(green arrow) moves in opposite directions. (b), (c) Reprinted from **Rev. Mod. Phys. 82, 3045 (2010)**.

The dissipation-less edge states realized in QHE required high magnetic field and low temperature, which limit its potential applications. Is this possible to obtain such dissipation-less edge states at room temperature without applying external magnetic field? Kane, Mele in 2005 and Bernevig, Zhang in 2006 independently proposed that such states can be realized in some theoretical models with high spin orbit coupling [8, 9]. The spin

orbit coupling in QSH system plays an analogous role to the magnetic field played in QH system. The intrinsic Spin orbit coupling can be considered as an effective magnetic field B_{eff} which acts in the opposite direction for up and down spin. Thus a QSH state can be considered as a superposition of two QH state with up and down spins, as shown in figure 1.2 (a). The edge dispersion of spin non degenerate states moving in the opposite direction is shown in figure 1.2 (c). The net flow of charge in QSH insulator is zero, however, there is finite spin current. QSH insulators are also known as 2D topological insulators (TIs). The spin non degenerate edge states appear in QSH insulator are immune to non magnetic impurity. These states are protected from backscattering by time reversal symmetry. A QSH edge state can be represented by

$$H = \hbar v_f \sigma_x k_y, \tag{1.5}$$

where v_f is Fermi velocity, σ_x is x component of the Pauli spin matrices and k_y is reciprocal lattice vector. Time reversal operator does two things, first, it flip the up spin to down spin and vice-versa. Second, it changes the sign of k vector. The Hamiltonian (eqn.1.5) of a QSH edge state remain invariant under the action of time reversal operator. The insensitivity of edge states towards non magnetic impurity can be explained by following way. Let us consider that an electron in QSH edge state encounters an impurity, it can take clockwise or counterclockwise turn around an impurity, and this turn rotates its spin by an angle π or -π in reverse direction. Now according to time reversal symmetry, these two paths are differed by π - (-π) = 2π. According to quantum mechanics, the wave function of spin 1/2 particle acquired a -ve sign after a 2π rotation (i.e. ψ changes to - ψ). Therefore two backscatter path interfere destructively, hence perfect transmission. However, time reversal symmetry is not preserved for magnetic impurities and two paths will no longer interfere destructively [10].

The TKNN invariant for QSH insulator is zero because it is equal and opposite for up and down spin (n $\uparrow$ = - n $\downarrow$). For QSH insulator, a new topological invariant (ν) was introduced by Fu and Mele and others [11, 12]. This invariant can be either 0 or 1 and thus named as 'Z_2 topological invariant'. For an antisymmetric matrix $\omega(\Gamma_a)$, where $\Gamma_{a=1,2,3,4}$ are high symmetry points in the Brillouin zone of two dimensional electronic system one can define a quantity $\delta_a = \frac{Pf[\omega(\Gamma_a)]}{\sqrt{Pf[\omega(\Gamma_a)]}} = \pm 1$. Pfaffian for any skew symmetric matrix A can be defined as $Pf(A)^2 = det(A)$. The topological invariant ν can be calculated by the expression,

$$(-1)^{\nu} = \prod_{a=1}^{4} \delta_a. \tag{1.6}$$

$\nu = 0$ represents a topological trivial state or a conventional insulator, and $\nu = 1$ represents a topological non trivial state or a QSH insulator, as shown in figure 1.2 (b). Experimentally QSH state was first realized in HgCdTe quantum well structures [13].

1.3 3D Topological Insulators

After the discovery of QSH insulator (or 2D TI), its 3D analogue was predicted and named as three dimensional topological insulator (3D TI) [14, 15, 16]. 3D TIs exhibit insulating behavior in bulk, but have conducting surface states. These surface states disperse linearly in the bulk bend gap, forming a 2D surface Dirac cone. This is shown in figure 1.3 (b). The most peculiar property of surface sates is their spin momentum locking, which is called helical spin polarization. They are helical in the sense that spin of the electron is locked perpendicular to the momentum vector. The real space picture of spin momentum locked surface states are shown in figure 1.3 (a). The helical surface states can be represented by a effective Hamiltonian,

$$H = \hbar v_f(\sigma_x k_y - \sigma_y k_x). \tag{1.7}$$

The gapless nature of 2D surface states are protected by TRS. In real materials 3D TIs are initially predicted in $Bi_{1-x}Sb_x$ and strained HgTe [17]. Experimentally it was first realized in $Bi_{1-x}Sb_x$ [18]. However, it was realized that this material is not very suitable for detailed study of the helical surface state due to its complex band structure. The Second generation of 3D TIs including Bi_2Se_3, Bi_2Te_3 and Sb_2Te_3 having a single Dirac cone on the surface has been predicted and verified experimentally [19, 20, 21, 22, 23].

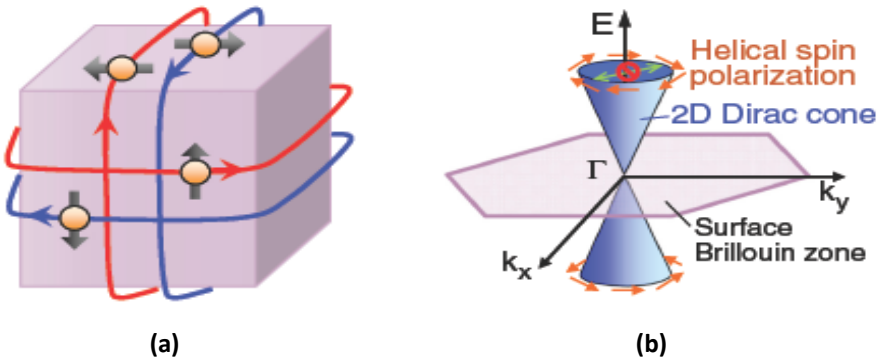

Figure 1.3: (a) Schematic representation of spin momentum locked surface states of 3D TI in real space. (b) Energy dispersion of surface states forming a 2D Dirac cone. Reprinted from **Journal of the Physical Society of Japan 82, 102001 (2013)**.

3D TIs are characterized by four Z_2 topological invariants $(\nu_0,\nu_1\nu_2\nu_3)$. Where ν_0

represent strong topological index and $\nu_1\nu_2\nu_3$ are weak topological indices. If all four invariants are zero (ν_0,$\nu_1\nu_2\nu_3$ = 0, 000), then the system behaves like a conventional band insulator. If the strong topological index ν_0 = 0 and one or more weak indices are non zero (ν_1 + ν_2 + $\nu_3 \neq 0$) then the system is known as a weak topological insulator. A weak TI can be constructed by stacking the layers of 2D TIs. The indices $\nu_1\nu_2\nu_3$, can be interpreted as Miller indices to indicate the orientation of layers. The strong topological invariant is defined as

$$(-1)_0^{\nu} = \prod_{a=1}^{8} \delta_a, \tag{1.8}$$

where "a" represents the TRIM points in 3D reciprocal space. For strong 3D TIs the value of ν_0 is found to be one. The bulk band structure of strong TI is consist of odd number of Dirac cones.

1.4 Topological Semimetals

Successful prediction and realization of TIs and band structure of graphene have motivated the search for other topological phases of matter. In graphene and TIs, the charge carriers are restricted to move in two dimensions. Graphene is considered to be a topologically trivial material due to presence of even number of Dirac cone. Graphene can be gapped, or charge carrier can be localized by small disorder or perturbation. The Recent discovery of topological semimetals (TSM), also known as 3D analog of graphene, has reinforced the search for this state of matter in various magnetic and nonmagnetic stoichiometric materials [2, 24, 25, 26, 27]. Dirac/Weyl semimetals (DSM/WSM) are TSMs having linear bulk band dispersion in all three-momentum directions. Due to their unique bulk band structure, these TSMs have been shown to exhibit exotic physical properties like such as extremely high magnetoresistance, non-Ohmic transport, Fermi arc surface states, high mobility, negative magnetoresistance, nonlocal conduction and a Berry phase of π [28, 29, 30].

1.4.1 Dirac Semimetals

A 3D DSM state was predicted and realized at a quantum critical between a band insulator and a TI [17, 31, 32]. Figure 1.4 (a) illustrates the band inversion mechanism, which provides a simple route to observe a DSM state. A topological insulator state can be tuned by doping and by strain. These parameters change the spin-orbit coupling in the system and may change the parity of conduction and valence band. At a quantum critical point, the gap between conduction and valence band closes, and massless DSM state is realized. The quantum critical point at which these two band touches is known as

Dirac node. The dynamics of massless quasiparticle (known as Dirac Fermions) can be described by a Hamiltonian,

$$H\psi = \begin{pmatrix} \hbar v_F \sigma.k & 0 \\ 0 & -\hbar v_F \sigma.k \end{pmatrix} \psi. \tag{1.9}$$

Where v_F, σ and k represent Fermi velocity, Pauli matrices and momentum vector respectively. Since Pauli matrices are 2×2 matrices, H in equation 1.9 is a 4×4 martrix.

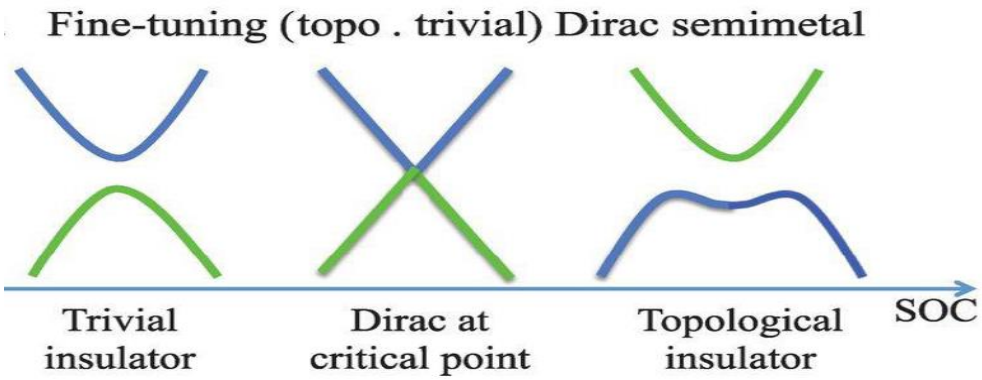

Figure 1.4: A 3D Dirac semimetal state can be realized by tunning a system to the critical point between a trivial insulator and topological insulator. Reprinted from **Science 347, 294 (2015)**.

Experimentally a 3D DSM state at a quantum critical point is realized in the number of compounds such as $BiTl(S_{0.5}Se_{0.5})_2$, $(Bi_{0.94}In_{0.06})_2Se_3$, $Bi_{0.96}Sb_{0.04}$ [18, 33, 34]. However, Dirac point in these type of semimetal is unstable because a small variation of external parameter away from the critical point will open a gap. It has been predicted that If rotational symmetry along with time reversal and inversion symmetry is taken into account, it can cause stable Dirac point [2, 26, 35]. Following the theoretical prediction, stable 3D DSM state has been realized in Na_3Bi and Cd_3As_2 [24, 36]. In these compounds, 3D Dirac points are stabilized by C_3 and C_4 rotational symmetry, respectively.

1.4.2 Weyl semimetals

In 1929, Hermann Weyl solved massless Dirac equation (1.9) by reducing it from four component to two components equation: [37],

$$H\psi = \pm c\vec{\sigma}.\vec{p}\psi, \tag{1.10}$$

above equation describes the two types of fermions with opposite chiralities, denoted by $\pm$ c. The particles known as Weyl fermions have definite spin-momentum projection. The

helicity operator h = $\vec{\sigma}.\vec{p}/|p|$ defines the projection of spin to momentum vector, have two eigen values $\pm$ 1. For massless fermions, helicity is same as the chirality. WSMs are class of a TSMs whose low energy quasiparticle excitations are Weyl fermions [38, 39]. Fig. 1.5 (a) and (b) shows that a DSM can be transformed into a WSM by breaking time reversal or inversion symmetry (IS). TRS can be broken by either applying a magnetic field or by introducing magnetic impurities in the system. If IS is preserved and TRS is broken, minimal number (two) of Weyl nodes of opposite chirality are allowed. On the other hand, If TRS is preserved and IS is broken then the total number of Weyl points must be in a multiple of four. WSMs are topological in nature in the sense that Weyl nodes are immune to small disorder and may only vanish by annihilation with other Weyl node of opposite chirality. Another important feature of the WSM state is the presence of the disjoint surface Fermi arcs, connecting the two Weyl nodes. The first theoretical prediction of the WSMs was reported in TaAs, TaP, NbAs, and NbP [27, 40] and subsequently experimentally realized in TaAs family of materials [41, 42] by Angle-resolved photoemission spectroscopy (ARPES). TSMs are further categorized into type-I or type-II DSMs/WSMs, depending on the nature of the bulk Dirac dispersion relation. While type-I has linear and isotropic dispersion relation in the momentum space, the dispersion relation in the type-II TSMs is tilted. This occurs when kinetic energy term (T(k)) becomes greater than potential energy term (U(k)) in certain momentum direction, a tilt appears in Dirac/Weyl cone. The tilted nature of Dirac/Weyl cone has been predicted and experimentally verified in large number of materials such as in $PdTe_2$, $PtTe_2$, $MoTe_2$ and $TaIrTe_4$ [43, 44, 45, 46, 47, 48]. Types-II WSMs are known to exhibit some special properties which includes Klein tunneling, field dependent chiral anomaly and anomalous Hall conductivity [49, 50, 51].

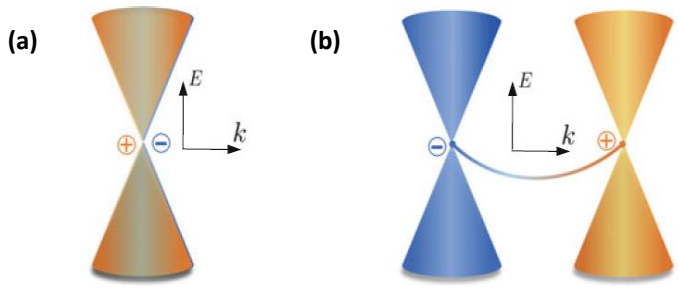

Figure 1.5: (a) Dirac semimetal with degenerate positive and negative chiralities fermions. (b) Weyl semimetal with positive and negative chiralities fermions are at different positions in k - space. Reprinted from **Topological Insulators (Springer, 2017)**.

1.5 Quantum Transport in Topological Semimetals

1.5.1 Fermi arc surface states

Surface states are generally associated with insulators. However, surface states can also be defined for gapless systems (WSMs/DSMs). The surface state of WSM is different from close contour surface states of 3D TI (figure 1.6 (a)). The Fermi surface of WSM is half of the usual Fermi circle which lies on one surface, with another half lies on the opposite surface (figure 1.6 (c)). The Fermi arc surface states observed on the surface of a WSM is a direct manifestation of the fact that Weyl nodes of opposite chirality are source and sink of Berry curvature in momentum space. If we consider Weyl nodes at $\pm$ k_0 then energy gap closes at these points, but in the region of $-k_0 < k < +k_0$, system behave as a quantum Hall insulator whereas outside this region, such a system can be well described as a trivial insulator. The Fermi arc surface states appear in QH phase and become ill defined at two Weyl nodes($\pm$ k_0). These Fermi arc surface state has been directly observed in TaAs family of compounds by angle dependent angle resolved photoemission spectroscopy (ARPES) and scanning tunneling microscopy (STM) studies.

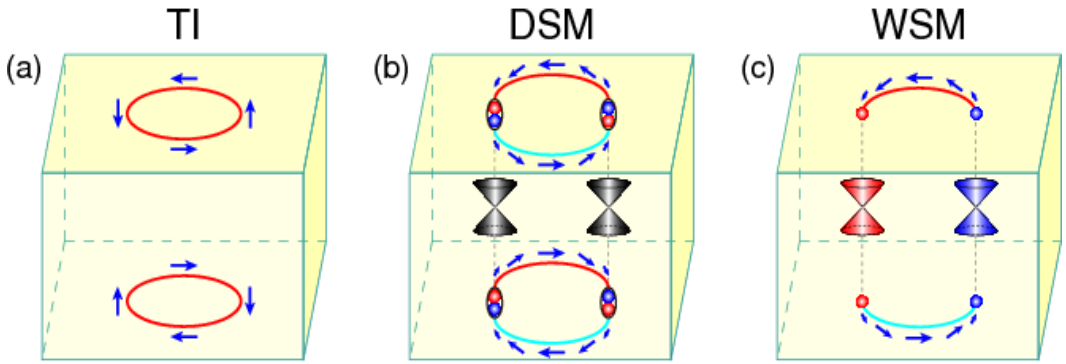

Figure 1.6: (a) Schematic diagram of the Z_2 protected two dimensional spin-polarized Dirac states on a boundary of a 3D TI. The spin polarization of surface states is indicated by the blue arrow. Fig.(b) depicts electronic structure of a DSM with spin-polarized surface Fermi arcs connecting two bulk Dirac nodes traversing through the three dimensional bulk Dirac cone. (c) In a WSM spin-polarized Fermi arcs are disjoint in nature, unlike closed ones in the DSM, connecting the Weyl nodes of opposite chirality in the bulk. Reprinted from Reprinted from **Phys. Rev. Lett. 115, 217601 (2015)**.

The surface state realized in DSMs Na_3Bi and Cd_3As_2 is called double Fermi arc [42, 52]. These Fermi arc states play a crucial role in the the dynamics of Dirac/Weyl fermions under applied magnetic field. It has been theoretically predicted that under external magnetic field electron can move in a cyclotron orbit which can connect one Fermi arc to the opposite Fermi arc through bulk nodes. Such a cyclotron orbit manifest itself by

an extra frequency in quantum oscillations, whose 2D character can be determined by the angle dependence of oscillations frequency (F $\propto$ 1/cos(θ)). To realize such a cyclotron orbit (or Weyl orbit), it is essential to reduce the size of the sample to reduce the contribution of the bulk states. These orbits have been experimentally observed in Cd_3As_2 nanostructure and WTe_2 [53, 54].

1.5.2 Large transverse magnetoresistance and high mobility

Dirac and Weyl semimetals usually exhibit extremely large magnetoresistance (XMR), when the magnetic field is applied normal to the direction of the current. Magnetoresistance (MR) is defined as a change of resistivity under magnetic field normalized by zero field resistivity (MR = [ρ(B) - ρ(0)]/ρ(0)). It has been observed that MR can reach upto 10^6 % at low temperature (0.3 - 2 K) and high magnetic fields [55, 56]. MR in TSMs usually shows power law field dependence (MR $\propto$ B^n) with n ranging from one to two. Some mechanisms are proposed to explain XMR in TSMs. One of these mechanism is electron - hole compensation i.e. number of electrons (n_e) is equal to the number of holes (n_h). As electron - hole compensation is found in multiband semimetals, simplified two band model is widely used to describe the longitudinal resistivity given by,

$$\rho_{xx} = \frac{B}{e}\frac{(n_h\mu_h + n_e\mu_e) + (n_e\mu_e\mu_h^2 + n_h\mu_h\mu_e^2)B^2}{(n_h\mu_h + n_e\mu_e)^2 + (n_h - n_e)^2(\mu_h\mu_e)^2B^2}. \tag{1.11}$$

Where n_e, μ_e and n_h, μ_h are carrier density and mobility of electrons and holes respectively. When n_e = n_h and mobility is high, equation (1.11) results in non saturating quadratic field depended XMR (MR $\propto$ B^2). A large linear MR could also be observed in TSMs and other materials. Two mechanisms are proposed to explain linear MR. First, linear MR could arise due to mobility fluctuation which has been observed in disordered $Ag_{2\pm\delta}Se$ and $Ag_{2\pm\delta}Te$ [57]. Second mechanism is the Abrikosov theory [58]. A Linear MR is expected in linear band touching materials when the lowest Landau level is partially field, and others are empty. TSMs are known to show very high mobility. The high mobility in TSMs can be understood by its relation with relaxation time τ and effective mass m^* by μ = eτ/m^*. Effective mass in TSMs can be calculated by quantum oscillations. It has been observed that effective mass (m^*) is very small for TSMs. Such massless behaviour is expected for Dirac fermions due to linear band dispersion. It is also observed that backscattering of the Dirac fermions in topological systems is suppressed by non trivial band topology, which leads in large relaxation time (τ). Therefore a small effective mass and large relaxation time favour high mobility in TSMs.

1.5.3 Chiral anomaly

Chiral anomaly is the most intriguing property of the WSMs. The chiral anomaly in condensed matter physics is analog of Adler-Bell-Jackiw anomaly in particle physics [59, 60]. Chiral anomaly is defined as nonconservation of chiral charge. In the presence of electric field (E) and magnetic field (B) the number of charge carriers in the neighborhood of Weyl nodes of opposite chirality is modified via the equation

$$\frac{dn^{3D}_{R/L}}{dt} = \pm\frac{e^2}{h^2}E.B. \tag{1.12}$$

This equation suggest that carrier density at an individual Weyl node is not conserved, which leads to non conservation of chiral electric charge. This imbalance of charge carriers at individual Weyl nodes causes extra flow of current in the direction of the applied electric field and results in negative longitudinal magnetoresistance (NMR). This chiral anomaly induced NMR is very sensitive to angle between E and B. The NMR is expected to exhibit largest amplitude when B $\parallel$ E and is suppressed as angle between B and E increases. The NMR induced by chiral anomaly was first observed Dirac semimetal $Bi_{0.97}Sb_0.03$ [61]. When the magnetic field is applied, a DSMs is transformed into a WSMs. Chiral anomaly has been observed in several WSMs/DSMs such as TaAs, NbP, Cd_3As_2, Na_3Bi [29, 62, 63, 64]. Observation of chiral anomaly induced NMR can be considered as a smoking gun signature of a Weyl state. However, NMR may also appear due to a classical effect known as current jetting. In this effect, current mainly flows in high conductance direction. This effect is strong in the materials that own large field induced conductance anisotropy. The current jetting effect can be minimized by using a perfect bar shape single crystal with collinear and well separated voltage contacts. In addition to NMR, the chiral anomaly may also lead to an unconventional version of the Hall effect, known as planar Hall effect (PHE) [65].

1.6 Topological Superconductors

Topological superconductors (TSCs) have been the focus of intense recent research [3]. TSCs are interesting because of the possibility that they may host Majorana fermion excitations [66, 67]. These Majorana excitations are of fundamental as well as technological interest and can also be utilized in fault-tolerant Quantum computation. Majorana fermion, theoretically predicted in 1937 [68], remain elusive as an elementary particle. These exotic chargeless particles are their own antiparticles. Initially, the neutrino was considered to be a Majorana fermion. If the neutrino is a Majorana fermion, neutrinoless double beta decay should occur but it was never observed. So, a neutrino can not be a

Majorana fermion. Several routes have been proposed to realize Majorana fermion. It has been predicted that Majorana fermion could emerge as a collective excitation of some elementary particles in certain condensed matter systems. These collective excitations have zero energy and therefor known as zero energy Majorana modes. Superconductors can host Majorana fermion because particle- hole symmetry is preserved in these materials. The Bogoliubov-de Gennes (BdG) quasiparticle excitations in the superconductors can be represented by the superposition of particles and holes. In condensed matter physics hole can be treated as an antiparticle. Let us consider a system where a single particle fermionic state is represented by λ, where λ can be spin, momentum, position etc. The creation operator $c_\lambda^\dagger$ create an electron in quantum state λ and the annihilation operator c_λ annihilate it from that state. In other words, c_λ can be defined as a creation operator for antifermion. Now in superconductors a new creation (annihilation) operator $\gamma_\lambda^\dagger$ (γ_λ) can be defined by equal superposition of a particle and a holes. The two such possible superpositions are $\gamma_\lambda \propto c_\lambda + c_\lambda^\dagger$ and $\gamma_\lambda \propto \imath(c_\lambda - c_\lambda^\dagger)$. For these superpositions $\gamma_\lambda = \gamma_\lambda^\dagger$, and hence these particles are their own antiparticle. This specific type of superposition is not observed in all superconductors. In a s-wave superconductor, the cooper pairs are made up of electrons of opposite spin. So the quasiparticle in conventionals s-wave superconductors are made up of equal superposition of electrons and holes having opposite spins. Due to this, $\gamma^\dagger \neq \gamma$, and therefore conventional superconductors will not satisfy a condition to observe Majorana fermions. This problem can be avoided in spin triplet $p_x + \imath\, p_y$ (p-wave) superconductors [69]. In a p-wave superconductor, it has been shown that the vortex of superconductor contains a quasiparticle with zero energy [70]. This quasiparticle is known as Majorana fermion. Some materials are proposed to host triplet p-wave pairing, and among them Sr_2RuO_4 is the most promising material [71]. However, the topological nature of this material is still unclear.

Fu and Kane proposed that effective p-wave superconductivity can be realized by combining surface states of 3D TIs with a conventional s-wave superconductor [72]. The newly engineered superconductor is called topological superconductor which can host Majorana fermion excitations. The non trivial topology of such proximity induced superconducting state is inherited from TIs. The proximity induced superconducting state has been confirmed in several reports [73, 74]. To achieve a TSC phase, various other attempts have been made, such as doping [75, 76, 77] or pressurizing [78] a parent topological material. Several routes have been proposed to detect Majorana fermions such as the 4π-Josephson effect [79], nonlocal tunneling [80], zero bias conductance peak [81], thermal metal-insulator transition [82] etc.

1.7 Structure of Thesis

Chapter 2 gives a brief description of sample synthesis and crystal growth techniques and their characterization by energy dispersive X-ray spectroscopy (EDX) and powder X-ray diffraction method. The experimental setups used to measure various physical properties (magnetotransport, heat capacity, dc magnetization) have been discussed.

In **Chapter 3** we present a detailed magnetotransport study on high quality single crystals of $Bi_{1-x}Sb_x$, ($0 \leq x \leq .16$). Bi is known to be a trivial semimetal. As Sb is introduced, a band inversion occurs at $x \approx 0.04$ signaling a topological phase transition into a TI state beyond x = 0.04. At the Topological transition point $x \approx 0.04$, the material is a DSM which changes to a WSM state on the application of a magnetic field. Very recently, the Sb rich side of $Bi_{1-x}Sb_x$ has been investigated theoretically and two new WSM phases have been predicted at large Sb doping of x = 0.5 and x = 0.83 . This suggests that new surprises are yet to be discovered even in this well studied system. We observe the chiral anomaly for our x = 0.03 crystals in agreement with previous report. Unexpectedly, we also find strong evidence of a WSM state for the x = 0.16 sample, which is close to the end of the TI state. The negative LMR is strongly suppressed with increasing angle between B and I. Additionally we observe a non-linear I-V for B $\parallel$ I but not for B $\perp$ I. A weaker but clearly observable negative LMR is also found for the x = 0.075 sample. These observations strongly indicate that in addition to x = 0.03, a WSM state exists for x = 0.075, 0.16 materials expected to be deep in the TI state.

In **Chapter 4** we present a detailed magnetotransport and dHvA quantum oscillations study on high quality single crystals of AT_2 (A = Pd, Pt) for both out-of-plane B $\parallel$ c and in plane B $\parallel$ ab. The number and positions of the frequencies observed in fast Fourier transform (FFT) spectra of quantum oscillations suggest different band structures for $PdTe_2$ and $PtTe_2$. Extracted transport parameters for $PtTe_2$ reveal a strong anisotropy which might be related to the tilted nature of the Dirac cone. Using a Landau level fan diagram analysis we find at least one Fermi surface orbit with a Berry phase of π consistent with Dirac electrons for both $PtTe_2$ and $PdTe_2$. The light effective mass and high mobility are also consistent with Dirac electrons in $PtTe_2$. Our results therefore suggest that similar to $PdTe_2$, $PtTe_2$ might also be a three-dimensional Dirac semimetal.
We also report experimental observation of the Planar Hall effect (PHE) in $PtTe_2$. Remarkably, the PHE in $PtTe_2$ can be observed up to temperatures near room temperature which indicates the robustness of the effect. The observation of this effect in nonmagnetic $PtTe_2$ suggests that PHE is a distinct and reliable signature of the chiral character in Dirac

and Weyl semimetals.

Chapter 5 contains a detailed magnetotransport study on single crystals of XBi (X = La, Pr). Last member of Lanthanum monopnictides series LaBi has the largest spin-orbit coupling, which reverts the bulk band order to form multiple Dirac cones in the bulk band structure. ARPES measurements on LaBi have shown the presence of multiple odd number of Dirac cone making this system more interesting for further study. The Fermi surface properties of LaBi have been analyzed by pronounced dHvA oscillations. We confirm the Dirac nature of the charge carriers in LaBi by extracting a Berry phase of π by fitting the quantum oscillations by full Lifshitz-Kosevich formula.
PrBi is a novel material in which the presence of f electrons, in addition to the possible topological band structure found in ARPES, raises the prospect of realizing a strongly correlated version of topological semimetals. We observe a magnetic-field-induced metal-insulator-like transition below T $\sim$ 20 K and a very large magnetoresistance ($\approx 4.4 \times 10^4\%$) at low temperatures (T = 2 K) . We have also probed the Fermi surface topology by de Haas–van Alphen and Shubnikov–de Haas quantum oscillation measurements complimented with density functional theory (DFT) calculations of the band structure and the Fermi surface. Angle dependent measurements of the Shubnikov–de Haas oscillations suggest that the transport is dominated by bulk bands. A Lifshitz-Kosevich fitting of the quantum oscillation data as well as a Landau fan diagram analysis gave a Berry phase close to π, suggesting the presence of Dirac fermions in PrBi.

In **Chapter 6** we examined the nature of superconductivity in $PdTe_2$ and Pd:Bi_2Te_3. $PdTe_2$ is an exciting material where a superconducting and topological state coexist. Our heat capacity measurements confirm bulk superconductivity at T_c = 1.7 K and show that the anomaly at T_c is characterized by the ratio $\Delta C / \gamma T_c \approx 1.5$. This value is close to 1.43 which is expected for a weak-coupling, single-band BCS superconductor. The electronic contribution to the heat capacity C_{el} at the lowest temperatures shows an exponential T dependence, which points to a gapped s-wave superconductivity. From H dependent C(T) measurements, we find C_{el}/ T $\sim$ H, in contrast with behavior expected for nodal superconductivity. Additionally, the critical field versus temperature phase diagram shows a behavior expected for a conventional superconductor. Thus, our measurements strongly indicate that the superconductivity in $PdTe_2$ is conventional in nature despite the presence of topologically nontrivial electrons contributing to the transport.
This chapter also includes the study of magnetic field vs. temperature (H–T) and pressure vs. temperature (P–T) phase diagrams of the $T_c \approx 5.5$ K superconducting phase in $PdBi_2Te_3$ (x $\approx$ 1). From high pressure magnetic measurements, we found that T_c is suppressed to lower temperatures approximately linearly with pressure P at a rate dT_c/dP $\approx$

-0.28 K/GPa. The H-T and P-T phase diagrams give seemingly conflicting results about the nature (conventional or unconventional) of superconductivity in $PdBi_2Te_3$.

In **Chapter 7**, I will summarize the main results carried out in this thesis work.

CHAPTER 2

Experimental Details

In this chapter we gives a brief description of sample synthesis and crystal growth techniques and their characterization by energy-dispersive X-ray spectroscopy (EDX) and powder X-ray diffraction method. The experimental setups used to measure various physical properties (magnetotransport, heat capacity, dc magnetization) have been discussed.

2.1 Sample Preparation

We have grown single crystals of the $Bi_{1-x}Sb_x$ ($0 \leq x \leq .16$), XBi (X = La, Pr), ATe_2 (A = Pd, Pt) and $Pd_xBi_2Te_3$ ($x \approx 1$). The techniques used to grow these crystals are described below. The techniques used to grow these crystals are described below and schematic details of the heat treatment are given in Fig. **??**.

2.1.1 Modified Bridgman technique

The single crystals of $Bi_{1-x}Sb_x$ ($0 \leq x \leq .16$), $PdTe_2$ and $Pd_xBi_2Te_3$ were grown by this technique. In this technique the material to be grown is taken into a vertical cylinder (quartz tube) and placed into a suitable furnace for complete melting. For crystal growth, the material is slowly cooled which leads into the single crystals, oriented along some preferred direction. Muffle furnaces have been used for the heat treatment of samples (shown in Fig. 2.1).

Figure 2.1: Tabletop muffle furnaces used for heat treatments of the samples.

$Bi_{1-x}Sb_x$

For single crystals of $Bi_{1-x}Sb_x$ ($0 \leq x \leq .16$), stoichiometric amounts of Bi (5N) and Sb (5N) were ground, palletized and thereafter sealed in a quartz tube under vacuum. The quartz tube was placed vertically in a box furnace and heated to 650 ^{o}C in 15 hrs, kept there for 8 hrs, and then slowly cooled to 270 ^{o}C over a period of five days for crystal growth. The crystals are kept at 270 ^{o}C for seven days for annealing and homogenization. Large shiny crystals could be cleaved from the resulting boul. It was found that there was a concentration gradient from top to bottom in the quartz tube and crystals of different concentration could be cleaved from same boule.

$PdTe_2$

For single crystals of $PdTe_2$, the starting elements, Pd powder (99.99% purity) and Te shots (99.9999%), were weighed in the atomic ratio 1 : 2.2 and sealed in an evacuated quartz tube. The 10% extra Te was taken to compensate for Te loss due to its high vapor pressure. For crystal growth, the tube with the starting materials was heated to 790 °C, kept there for 48 h, and then slowly cooled to 500 °C over seven days. The tube was then annealed at 500 °C for five days before cooling naturally to room temperature. The shiny crystals of millimeter size thus obtained could be cleaved easily from the as-grown boule.

$Pd_xBi_2Te_3$

For single crystals of $Pd_xBi_2Te_3$ ($x \approx 1$), Stoichiometric amounts of Pd (4N), Bi (5N), and Te (5N) were ground together, pelletized and sealed in a quartz tube under partial Ar pressure. For crystal growth the tube was placed vertically in a box furnace and heated to 900^o C in 8 hrs, kept there for 10 hrs, then slowly cooled at a rate of 2^o C/hr to 650^o C after which the furnace was switched off and allowed to cool to ambient temperature. For polycrystalline samples, two heat treatments at 900^o C for 24 hrs each with a regrind and

pelletizing step in between, were used.

2.1.2 Flux growth technique

The flux growth technique is widely used to synthesizes the single crystals of material which melts incongruently. In this method the matrials to be crystallized are dissolved into a suitable solvent. The crystallization process starts when solution becomes supersaturated. The supersaturation can be attained by lowering the temperature of solution or by evaporation of solvent. This technique is particular useful for crystals growth of oxides material having high melting point and the material whose phase transition temperature lies below the melting point. The key points which should be satisfied for crystal growth using flux growth method are [83]:
(i) The solute must be the only stable solid phase at growth conditions.
(ii) The melting point of flux should be low and its solubility should decrease with temperature.
(iii) The flux should have low viscosity and vapor pressure.
(iv) The flux should not react with the crucible.
(v) The flux should easily seprated from crystals

Following are the single crystals grown by this technique.

$PtTe_2$

The single crystals of $PtTe_2$ were grown by self-flux method, where Te act as a flux. For $PtTe_2$ crystals, the starting elements Pt powder (99.9 %, Alfa Aesar) and Te lump (99.9999%, Alfa Aesar) were taken in the molar ratio 2 : 98 and sealed in an evacuated quartz tube. The tube was heated to 790 °C in 15 h, kept at this temperature for 48 h in order to homogenize the solution and then slowly cooled to 500 °C at a rate of 2.5 °C/hr. The excess Te liquid was decanted isothermally for 2 days. Finally, the tube was allowed to cool down to room temperature by shutting off the furnace. Plate-like hexagonal shaped crystals were obtained after breaking open the tube at room temperature.

XBi (X = La, Pr)

High quality single crystals of XBi (X = La, Pr) were grown by using Indium flux. The purity of rare earth metals La and Pr was 99.9 % whereas the purity of Bi and In was 99.999 %. The starting elements La, Bi and In (for LaBi) and Pr, Bi and In (for PrBi) were taken in molar ratio of 1 : 1 : 20. The elements were put into an alumina crucible and sealed into a evacuated quartz tube. The sealed quartz tube was heated to a temperature of 1050 °C in 10 h, kept at this temperature for 5 h and then slowly cooled to 700 °C at a rate of 2.1 °C/hr. At this temperature excess In was removed by a centrifuge. The typical

size for LaBi crystal was 2 × 1 × 1 mm and for PrBi crystal it was 3.5 × 2 × 1 mm. The pictograms of heat treatment are shown in Fig. 2.2.

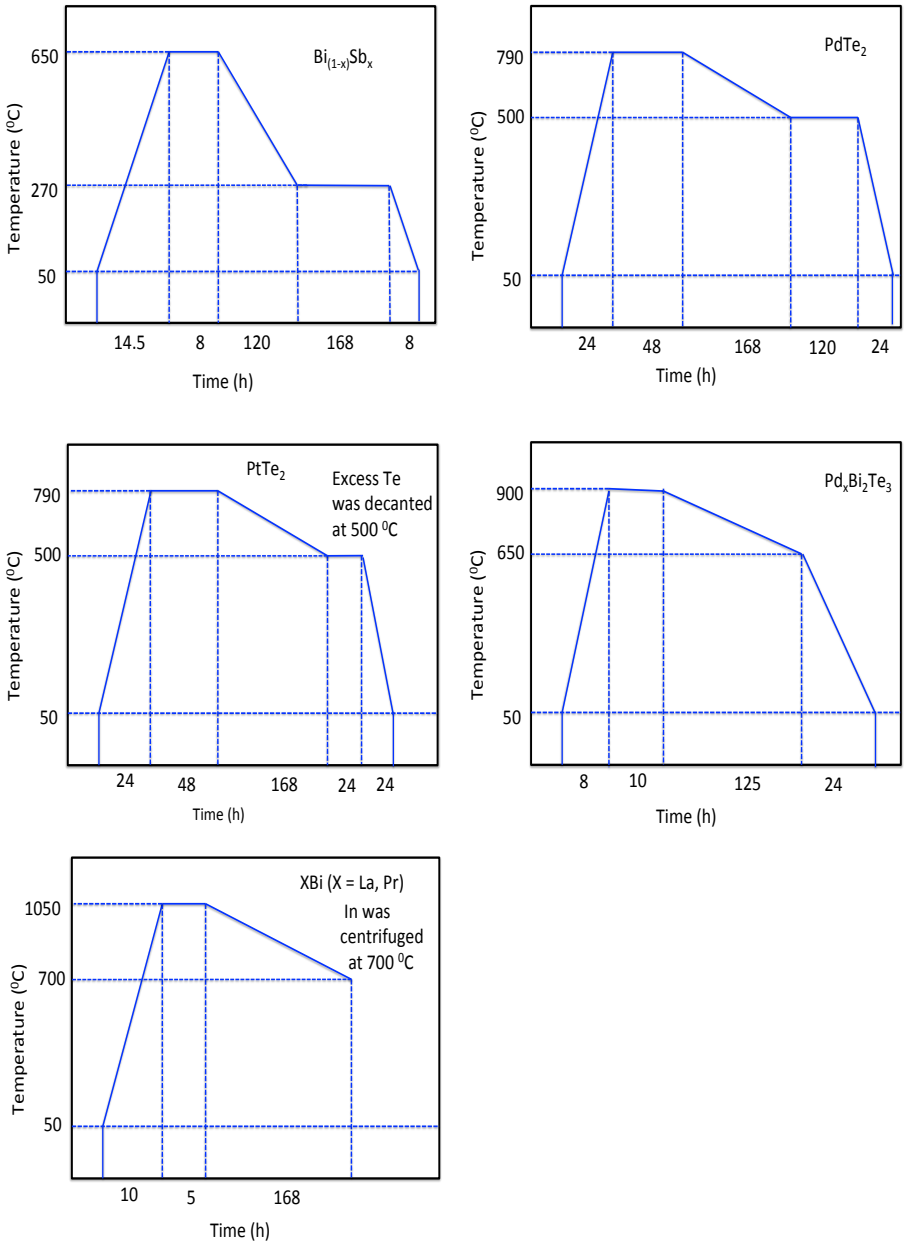

Figure 2.2: Schematic details of the heat treatment of different materials.

2.2 Sample Characterization

2.2.1 Energy dispersive spectroscopy

Energy-dispersive X-ray spectroscopy (EDS) is a standard technique, used to determine the chemical composition of a sample. This technique relies on the fact that each element has unique atomic structure which emits unique energy characteristic X-ray, stimulated by high energy electron beam. The generation of characteristic X-ray in EDS can be explained in two steps. In first step, high energy electron beam is bombarded on the sample. This energy beam transfer part of its energy to the atom of specimen and, electron inside the atom can use this energy to jump to high energy level or can be kicked-out from the atom. In such a scenario, a vacancy is created in place of electron. In second step, electron from higher energy level fills this vacancy and energy difference between two levels can emitted in the form an X-ray. Each element has unique characteristic X-ray spectrum and can be used to determine elemental composition of the sample. This two step process is shown in Fig. 2.3, where a primary electron beam hit the electron and create a vacancy at position 1 and this vacancy is filled by transition of electron from position 2 to 1 by emitting characteristic X-ray.

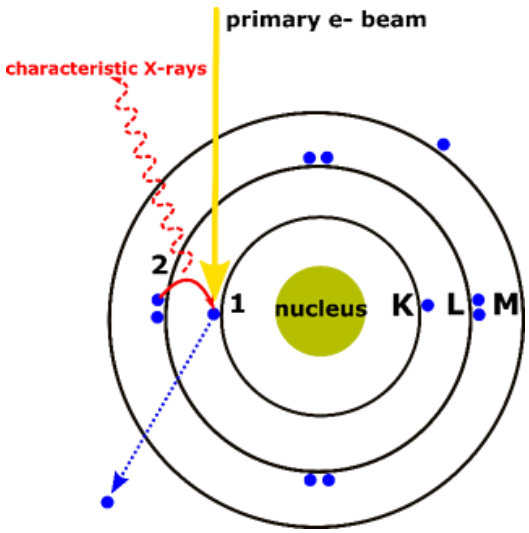

Figure 2.3: Schematic diagram showing the emission of characteristic X-ray by the interaction of elecrton beam to the sample.

2.2.2 Powder X-ray

Powder X-ray diffraction (PXRD) technique is widely used to characterize the crystal structure the materials. After synthesizing desired single crystals, we have first confirmed

their crystal structure and phase purity. The wavelength of X-ray is of the order of 1 Å, which is comparable to interatomic spacing in crystalline materials. Laue, suggest that a crystal could serve as a natural grating and therefore should exhibit diffraction pattern [84].

W.L Bragg gave simple interpretion of diffraction pattern. According to his theory a crystal consists of various sets of equally spaced parallel planes. When atoms are exposed to X-rays, the incident light get reflected and results in constructive interference. The condition for observing Bragg's reflection is given by a metamathematical relation,

$$2dsin\theta = n\lambda. \tag{2.1}$$

This is called Bragg's law. Here d is the interplanar spacing of planes, θ is the angle between incident ray and plane of reflection, n stands for order of reflection, λ is the wavelength of incident X-ray. In a PXRD experiment one could observe Bragg's reflection at all angles, where Bragg's condition (Equ. 2.1) is satisfied. Hence for fixed λ, by measuring 2θ at which reflection occur, one can determine interplanar spacing. The position and intensity of Bragg's peaks are directly related with unit cell parameters and arrangement of atoms inside a unit cell.

A few crystals of synthesized materials, were crushed into powder for PXRD measurements done using Rigaku high-resolution X-ray diffractometer. The powder diffraction pattern were recored in 2θ range from 10^o to 90^o at a step of 0.02^o. After obtaining experimental data the crystal structure were analyzed by Rietveld method using General structure analysis software [85]. The phase purity and lattice parameter were determined.

2.3 Physical Properties Measurements

After confirming chemical composition and phase purity of the samples, various physical properties were measured by quantum-design physical property measurement system (QD-PPMS) shown in Fig. 2.4.

2.3.1 Electrical resistivity

The temperature dependence of AC and DC resistivity of the samples were measured by standard four probe technique. In this technique four ohmic contacts were made on bar shaped sample, using very small diameter gold wires and highly conducting silver paint or epoxy. Out of these four wires, the two outer wires were used to supply current (1 to 5 mA) and two inner wire were used to measure voltage. The accuracy of four wire measurement technique is higher than two wire because it reduces the contribution of

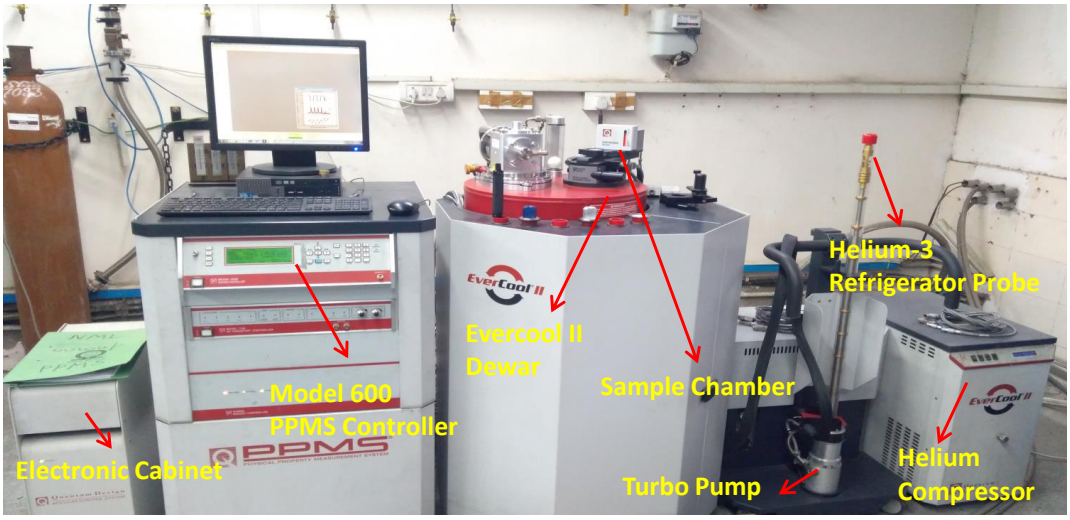

Figure 2.4: Quantum Design Physical Property Measurement System(PPMS).

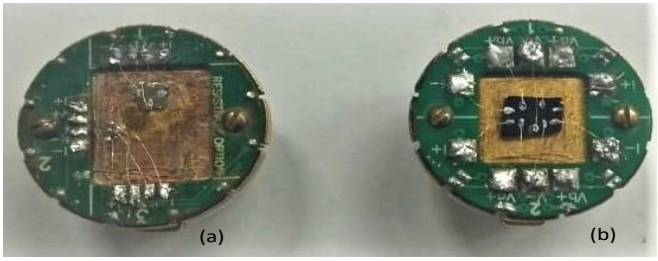

Figure 2.5: Sample mounted on a (a) DC resistivity and (b) AC resistivity puck.

lead resistance. For a sample of cross section area A, the resistivity ρ can be calculated by measuring voltage (v) using Ohm's law:

$$\rho = \frac{VA}{Il}, \tag{2.2}$$

where l is the distance between two voltage leads and I is the constant current supplied to the system. The DC and AC resistivity were measured in the temperature from 300 K to 2 K and in a magnetic field upto 9 T. On DC resistivity puck (shown in Fig. 2.5 (a)), one can mount three sample at a time and can adjust current excitation upto $\pm$ 5 mA.

The AC measurement has greater sensitivity than DC measurement and mainly used for highly conducting samples. The ACT option supports various transport measurements such resistivity, Hall coefficient, I-V curve and critical current. The typical picture of DC and AC resistivity puck with samples are shown in Fig. 2.5.

The electrical resistivity down to 0.4 K were measured using the He3 option of QD-PPMS. The angle dependent magnetoresistance measurements were carried out on some of the single crystals. For this purpose Horizontal Rotator option of QD-PPMS was used

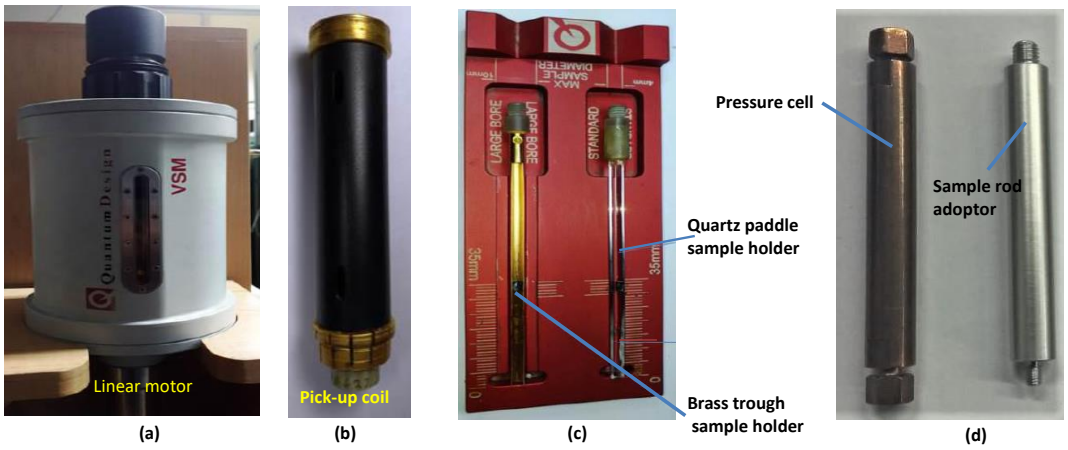

Figure 2.6: VSM linear motor used for vibrating the sample (b) pickup coil for magnetic flux detection (c) the quartz tube and brass tube sample holders (d) Cu-Be pressure cell and Al sample rod adoptar.

which allow to rotate the sample around a perpendicular axis to the magnetic field. The range of sample rotation is -10^o to 370^o.

2.3.2 DC magnetization

The DC magnetization measurements between 2 K and 300 K and isothermal magnetization measurements in field upto 9 T were performed using Quantum Design Vibrating Sample Magnetometer (VSM). The VSM option consist of linear motor used to vibrate the sample, pick-up coils for signal detection and electronics to derive the linear motor (shown in Fig. 2.6 (a) and (b)). The sample was stuck to the brass and glass sample holder tube with the help of GE varnish (shown in Fig. 2.6 (c)). The VSM works on the basic principal that a vibrating sample will induce a voltage in the pick-up coil. The time dependent voltage (V) induced in the pick-up coil is given by the following equation:

$$V_{coil} = \frac{d\phi}{dt} = \frac{d\phi}{dz}\frac{dz}{dt}, \tag{2.3}$$

where ϕ is the magnetic flux enclosed by the pickup coil, z is the vertical position of the sample with respect to the coil, and t is time. The VSM linear motor is designed to operate upto 40 Hz frequency and can resolve magnetization changes of less than 10^{-6} emu at a data rate of 1 Hz.

Magnetic susceptibility $\chi(T)$ at various pressures P $\leq$ 1.3 GPa were measured using a Cu-Be pressure (shown in Fig. 2.6 (d)) cell with the VSM option of a Quantum Design PPMS. Sn was used to get a proper estimate of pressure on the sample at low temperature.

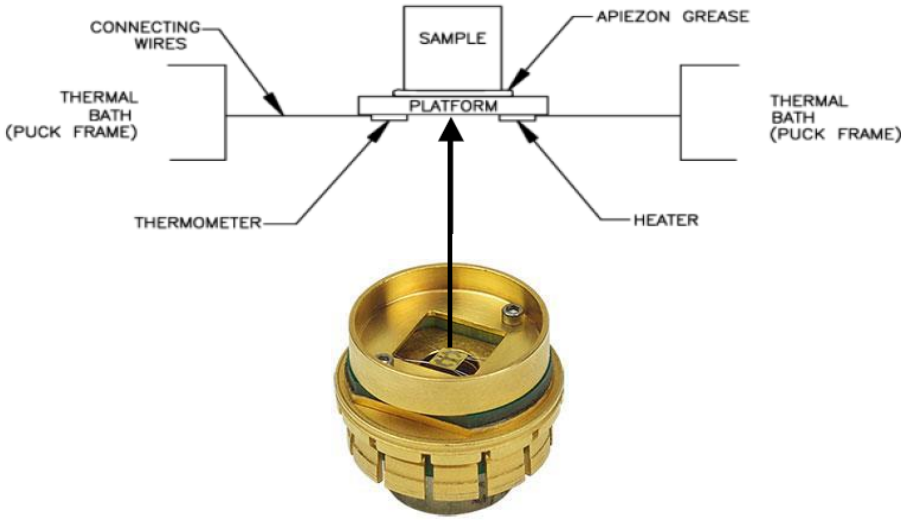

Figure 2.7: Heat capacity sample puck and schematic of thermal connections to Sample and Sample Platform.

2.3.3 Heat capacity

Heat capacity is the heat required to raise the temperature of material by one unit. Heat capacity measurement provide important information about magnetic and structural phase transitions in materials. Zero field and field dependent heat capacity down to 0.4 K were measured using the He3 option of a QD-PPMS. QD-PPMS measure heat capacity at constant pressure and uses relaxation technique of measurement.

In this technique, sample is placed on the on a platform which is connected with a weak thermal link to a constant temperature bath (puck), at a temperature T_0. A small amount of heat is supplied which raises the sample temperature by ΔT (typically $\Delta T/T$ = 1%). After switching off the heater the temperature of sample starts decaying exponentially. The exponentially decaying temperature T_s is given by:

$$T_s = T_0 + \Delta T exp(-t/\tau) \tag{2.4}$$

where t is the time and τ is the sample to bath relaxation time constant. The heat capacity C is calculated by measurement of τ and the known thermal conductivity κ of the weak thermal link as:

$$C = \tau\kappa. \tag{2.5}$$

The heat capacity sample puck and schematic of thermal connections to sample and sample platform are shown in Fig. 2.7. A heater and a thermometer are attached to the

bottom of the sample platform. Apiezon-N grease was used to stick the sample to the platform, which also provide thermal contacts between platform and sample. The adiabatic condition required for heat capacity measurement is obtained by creating high vacuum (10^{-6}) inside the sample chamber using PPMS cryopump high-vacuum option.

CHAPTER 3

Evolution of Berry phase and observation of chiral character in $Bi_{1-x}Sb_x$

3.1 Introduction

The Bismuth-Antimony (Bi-Sb) alloy system $Bi_{1-x}Sb_x$ is an ideal system to study the transition from a topologically trivial to a non-trivial phase as a function of x. Pure Bi is a topologically trivial semimetal with A7 type rhombohedral structure [86]. The substitution of Bismuth with antimony changes the band structure of Bismuth as summarized in Figure 3.1 [17, 87]. As the Antimony substitution in Bismuth increases the band gap between L_a and L_s bands decreases. At $x \approx 0.04$ the gap between these two bands closes and a Dirac point is observed. As the x is further increased, the band gap reopens with an inverted ordering. "Also the the top of the valence band at T comes down in energy and crosses the bottom of the conduction band at $x = 0.07$. At $x = 0.09$ the T valence band clears the L_s valence band, and the alloy is a direct gap semiconductor at the L points. As x is increased further, the gap increases until its maximum value of order 30 meV at $x = 0.18$. At that point, the valence band at H crosses the L_s valence band. For $x = 0.22$ the H band crosses the L_a conduction band, and the alloy is again a semimetal" [17].

At the topological transition point $x \approx 0.04$, the material is a Dirac Semimetal (DSM) which changes to a Weyl semimetal (WSM) on the application of a magnetic field. Indeed the chiral anomaly in the B $\parallel$ E configuration with a strongly angle dependent negative longitudinal magnetoresistance (LMR) has been observed for x = 0.03 material [61]. Additionally, a violation of the Ohm's law has been observed for x = 0.05 material which

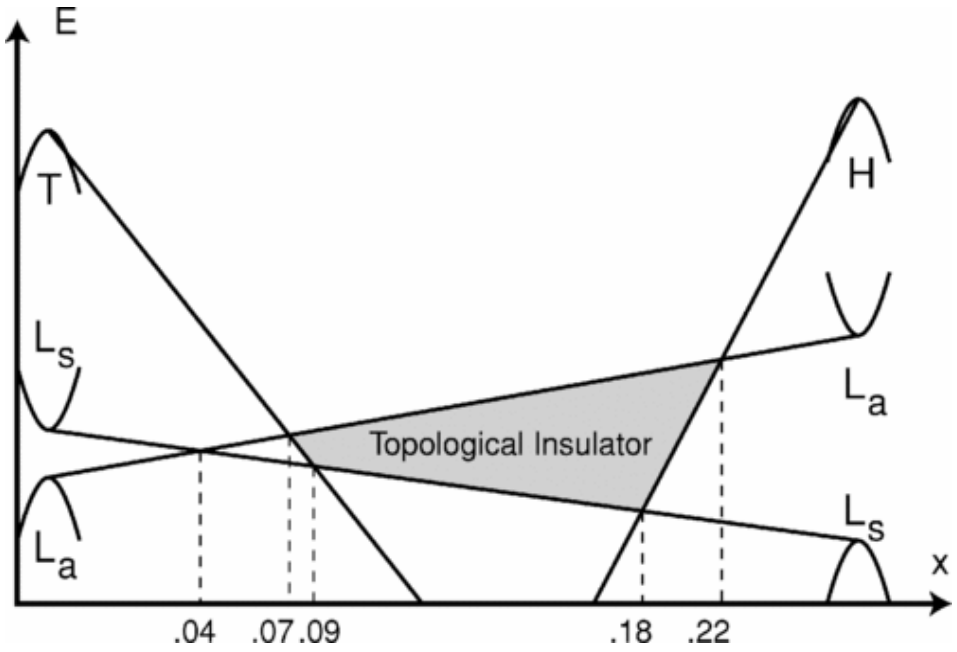

Figure 3.1: Schematic representation of band structure evolution of $Bi_{1-x}Sb_x$ as a function of x at T = 0 K. Reproduced from **Journal of Physics and Chemistry of Solids 57, 89 (1996)**.

also lie close to the topological phase transition into a TI state, and has been argued to be a consequence of the chiral anomaly. This study also concluded that no negative LMR was observed for samples far away $x > 0.05$ from the topological transition [88]. Thus, $Bi_{1-x}Sb_x$ alloys host a TI state in an extended range x = 0.03 – 0.22, a DSM state at $x \approx 0.04$, and a WSM state for $x \approx 0.04$ when TRS is broken by the application of a magnetic field. Very recently, the Sb rich side of $Bi_{1-x}Sb_x$ has been investigated theoretically and two new WSM phases have been predicted at large Sb doping of x = 0.5 and x = 0.83 [89]. This suggests that new surprises are yet to be discovered in this well studied system.

In this chapter, we report a detailed magnetotransport study on some high quality single crystals of $Bi_{1-x}Sb_x$, covering the large TI range x = 0 – 0.16.

3.2 Experimental Details

Single crystals of $Bi_{1-x}Sb_x$ ($0 \leq x \leq .16$) were grown using a modified Bridgman technique as described in detail in chapter 2. The actual composition of the grown crystals

were checked by chemical analysis using energy dispersive X-ray spectroscopy (EDX). Some crystals of each composition were ground into powder for X-ray diffraction (PXRD) measurements. The PXRD patterns for all crystals were found to be single phase and crystallizing in the expected structure. Rietveld refinement technique was used to refine the structural parameters from the PXRD patterns. A typical PXRD pattern and the results of a refinement of the data for $Bi_{1-x}Sb_x$ with x = 0.04 are shown in Figure 3.2 and confirmed the formation of crystals with the Bi structure with lattice parameters a = 4.528 Å, c = 11.818 Å which as expected, are smaller than those of pure Bi (a = 4.546 Å, c = 11.862 Å). Lattice parameter and unit cell volume was found to monotonically decreases with antimony doping, consistent with previous reports [1]. The goodness of fit (χ^2) value obtained after Rietveld refinement for $Bi_{1-x}Sb_x$ was 5. Electrical and magnetic transport was measured using a Quantum Design Physical Property Measurement System (PPMS).

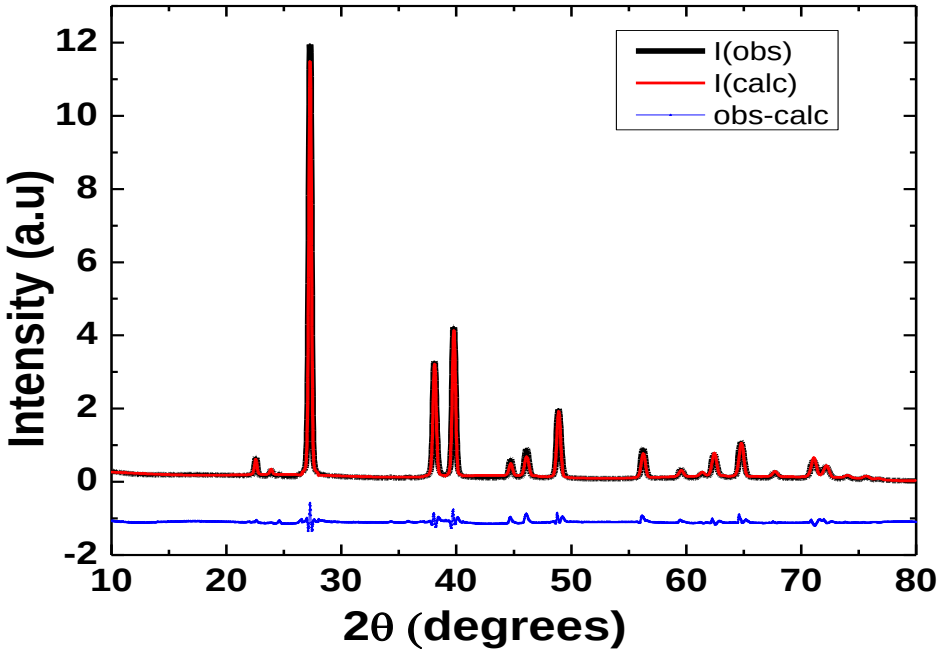

Figure 3.2: Powder X-ray diffraction pattern of $Bi_{1-x}Sb_x$ (x = 0.04) sample and its rietveld refined data are shown.

3.3 Results

Figure 3.3 (a) and (b) show the electrical resistivity ρ versus temperature T for crystals of $Bi_{1-x}Sb_x$ ($0 \leq x \leq .16$) from 2 to 305 K measured in zero applied magnetic field B and a current I = 2 mA. Figure 3.3 (a) shows the ρ(T) for $Bi_{1-x}Sb_x$ crystals for x smaller than the critical concentration for transition to a topological insulator phase. These data

are typical of (semi-)metals where the electrical resistivity decreases with decrease in temperature.

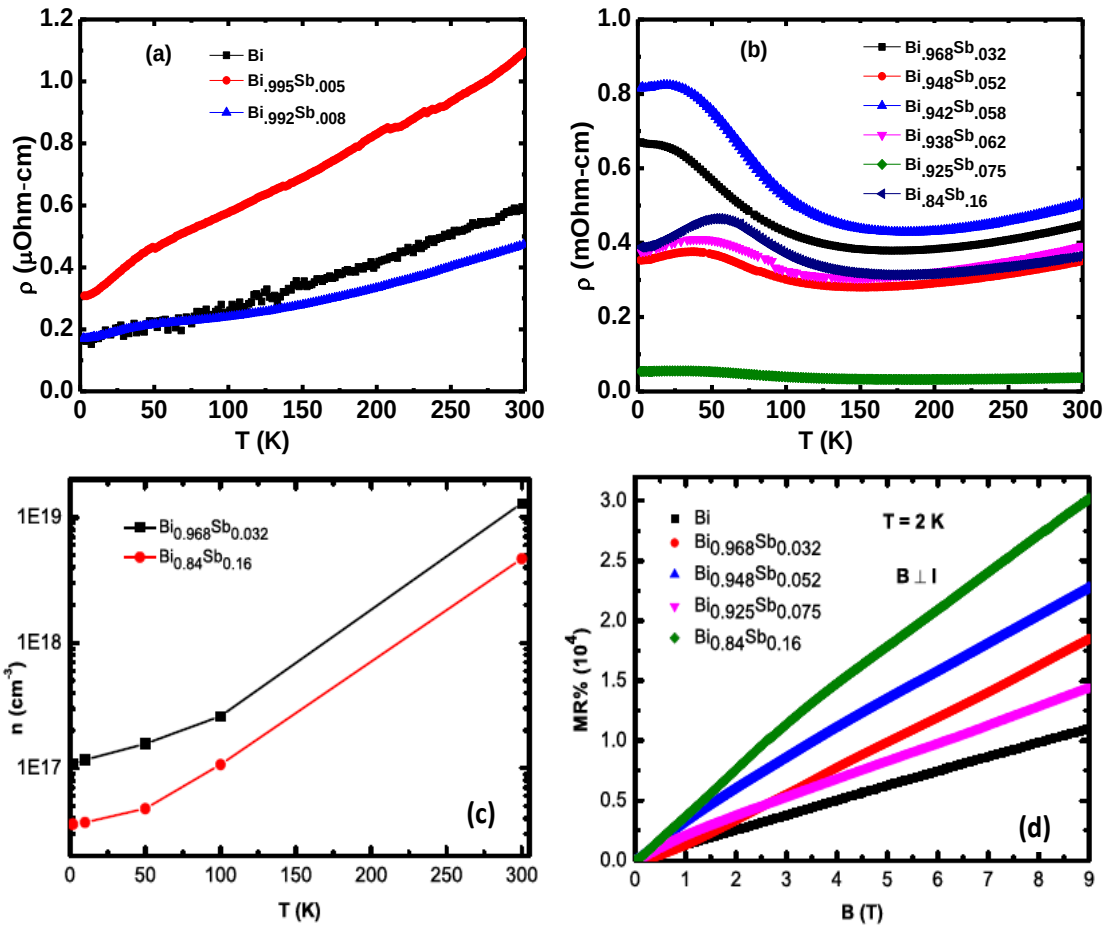

Figure 3.3: (a) and (b) Resistivity ρ vs temperature T for $Bi_{1-x}Sb_x$. (c) The carrier density n versus T for x = 0.032, 0.16 samples. (d) Transverse magneto resistance MR vs B at T = 2 K for $Bi_{1-x}Sb_x$. The MR for all x is positive and linear at high B.

Figure 3.3 (b) shows the ρ(T) data for $Bi_{1-x}Sb_x$ with x $\geq$ = 0.032. For all these materials the qualitative T dependence is similar. There is a weak metallic behaviour at high temperatures before a minimum in ρ(T) is observed around T = 100 – 150 K . For lower T the ρ(T) increases as T decreases. Finally the ρ(T) passes over a maximum and shows metallic behaviour for lower temperatures. Such a ρ(T) is expected for a topological insulator where the charge gap in the bulk band structure suppresses bulk conduction below some T and ρ increases below this T. For sufficiently low T where the bulk conductivity becomes too small,conduction through surface states takes over and ρ(T) stops increasing. The competition between surface and bulk conductivity influences the position of maxima and minima in ρ(T).

Figure 3.3 (c) shows the carrier density n estimated from Hall measurements, as a function of T for the x = 0.032, 0.16 samples. The n drops by about two orders of mag-

nitude on cooling from 300 K to 2 K indicating the gapped nature of the crystals. Large conventional transverse magnetoresistance with magnetic field perpendicular to the current direction has been reported in the TI state. Transverse magnetoresistance (MR) for $B \perp I$ is shown in Figure 3.3 (d). We observe large non-saturating positive MR for all samples which is linear up to the largest B, consistent with previous observations on samples close to x = 0.04 [90]. Thus our samples show behaviour consistent with them being in the TI state. We note that the MR is largest for the x = 0.16 sample and is much larger than reported previously for the x = 0.04 samples close to the trivial to topological insulator transition.

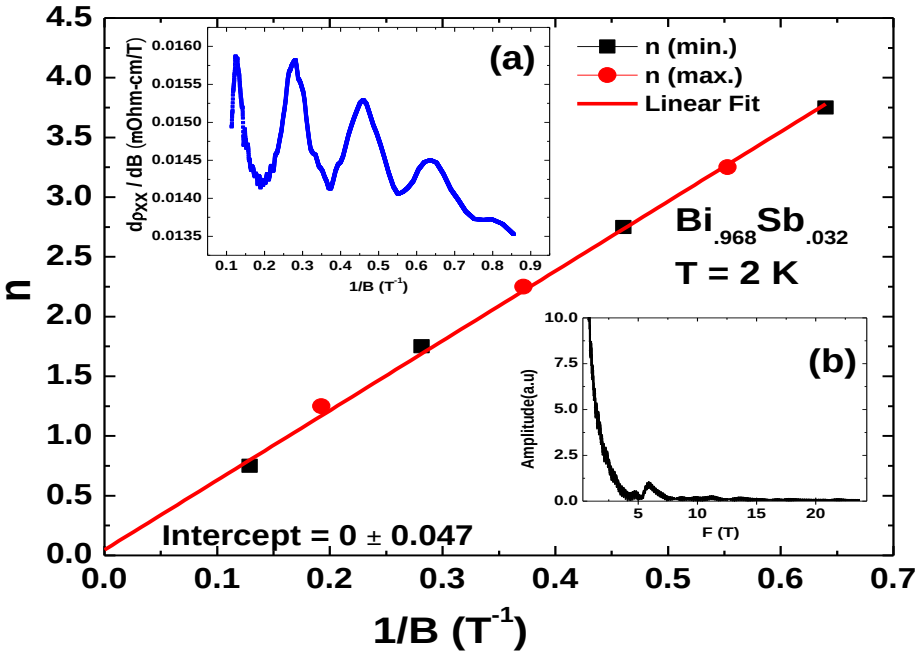

Figure 3.4: Inset (a) shows the SdH oscillations at T = 2 K for $Bi_{.968}Sb_{.032}$. Inset (b) shows the Fast Fourier transform (FFT) of SdH oscillation measured at 2 K. Main plot show Landau fan diagram, extracted from quantum oscillation. The extrapolated intercept is close to what is expected (0) for a topologically trivial system.

To explore the low temperature metallic behaviour and Fermi surface properties of $Bi_{1-x}Sb_x$, we measure the SdH oscillations in $Bi_{.968}Sb_{.032}$ and $Bi_{.925}Sb_{.075}$. In real samples of topological insulators, it is challenging to separate bulk and surface conductivity due to residual carriers in the bulk [91, 92]. At low temperature both ρ_{xx} and ρ_{xy} shows oscillations with magnetic field. Derivative of ρ_{xx} with magnetic field vs. 1/B shown in inset of figure 3.4 (a) and figure 3.5 (a), clearly shows the SdH oscillations at 2 K. The Fast Fourier transform (FFT) of these oscillations gives a single oscillations frequency at F =

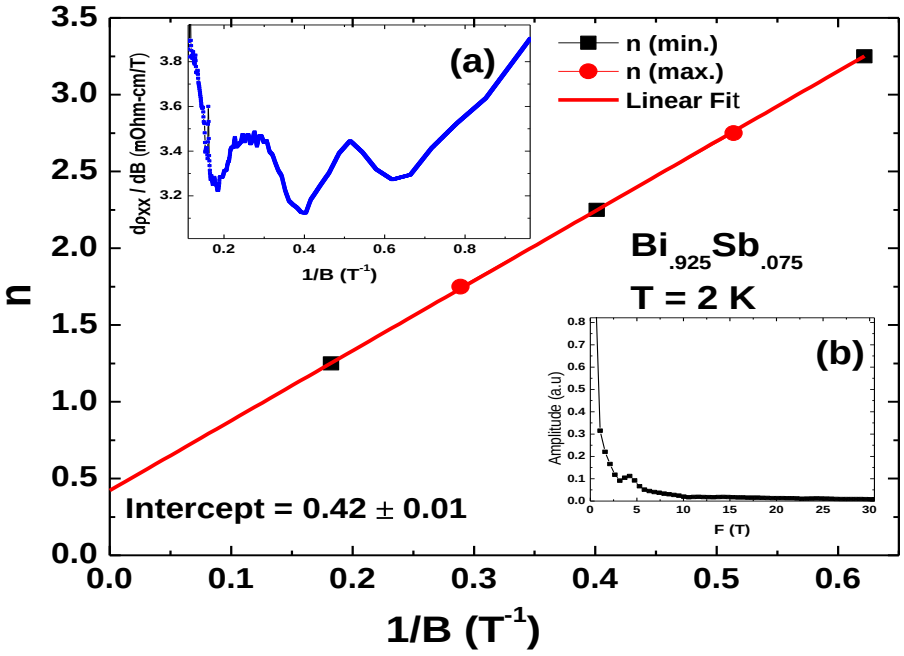

Figure 3.5: Inset (a) shows the SdH oscillations at T = 2 K for $Bi_{.925}Sb_{.075}$. Inset (b) shows the Fast Fourier transform (FFT) of SdH oscillation measured at 2 K. Main plot show Landau fan diagram, extracted from quantum oscillation. The extrapolated intercept is close to what is expected (0.5) for a topologically nontrivial system.

4.24 T and F = 5.83 T for $Bi_{.925}Sb_{.075}$ and $Bi_{.968}Sb_{.032}$ respectively. The oscillation frequency (F) is related to the Fermi surface area (A_F) in momentum space via the Onsager relation $F = (\hbar/2\pi e)A_F$ [93]. The calculated Fermi surface area for these frequencies are $40.45 \times 10^{15}\ m^{-2}$ and $56 \times 10^{15}\ m^{-2}$. The Fermi wave vector can be calculated by relation $k_F = (A_F/\pi)^{1/2}$ and 2D charge carrier density n_{2D} by $k_F^2/4\pi$. We find k_F as 0.0113 $Å^{-1}$, 0.013 $Å^{-1}$ which corresponds to n_{2D} of $1.02 \times 10^{11} cm^{-2}$ and $1.34 \times 10^{11} cm^{-2}$ for $Bi_{.925}Sb_{.075}$ and $Bi_{.968}Sb_{.032}$ respectively.

In a topological insulator the surface electron modes are arranged in a single Dirac cone with vortex like spin arrangement. The spin direction rotates as one goes around the Dirac cone causing the electronic wave function to acquire a Berry's phase (Φ_B) of π [94]. In order to calculate Berry phase we plot the Landau Fan diagram which is plot of n (Lamdau level index) vs 1/B where integer n + 1/4 corresponds to minima and n + 3/4 corresponds to maxima of SdH oscillations. The landau level index is related with the Fermi surface area via Lifshitz-Onsager quantization rule $A_F\hbar/eB = 2\pi(n + 1/2 + \beta + \delta)$ [95]. Here, $2\pi\beta$ is the Berry's phase and $2\pi\delta$ is phase shift $(\delta = \pm 1/8)$ for a three dimensionality of Fermi surface [96]. The Fermi wave vector and 2D carrier density of $Bi_{.925}Sb_{.075}$

calculated by Landau Fan diagram is 0.0118 $Å^{-1}$ and $1.1 \times 10^{11} cm^{-2}$ respectively. We got similar value for the Fermi wave vector and 2D carrier density from frequency of oscillations and Landau Fan diagram. Linear fitting of index gives finite intercept of 0.42 ± 0.01 (corroseponding to $\Phi_B = .84 \pm 0.02\ \pi$) and 0 ± 0.047 (corroseponding to $\Phi_B = 0\ \pi$) for $Bi_{.925}Sb_{.075}$ and $Bi_{.968}Sb_{.032}$ respectively. The calculated value of (Φ_B) for $Bi_{.925}Sb_{.075}$ is close to expected value of π for non trivial topology. Departure of extracted Φ_B from π for Dirac fermion has been highlighted by many groups [97, 98, 99]. One possible explanation is that topological trivial bands contribute towards SdH oscillations i.e deviation from ideal linear dispersion relation for Dirac fermions [100].

We now show evidence for the chiral anomaly in the whole TI region. Figure 3.6 (a) shows the resistivity ρ vs magnetic field B measured at temperature $T = 2$ K with the magnetic field B applied parallel to the electrical current I for $Bi_{1-x}Sb_x$ ($x = 3.2, 7.5, 16\%$). These three samples are located at (i) the transition from the normal insulator to a TI ($x = 0.032$), (ii) in the middle of the x range in which a TI has been shown to exist ($x = 0.075$), and (iii) near the end of the range of the TI state ($x = 0.16$). For the $x = 0.032$ sample, we observe that after the initial increase in ρ at small B most likely arising from 3D weak anti-localization (WAL), the ρ turns down and starts decreasing upto the highest B measured. This is the negative longitudinal ($B \parallel I$) magnetoresistance (NLMR) or the chiral anomaly. For $x = 0.032$ the $Bi_{1-x}Sb_x$ is situated close to the Dirac semi-metal state and the application of a magnetic field leads to time-reversal symmetry breaking and hence the Dirac cone is expected to split into a pair of Weyl nodes and so the chiral anomaly (NLMR) for this composition is expected and has been observed previously as well for $Bi_{0.096}Sb_{0.04}$ [61] and $Bi_{0.095}Sb_{0.05}$ [88] samples.

What is surprising is that we observe a chiral anomaly even for samples far away from $x = 0.032$. Figure 3.6 (a) also shows the ρ vs B data for $x = 0.075$ and $x = 0.16$. The $x = 0.075$ sample shows a weak negative LMR above $B \sim 4$ T, suggesting a Weyl state for this x too. However, the ρ data for $x = 0.16$ shows the strongest negative LMR compared to even the $x = 0.032$ sample, which is our main focus in this study. The NLMR keeps increasing and remains unsaturated up to the highest magnetic fields measured $B = 9$ T. This strongly suggests that a WSM state exists for $x = 0.16$ as well. A crucial signature of the chiral anomaly is the strong dependence of the NLMR on the angle between B and I. Figure 3.6 (b) shows the angle dependence of the NLMR for the $x = 0.16$ sample. We observe that for angle $= 0$ ($B \parallel I$), the NLMR is the largest and as the angle between B and I is increased, the magnetoresistance quickly increases and changes to completely positive MR for angle $\geq 8\ ^o$. This strong sensitivity of the NLMR to the angle between B and I is strong evidence of the chiral anomaly for the $x = 0.16$ sample and points to it being in the WSM state.

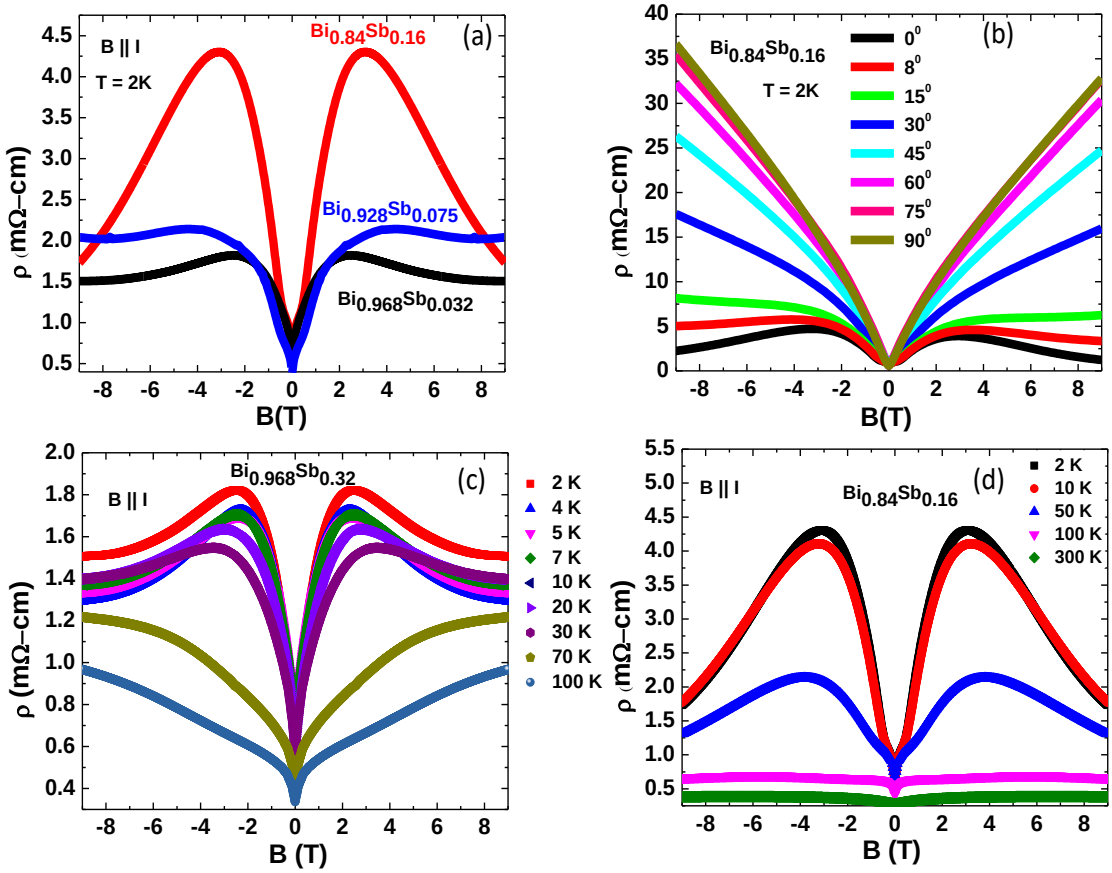

Figure 3.6: (a) Resistivity ρ vs magnetic field B at T = 2 K with B $\parallel$ I for $Bi_{1-x}Sb_x$ (x = 3.2, 7.5, 16 %). (b) ρ vs B at T = 2 K for the x = 16% sample with B applied at various angles to the current I. The negative LMR seen clearly for B $\parallel$ I is rapidly suppressed as the angle between B and I increases. Temperature dependence of the negative LMR for the (c) x = 0.032 and (d) x = 0.16 samples.

We have also measured the T dependence of the LMR for the $x = 3.2$ and 16% samples as shown in Figure 3.6 (c) and (d), respectively. The negative contribution to the LMR shows a strong T dependence and is suppressed for higher T. The NLMR is no longer observed for $T > 50$ K for $x = 0.032$ and $x = 0.16$.

Further confirmation of anomalous transport behaviour expected for a WSM is obtained for the $x = 0.16$ sample from the observation of a violation of the Ohm's law. Figure 3.7 shows the $I-V$ curve for the $x = 0.16$ sample measured at $T = 2$ K in $B = 0$ and in $B = 9$ T for $B \parallel I$. The $B = 0$ data are completely linear as expected in conventional metals. The $I-V$ data at $B = 9$ T with $B \perp I$ were also measured (not shown) and were found to be completely linear. For $B \parallel I$, the LMR configuration, a clear non-linearity can be seen in the $I-V$ curves. To highlight the non-linearity, we have subtracted the linear part of the $I-V$ curve obtained by a fit to the $I \leq 2$ mA data. The resulting $I-V$

curve obtained at 9 T is shown in Fig. 3.7 inset and clearly shows a non-linear behaviour. This clear violation of the Ohm's law has previously been reported only for the $x = 0.05$ samples close to the topological transition boundary [88].

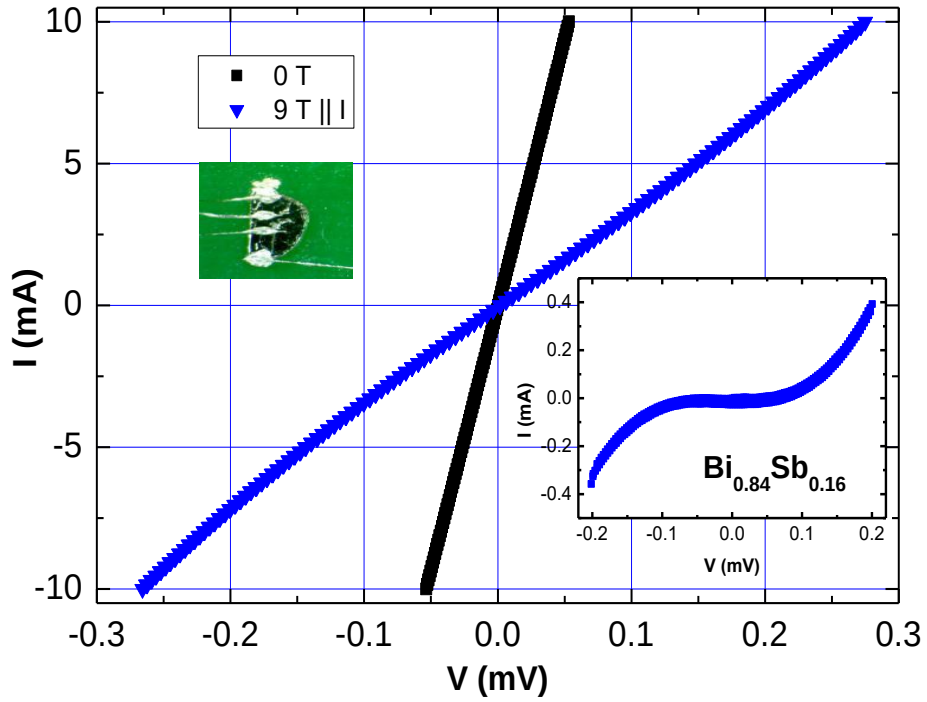

Figure 3.7: I–V curve for the x = 0.16 sample measured at T = 2 K in B = 0 and in B = 9 T for B || I.

3.4 Summary and Discussion

We have studied the detailed magneto-transport properties of $Bi_{1-x}Sb_x$ ($0 \leq x \leq .16$) across the trivial semimetal to topological insulator transition around $x \approx 0.04$. Giant magnetoresistance upto 1.6×10^5 % was observed at temperature T = 2.2 K in a magnetic field of H = 9 T, without any sign of saturation. We observed Shubnikov de Haas (SdH) oscillations in magneto-transport measurement for the doped crystals indicating their high quality. From a Landau fan diagram analysis of the quantum oscillation data we track the evolution of the Berry phase across the topological transition around $x \approx 0.04$. We find a non trivial Berry phase of for $Bi_{0.0925}Sb_{0.075}$, indicating the topological nature of the surface states. $Bi_{0.0968}Sb_{0.032}$ on the other hand shows a trivial Berry phase. The transition from trivial insulator to a TI occurs at $x \approx 0.03$. Samples at this topological phase tran-

sition are Dirac semi-metals (DSM) and the application of a magnetic field breaks time reversal symmetry and hence splits the Dirac cone into two opposite chirality Weyl cones displaced in momentum space along the field direction turning the material into a Weyl semimetal (WSM). A smoking gun signature of a WSM state is the observation of a chiral anomaly i.e. a negative longitudinal magnetoresistance (LMR) when a magnetic field B is applied along the current I direction. This negative LMR is expected to be strongly suppressed as the angle between B and I is increased. Additionally, a non-linear I – V has been reported for the WSM state at x = 0.05. We indeed observe the chiral anomaly for our x = 0.03 crystals in agreement with previous reports on samples with x = 0.04 and 0.05. Unexpectedly, we also find strong evidence of a WSM state for the x = 0.16 sample, which is close to the end of the TI state. In particular, we find a negative LMR even stronger than the x = 0.032 sample. The negative LMR is strongly suppressed with increasing angle between B and I. Additionally we observe a non-linear I-V for B $\parallel$ I but not for B $\perp$ I. A weaker but clearly observable negative LMR is also found for the x = 0.075 sample. These observations strongly indicate that in addition to x = 0.03, a WSM state exists for x = 0.075, 0.16 materials expected to be deep in the TI state. Sometimes current jetting may also cause the negative LMR signal. The issues of the current jetting and the crystal inhomogeneity has been ruled out in this study and the observations are indeed intrinsic. In order to avoid any contribution from current jetting to the negative LMR the contacts on the single crystals were made by high quality silver paint in a collinear geometry as shown in upper half of Fig. 3.7. Previous STM and ARPES results have shown a complex band structure in the bulk of these alloys for the compositions studied here. Our results suggest that these bulk bands host Weyl nodes which are responsible for the observation of the anomalous longitudinal magneto-transport properties including the chiral anomaly and violation of Ohm's law.

CHAPTER 4

Quantum oscillations and non trivial topological state in type-II Dirac semimetals ATe_2 (A = Pd, Pt).

4.1 Introduction

Recently, a new family of transition-metal dichalcogenide materials ATe_2 (A = Pd, Pt) were theoretically predicted to be type-II Dirac materials and subsequently experimentally confirmed by the ARPES. [25, 43, 46, 101, 102]. These semimetals are termed as type-II, because, unlike type-I TSM having isotropic linear E-K dispersion, the E-K dispersion in type-II TSMs is strongly tilted in one k-direction.This follows the discovery of type-II Weyl materials [40, 47, 103]. The general Hamiltonian (H(k)) for Dirac/Weyl semimetals can be written as a sum of potential energy term (U(k)) and a kinetic energy term T(k) which is given by $H(k) = U(k) \pm T(k)$. The type-I and type-II nature of Dirac and Weyl semimetals can be classify by relative magnitude of U(k) and T(k). For Lorentz invariance type-I DSMs/WSMs, $U(k) > T(k)$, and has linear and isotropic dispersion in the momentum space. On the contrary when $U(k) < T(k)$ along particular direction in momentum space, tilted Dirac cone is expected to appears at special symmetry points. The resulting electronic band structure consist of overlapping electron and hole pockets at Fermi level. The schematic of type-I and type-II TSMs is shown in Fig. 4.1 (a) and (b). Recent theoretical calculations combined with ARPES results provide the evidence that $PdTe_2$ and $PtTe_2$ can host type-II Dirac fermion lies at $k = (0, 0, \pm 0.4c^*)$ and $k = (0, 0, \pm 0.35c^*)$ respectively, where $c^* = 2\pi/c$ [45, 46]. The experimentally measured dispersion as a function of out of plane momentum (k_z) in $PtTe_2$ is shown in Fig. 4.1

(c), where a tilted Dirac cone was revealed at $k_z = 0.35c^*$ [46]. Both the type-II Weyl and Dirac fermions break Lorentz invariance and are therefore fundamentally different quasiparticles compared to the normal type-I Dirac and Weyl fermions discovered earlier. Type –II Dirac/Weyl semimetals are predicted to have some unique properties such as field dependent NMR and Klein tunneling [49, 50]. Both $PdTe_2$ and $PtTe_2$ are crystallize in a layered CdI_2 type crystal structure with $P\bar{3}m1$ (164) space group, which is shown in Fig. 4.2 (a) and (b). The crystal structure of these compound hold inversion symmetry and therefore bands are Kramers degenerate. The study of the properties of these type-II topological materials are therefore of immense fundamental interest and could lead to important technological applications. The linear Dirac dispersion in the bulk band structure can be probed by studying quantum

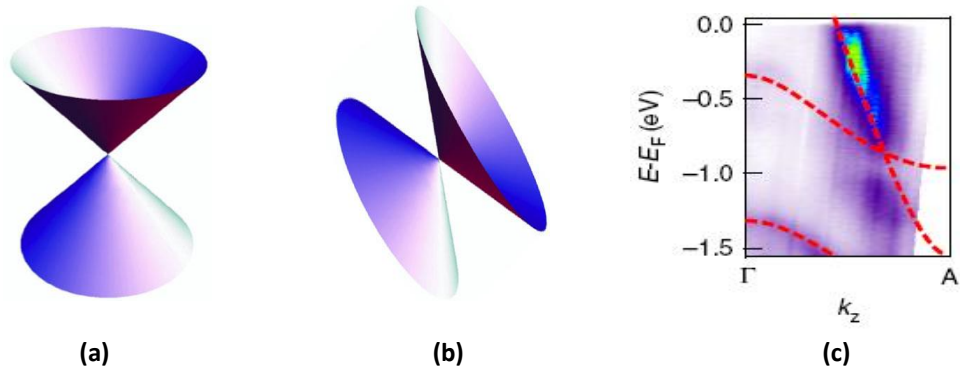

Figure 4.1: (a) and (b) Schematic of electronic structure of type-I and type-II Dirac semimetals. Fig(b) shows the tilted nature of the Dirac band. (c) Tilted Dirac cone measured by angle resolved photoemmission spectroscopy. The red dotted lines are theoretically calculated dispersions for comparison. Reproduced from **Nature communications 8, 257 (2017)**.

oscillations in transport experiments as has been demonstrated for graphene, topological insulators and recently in the Dirac and Weyl semimetals [30]. Previous quantum oscillation studies on Weyl and Dirac semimetals have demonstrated a connection between band topology and the phase acquired by the charge carriers. The wave function of a relativistic quasi-particle acquires a nontrivial geometric phase of π along the cyclotron orbits in a magnetic field, (also known as the π Berry phase), which can be calculated from the quantum oscillations in resistivity and magnetization measurements [30]. In the transition metal di-telluride family experimental work focusing on demonstrating the Type-II DSM nature has been mainly on $PtSe_2$, and Pd/PtSeTe compounds [101, 104, 105]. However, experimental evidence for the DSM nature of $PdTe_2$ and $PtTe_2$ are missing. There are some photoemission spectroscopy reports regarding tilted nature of the Dirac cone in $PtTe_2$ and $PdTe_2$, but detailed quantum oscillation studies on these compound are still

missing, which can help establish the three dimensional Dirac character of these compounds.

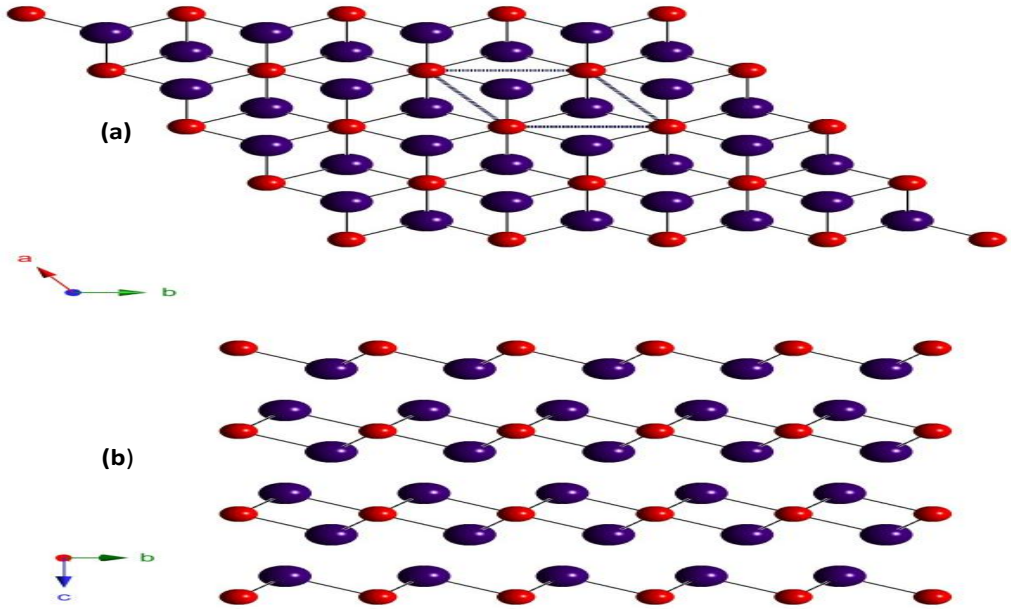

Figure 4.2: (a) and (b) Crystallographic structure of $PdTe_2$ and $PtTe_2$ via the atomic arrangements observed within the ab and bc planes, respectively. Here, the Pt/Pd and Te atoms are represented by red and blue spheres, respectively. Reproduced from **Phys. Rev. B 97, 235154 (2018)**.

In this chapter We present our detailed magneto-transport and quantum oscillations study on high quality single crystals of the transition metal di-tellurides $PtTe_2$ and $PdTe_2$.

4.2 Experimental Details

Single crystals of $PdTe_2$ were synthesized using a modified Bridgeman method. A typical crystal is shown on a millimeter grid in the inset of Fig. 4.11. High quality single crystals of $PtTe_2$ were grown by self flux method. The details of synthesis process has been provided in chapter 2. A typical crystal of $PtTe_2$ is shown on a millimetre grid in the inset of Fig. 4.4. The powder X-ray diffraction pattern obtained on crushed crystals of $PdTe_2$ and $PtTe_2$ confirms the phase purity and CdI_2 type crystal structure with $P\bar{3}m1$ (164) space group for both materials. The chemical composition and uniformity of stoichiometry for crystals of both compounds was confirmed by energy dispersive spectroscopy at several spots on the crystals used for the measurements reported in this work. The results of chemical analysis and powder x-ray diffraction for ATe_2 are shown

in Fig. 6.5. The goodness of fit (χ^2) values obtained after Rietveld refinement for $PdTe_2$ and $PtTe_2$ are 7 and 15 respectively. In the Rietveld refinement of $PtTe_2$ some unreacted peaks are obseved at approx. 28°, 33° and 38°. These unreacted lines are identified due to excess Te in $PtTe_2$ sample.This could be due the fact that the single crystals of $PtTe_2$ were grown by self-flux method, where Te act as a flux. The electrical transport and magnetic measurements (0-14 T) were performed on a physical property measurement system by Quantum Design (QD-PPMS).

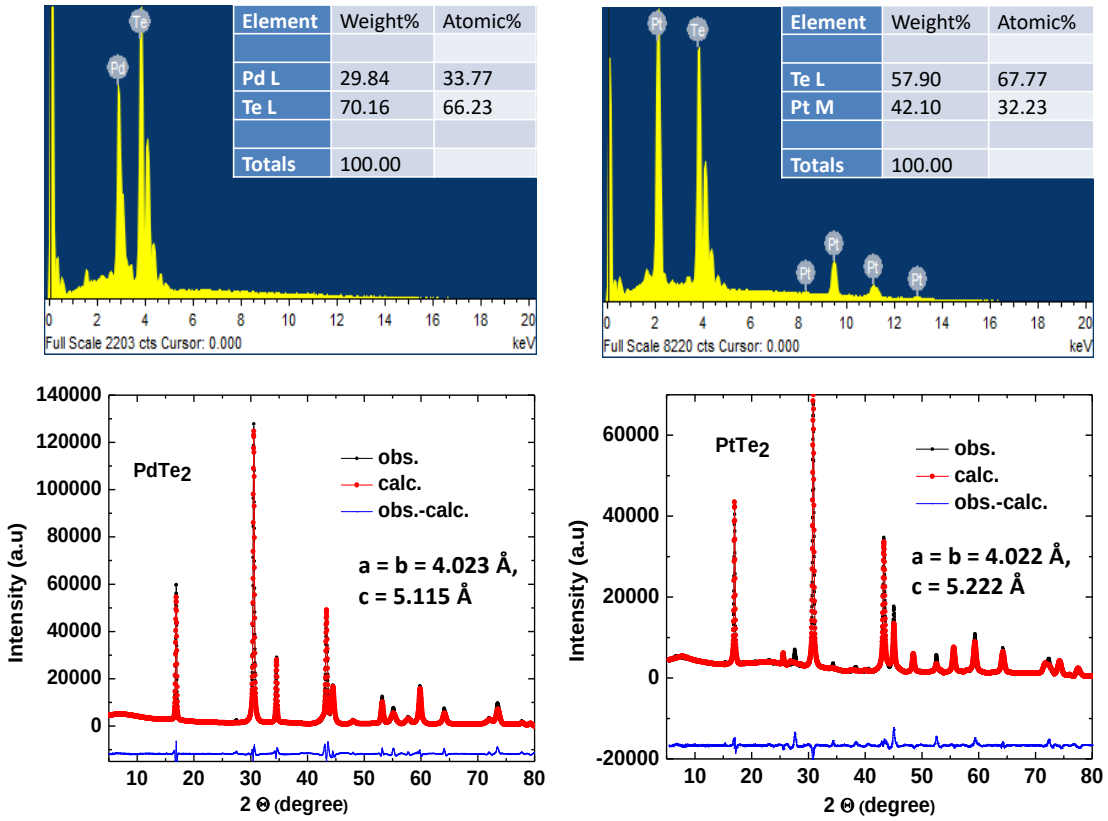

Figure 4.3: Results of chemical analysis (a1) and (a2) and powder x-ray diffraction (b1) and (b2) on $PdTe_2$ and $PtTe_2$, respectively.

4.3 Results

4.3.1 $PtTe_2$

Figure 4.4 shows electrical resistivity ρ versus temperature T for a single crystal of $PtTe_2$ measured with an ac current of amplitude $I = 2$ mA applied within the *ab*-plane of the crystal. Metallic behaviour is observed in the whole T range (1.8 K to 300 K) of measurements. The residual resistivity ratio RRR $= \rho(300\ K)/\rho(1.8\ K) \approx 96$ indicates

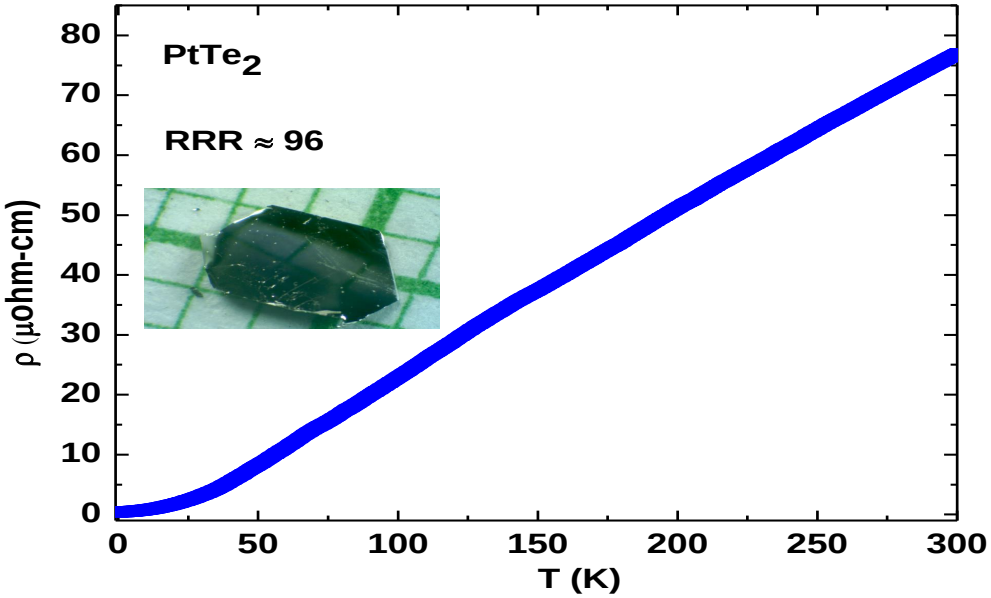

Figure 4.4: Temperature dependent electrical resistivity of $PtTe_2$ single crystal. A current I = 2 mA is applied in the crystallographic ab plane. Upper inset shows an optical image of a $PtTe_2$ crystal placed on a millimeter grid.

the high quality of the crystal. A high RRR has been regarded as an indication of relativistic charge carriers in three dimensional Dirac semimetals such as Cd_3As_2, NbAs, $PdTe_2$, NbP etc. [41, 106, 107, 108]. The top inset shows an optical image of an as-grown $PtTe_2$ crystal showing the hexagonal morphology of the underlying crystal structure.

Figure 4.5 shows the magneto resistance (MR) data on the $PtTe_2$ crystal. The main panel shows the magnetic field B dependence of the MR measured at $T = 2$ K as a function of the angle between $B \leq 9$ T and the direction of the electrical current I, which was always applied in the same direction within the *ab*-plane of the crystal. The MR for all angles increases monotonically and tends to a linear in B behaviour. The magnitude of MR reaches about 200% which is smaller than observed for other DSMs. We specifically point out that no negative contribution to the MR was observed for $B \parallel I$ indicating the absence of the Chiral anomaly. The MR as a function of $B \perp I$ at various temperatures T is shown in the inset of Figure 4.5 and shows that the magnitude of MR has a strong T dependence.

The isothermal magnetization M data for $PtTe_2$ plotted as dM/dB versus $1/B$ at different temperatures for magnetic fields $B \leq 14$ T applied along the c-axis ($B \parallel c$) and applied within the *ab*-plane ($B \parallel ab$) are shown in Figs. 4.6 (a1) and (b1), respectively. The raw M vs B data for the two field directions are shown in the insets. The magnetization data reveal pronounced dHvA oscillations starting from 4 T. The low onset field value of the quantum oscillations also point to the high quality of the $PtTe_2$ crystal. Pronounced

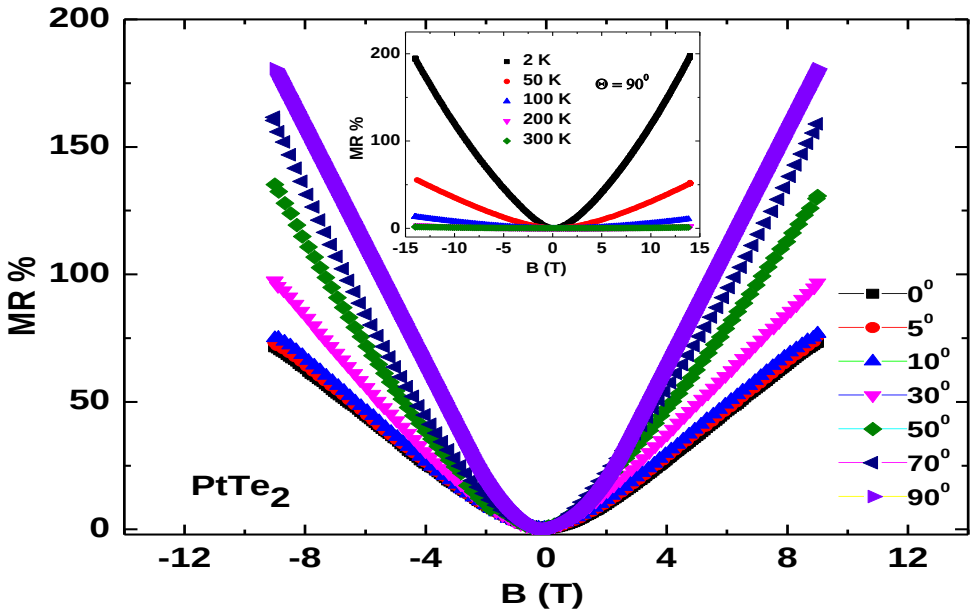

Figure 4.5: Magnetoresistance (MR) for $PtTe_2$ as a function of the magnetic field $B \leq 9$ T applied at various angles to the direction of the current I which was always applied within the ab-plane. Inset shows the MR measured at various T with $B \perp I$ for $B \leq 14$ T.

periodic oscillations as a function of $1/B$ are clearly visible up to 10 K in both field orientations. Multiple frequencies for both field orientations were observed in the fast Fourier transform (FFT) spectra of the quantum oscillations as shown in Figs. 4.6 (a2) and (b2). The multiple frequencies in the FFT spectra indicates the presence of multiple Fermi surface pockets at the Fermi level. Additionally, the presence of dHvA oscillations for both $B \parallel c$ and $B \parallel ab$ directions, confirms the presence of a three dimensional Fermi surface in $PtTe_2$. From the temperature dependent FFT spectra, we find four main frequencies for both $B \parallel c$ and $B \parallel ab$ as shown in Figs. 4.6 (a2) and (b2). The main frequencies for the $B \parallel c$ are labeled as α_1(93.3 T), α_2(108.9 T), α_3(241 T) and α_4(459 T). The main frequencies for $B \parallel ab$ are labelled β_1(116.6 T), β_2(140.6 T), β_3(194.5 T) and β_4(225.6 T). The information regarding the Fermi surface area corresponding to these frequencies can be determined by the Onsager relation $F = A_F(\varphi/2\pi^2)$, where $\varphi = h/e$, is the magnetic flux quantum and A_F is the Fermi surface area. The calculated Fermi surface area for the frequencies extracted for the two field orientations are listed in Table 5.4.

A quantitative analysis of the dHvA oscillations can be made using the Lifshitz-Kosevich (LK) equation which gives the oscillatory contribution to the magnetization as:

$$\Delta M \propto -R_T R_D \sin(2\pi[\frac{F}{B} - (\frac{1}{2} - \phi)]) \tag{4.1}$$

where, $R_D = exp(-\lambda T_D)$ is the Dingle factor, $T_D = \hbar/2\pi K_B \tau$ is the Dingle temper-

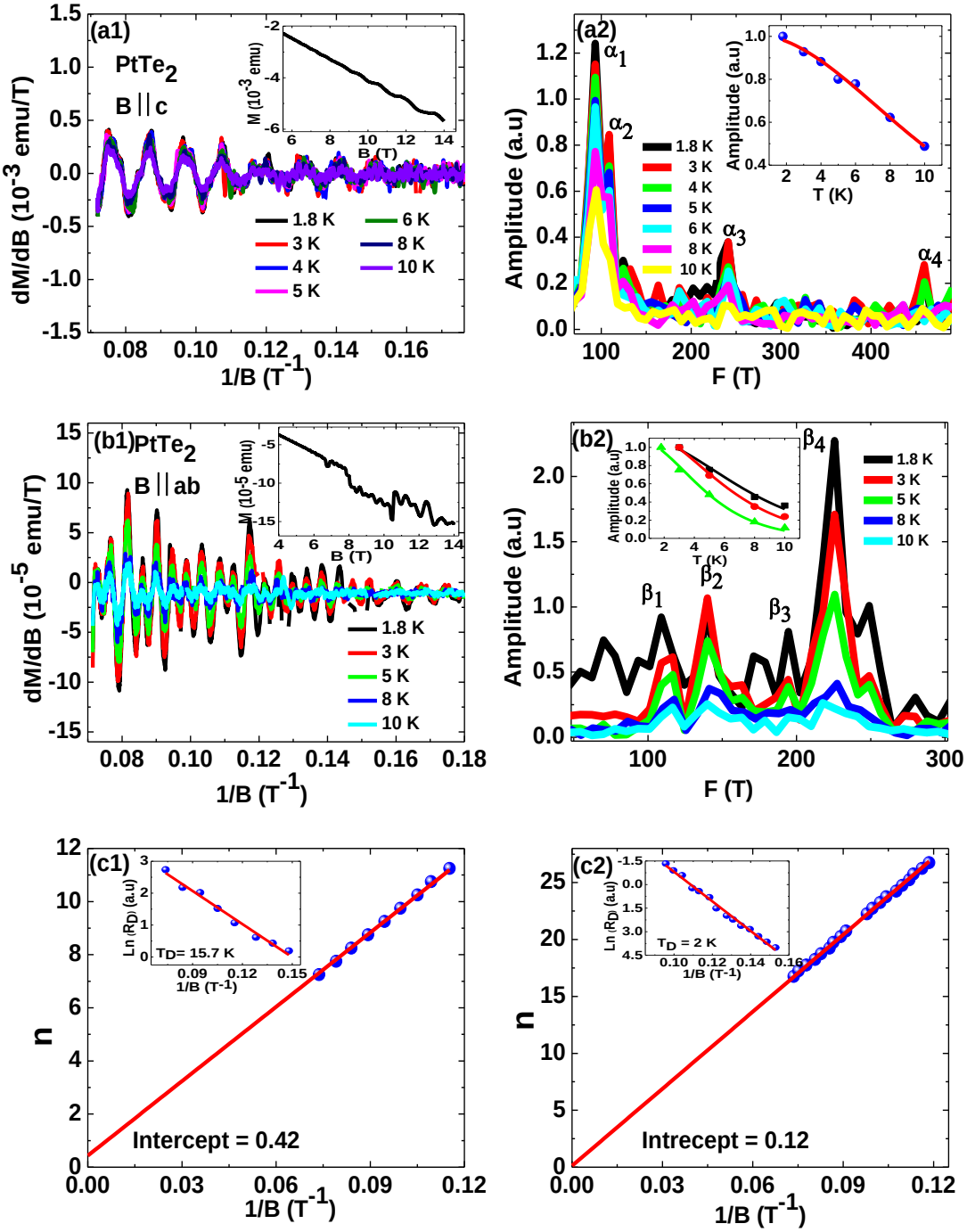

Figure 4.6: (a1 and b1)Isothermal magnetization oscillation data for $PtTe_2$ in the two directions $B \parallel c$ and $B \parallel ab$, at various temperatures.Inset shows row magnetization data at 1.8 K. (a2 and b2) shows the temperature dependence of FFT spectra and fitting of the temperature dependent amplitude is shown in the inset for the two cases. (c1 and c2) The landau level fan diagrams for the two cases. Inset shows the Dingle fitting.

ature, and the temperature dependent damping of the oscillations is accounted for by the factor $R_T = \lambda T/\sinh(\lambda T)$, with $\lambda = (2\pi^2 K_B m^*/\hbar eB)$ and m^* the effective cyclotron

Table 4.1: Fermi surface parameters for $PtTe_2$ obtained from the dHvA data shown in Figs. 4.6 (a2) and (b2)

Compound	F (T)	$A_f(^{-2})(10^{-2})$	$K_f(^{-1})(10^{-2})$	m^*/m	$v_f(m/s)(10^5)$	$E_f(meV)$
$PtTe_2, B \parallel c$	93.3	0.89	5.3	0.15 ± 0.004	4.1 ± 0.1	143 ± 5
	108.9	1	5.7	–	–	–
	241	2.3	8.6	–	–	–
	459	4.4	11.8	–	–	–
$PtTe_2, B \parallel ab$	116.6	1.1	5.96	0.21 ± 0.01	3.27 ± 0.2	127.5 ± 9
	140.6	1.3	6.54	0.26 ± 0.01	2.9 ± 0.1	124 ± 9
	194.5	1.9	7.7	–	–	–
	225.6	2.1	8.3	0.32 ± 0.01	3 ± 0.1	163.6 ± 11

.

mass. The phase $\phi = \phi_B/2\pi - \delta$, where ϕ_B is the Berry phase and δ is an extra phase factor. The value of this additional phase shift δ depends on the dimensionality of the Fermi surface and takes the value 0 or $\pm 1/8$ ($-$ for electron like and $+$ for the hole like) for two and three dimension, respectively [107, 109, 110].

The damping factors R_T and R_D can be used to calculate important band parameters such m^*, quantum life time τ and quantum mobility μ of the carriers. The values of τ (corresponding to Dingle temperature T_D) extracted from fitting of the B dependence (see inset of Figs. 4.6 (c1) and (c2)) of the oscillation amplitude are given in the Table 5.5. For $B \parallel c$ the value of $\tau = 7.7 \times 10^{-14}$ s, and for $B \parallel ab$, $\tau = 6.0 \times 10^{-13}$ s. The corresponding quantum mobility $\mu = e\tau/m^*$ in the two directions are estimated to be 902.0 cm^2/Vs and 3296 cm^2/Vs, respectively. These values of μ are comparable to values reported previously for some Dirac semimetals [46, 107, 109, 110, 111, 112]. The large difference in the mobility (more than a factor of three) in the two crystal orientations suggests that the dynamics of carriers in $PtTe_2$ is highly anisotropic with carriers in the c-axis direction being less mobile than in the ab-plane. This would be consistent with a tilted Dirac cone as a tilting of the cone in one momentum direction might result in strong anisotropy in the transport properties as observed above for $PtTe_2$.

The value of the effective mass for the two field orientations is found from the fitting of the temperature dependence of the amplitudes of the frequencies identified in the FFT spectra of the dHvA oscillations. The fitting shown in the insets of Figs. 4.6 (a2) and (b2) was successful only for certain frequencies as the amplitude dropped too rapidly with T for some frequencies. The effective masses thus obtained are listed in the Table 5.4. For $B \parallel c$ the value of the effective mass m^* corresponding to the frequency $\alpha_1 = 93.3$ T is 0.15. The low value of m^* for this frequency suggests the presence of relativistic charge carriers, which can further be confirmed by the Landau level fan diagram analysis which we present later. The values of m^* corresponding to frequencies in the $B \parallel ab$ orientation

Table 4.2: Parameters obtained from a Dingle fitting of the dHvA data shown in Fig. 4.6

Compound	$T_D(K)$	$\tau(10^{-13}s)$	l (nm)	$\mu(cm^2/V-s)$
$PtTe_2, B \parallel c$	16 ± 1	0.77 ± 0.06	32 ± 4	902 ± 87
$PtTe_2, B \parallel ab$	2 ± 0.1	6 ± 0.4	180 ± 21	3296 ± 386

.

are relatively larger in magnitude as listed in Table 5.4.

We now present a Landau fan diagram analysis to estimate the Berry phase. The presence of multiple frequencies (from multiple Fermi surface orbits) in the quantum oscillations makes it difficult to isolate contributions to the Berry phase from individual orbits. We therefore take in to account the frequencies with the largest FFT amplitudes ($\alpha_1 = 93.3$ T for the $B \parallel c$ and $\beta_4 = 225.6$ T in case of $B \parallel ab$) as shown in the Figs. 4.6 (a2) and (b2). To construct the Landau level fan diagram we assign the landau index $n - 1/4$ to the minima of quantum oscillations. We are able to reach the 7^{th} landau level in the $B \parallel c$ and 16^{th} landau level for the $B \parallel ab$ configuration as shown in the Figs. 4.6 (c1) and (c2). The extrapolated value of the intercept ($= \phi_B/2\pi \pm \delta$) on the n axis is found to be $0.42(2)$ and $0.12(3)$ for $B \parallel c$ and $B \parallel ab$, respectively. The slopes obtained from the fits are 94.7 T and 228.2 T for the two directions. These slopes are very close to the frequencies of the α_1 and β_4 orbits, proving that we are analysing these orbits in the Landau level fan diagram [30]. From the value of the intercepts found above the estimated Berry phase for $B \parallel c$ and $B \parallel ab$ directions are $1.08(4)\pi$ [or $0.59(4)\pi$] and $0.49(6)\pi$ [or $-0.01(6)\pi$], respectively. The value $\phi_B = 1.08(4)\pi$ for the α_1 orbit in $B \parallel c$ direction is very close to the value π expected for Dirac electrons. Whereas, the value $\phi_B = 0$ for $B \parallel ab$ suggests that the orbit β_4 is trivial. A possible reason for the trivial character of bands in the $B \parallel ab$ direction can be the nonlinear nature of the bands owing to the Fermi level being away from the Dirac point. We will discuss the validity of these numbers in our discussion section later.

Owing to the deeply rooted Dirac points below the Fermi level in the $PtTe_2$ (0.8eV), we could not observe chiral anomaly induced negative MR, however, the Dirac nature is confirmed by the extracted Berry phase of π in the transport experiments. In the following we present the observation of planar Hall effect (PHE) in $PtTe_2$ single crystals.

The appearance of the transverse voltage in the conductors and semiconductors in the presence of a external magnetic field applied perpendicular to the plane is well understood in terms of the Lorentz force acting on the charge carriers, and is a versatile tool for determining the nature and density of the carriers in a specimen. This effect is known as the ordinary Hall effect, and the origin and physics of this effect is well understood. Another version of the ordinary Hall effect, the quantum Hall effect and (quantum) anomalous Hall

effect (does not require magnetic field) can not be understood in the same framework as driven by the Lorentz force only [113, 114]. These quantization effects are not sensitive to the local details of the sample, material type and more importantly the disorder strength. These properties of the quantum Hall/anomalous effect, observed in various classes of the materials, led to the discovery of the new classification scheme of the insulators, superconductors and metals based on the quantized topological invariants of the bulk band structure [2, 115].

Recently an unconventional version of the Hall effect, known as planar Hall effect (PHE) has been theoretically proposed as a signature of the chiral anomaly in topological semimetals, the origin of which is the large Berry curvature between a pair of Weyl node [29, 61, 64, 116, 117]. The Berry curvature in the energy-momentum space for TSMs acts like an intrinsic magnetic field, which in turn affects the charge carrier dynamics in an unusual way. Unlike ordinary Hall effect, the PHE does not require a perpendicular magnetic field, and a transverse voltage is generated by the application of a magnetic field, applied in the plane of the sample/current. While a small PHE has been reported for ferromagnetic semiconductors and semimetals, PHE has recently been experimentally observed in several classes of magnetic and nonmagnetic Dirac and Weyl semimetals (DSM and WSM) [118, 119, 120, 121, 122, 123, 124, 125, 126]. The origin of PHE effect in these ferromagnets has been attributed to several microscopic phenomenon, including spin Hall magnetoresistance, anisotropic scattering by the impurities and non-spherical Fermi surface. On the other hand PHE in topological materials has its origin in the finite Berry curvature of the nontrivial bands in the bulk. The PHE could be an intrinsic and universal effect like anomalous Hall effect. Experimental observation of the all three effects, chiral anomaly driven negative MR, anomalous Hall effect and PHE, in nonmagnetic topological semimetal $ZrTe_5$, strongly suggests a common and intrinsic origin of these phenomena [122, 127, 128].

The chiral anomaly induced NMR character in TSMs may appears due to many other extrinsic effects. These effects include primarily current jetting and chemical inhomogeneity in the crystals with a very high mobility such as frequently observed in the topological semimetals. For instance, the NMR in the coplanar and collinear current and magnetic fields (chiral anomaly) has been observed, despite the fact that the chirality of the band structure is not well defined, i.e, the chemical potential is very far away from the Weyl nodes [64, 117, 129, 130, 131]. Therefore the signature of chiral anomaly by negative longitudinal MR is still under debate. These experimental complexities, on the other hand, do not affect the signature of the PHE in a topological semimetal and the response of the topological bands has been detected by this effect [132]. This led us to believe that topological bands could manage to contribute in transport measurements, even in cases

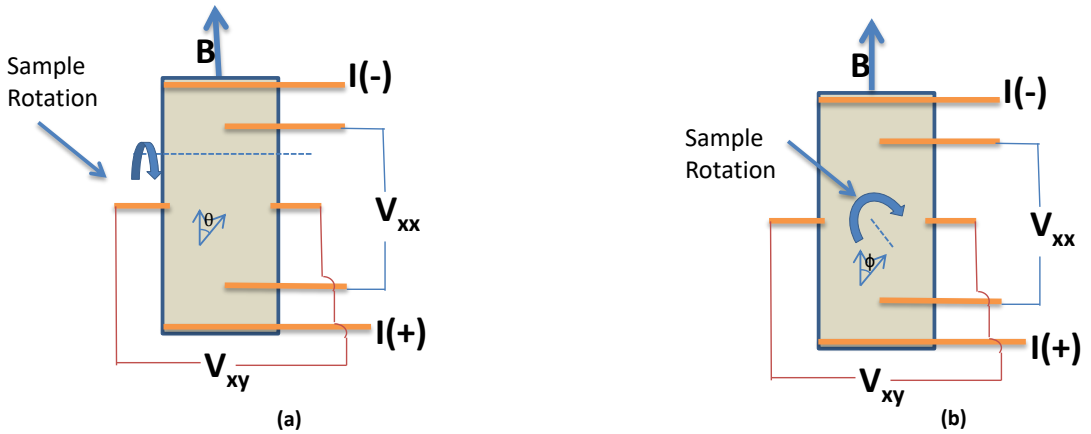

Figure 4.7: (a) and (b) Schematic diagram for the normal and PHE measurements respectively. In normal Hall effect B changes direction from in plane to out of plane during θ rotation while in PHE, B always remain in plane, during ϕ rotation.

when the Dirac or Weyl node is located slightly away from the Fermi energy. For example, in metallic topological insulators quantum oscillation are observed from surface Dirac states although the chemical potential lies in the bulk conduction/valance bands [133, 134, 135].

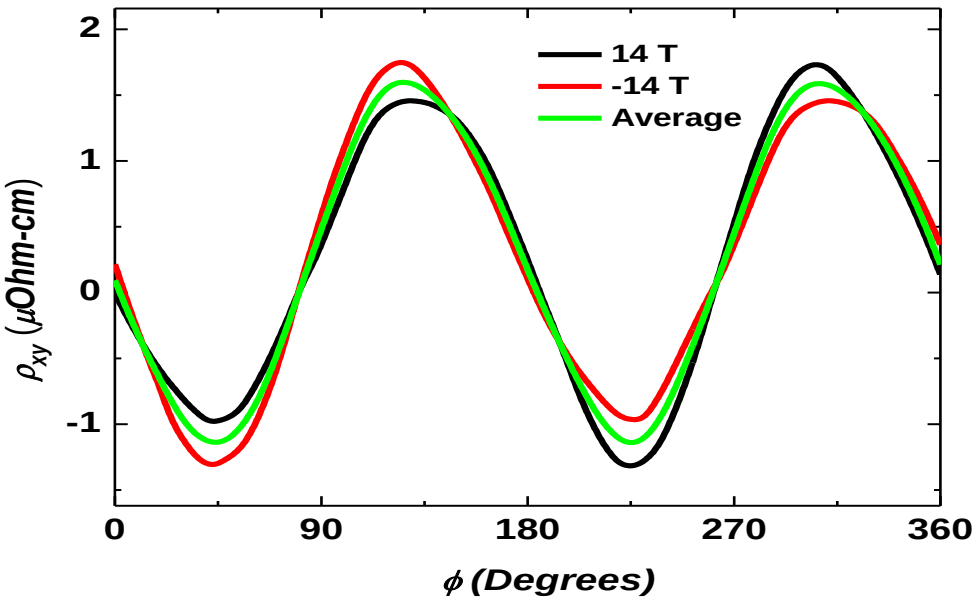

Figure 4.8: Measured planar Hall resistivity at two opposite field (14 & -14 T) at 2 K and their averaged value.

The measurement geometry and the field configuration for the normal Hall effect and

PHE is shown in the figure 4.7 (a) and (b) respectively. The magnetic field B is applied in the plane of the current I and the angle between B and I is controlled by rotating the sample in the plane made by B and I as shown in figure 4.7 (b). The planar Hall resistivity (ρ_{xy}^{PH}) and the planar anisotropic MR (ρ_{xx}) are measured simultaneously. Contributions from the normal Hall effect can arise due to a small misalignment of the sample plane with respect to the magnetic field. The measurements of the two resistivities is performed in both negative and positive magnetic field polarities and is subsequently averaged and thus any stray contribution from the normal Hall resistivity is removed. A typical raw data in negative and positive magnetic field polarity and the averaged data as a function of the in plane angle (between the coplanar magnetic field and the current) at 14 T is shown in figure 4.8.

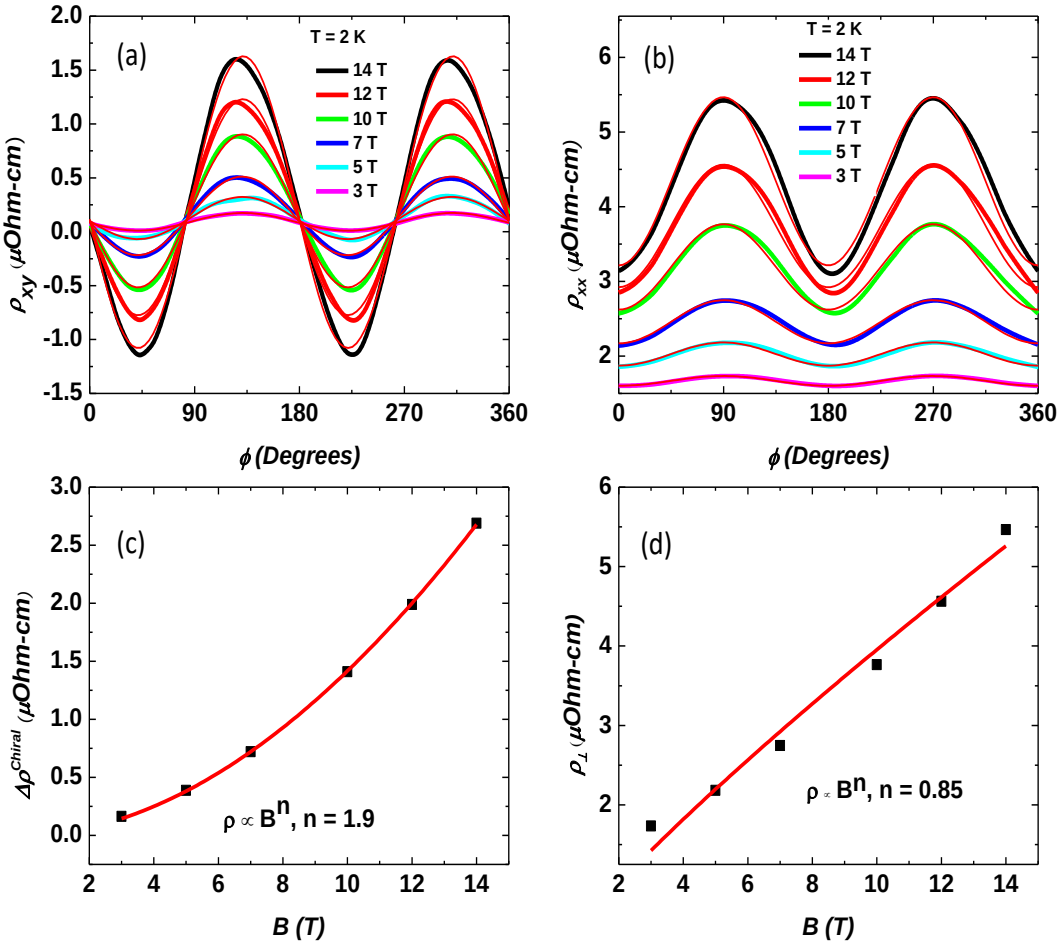

Figure 4.9: (a) and (b)In plane angular dependence of symmeterized planar hall resistivity(ρ_{xy}^{PH}) and longitudinal resistivity(ρ_{xx}) at different field at 2 K. These curves are fitted by equation 4.2 and equation 4.2, as shown by red curves. (c) & (d) Extracted values of $\triangle\rho_{chiral}$ and $\rho_{\perp}$ plotted vs magnetic field respectively. The data is fitted with power law.

The field dependent ρ_{xy}^{PH} and ρ_{xx} at 2 K is shown in the figure 4.9 (a) & (b). It is clear from the data in the figure 4.9 (a) that ρ_{xy}^{PH} has distinct minima and maxima at the in plane angular positions ϕ = 45°and 135°, respectively. On the other hand the variation of the anisotropic MR ρ_{xx} as a function of ϕ, shows characteristic maxima and minima at 90°and 180°as expected theoretically. Moreover, a phase difference of 45°between the ρ_{xy}^{PH} - ϕ and ρ_{xx} - ϕ curves is consistent with theoretical predictions. This observation is consistent with the previously observed PHE data on the ferromagnetic semiconductors and other Dirac and Weyl semimetals, such as $ZrTe_5$, GdPtBi, Cd_3As_2, VAl_3, $MoTe_2$ and $Co_3Sn_2S_2$ [118, 119, 120, 121, 122, 123, 124, 125, 126]. The value of the ρ_{xy}^{PH} increases with increasing magnetic fields up to 14 T, and reaches value of 1.61μOhm-cm. This value is quite large in comparison to the values calculated in the ferromagnets, and comparable to the values found in the recent experiments on some of the DSMs and WSMs [118, 124]. However, this value is relatively smaller in comparison to the ρ_{xy}^{PH} values found in GdPtBi and $ZrTe_5$ [121, 122], which could be due to the fact that the chemical potential lies near to the Dirac point in these topological semimetals. On the other hand Dirac point in $PtTe_2$ is located 0.8eV below the Fermi level, which could be lowered by Ir doping.

In order ot estimate the chiral anomaly contribution $\triangle\rho_{chiral}$ in the measured ϕ dependent ρ_{xy}^{PH} and ρ_{xx} data, we fit the data with the theoretically derived semiclassical expressions of the two resistivities which are given as: [65]

$$\rho_{xy}^{PH} = -\triangle\rho^{chiral}\sin\phi\cos\phi + b\cos^2\phi + c \tag{4.2}$$

$$\rho_{xx} = \rho_{\perp} - \triangle\rho^{chiral}\cos^2\phi \tag{4.3}$$

The first term in equation 4.2 represents the contribution to ρ_{xy}^{PH} from the chiral anomaly. The $\triangle\rho_{chiral}$ = $\rho_{\perp}$ - $\rho_{\parallel}$, with $\rho_{\perp}$ and $\rho_{\parallel}$ being the resistivities in the plane transverse (ϕ = 90°) and parallel (ϕ = 0°) magnetic fields, respectively. The second term in the equation 4.2 takes into account the possible contribution of the anisotropic MR which might arises from misalignment effects in the measurements and the third term c accounts for the constant Hall resistivity resulting from the nonuniform thickness of the sample [122]. The fitting by the above equations to the ρ_{xy}^{PH} - ϕ and ρ_{xx} - ϕ curves at different fields is shown as the solid curves through the data in figure 4.9 (a) & (b). The extracted value of the $\triangle\rho_{chiral}$ and the transverse resistivity $\rho_{\perp}$, from the fits is plotted as a function of the magnetic field in the figure 4.9 (c) & (d), respectively. As expected, the value of the $\triangle\rho_{chiral}$ and $\rho_{\perp}$ increases with increasing magnetic field. The value of the $\triangle\rho_{chiral}$ at 2 K, and in 14 T is found to be 2.688 μOhm-cm. To quantify the variation of $\triangle\rho_{chiral}$ and

$\rho_\perp$ with magnetic field we have fitted these data by power-law dependence. On fitting the $\triangle\rho_{chiral}$ data with the power law function ($\triangle\rho_{chiral} = B^n$) [123], we find the value of n = 1.9(2) which is close to a quadratic field dependence. This is consistent with theoretical expectations. Similar values of the power law coefficient n has been found in many other DSM and WSM. On the other hand the value of the coefficient n in the case of $\rho_\perp$ vs magnetic field is not near to n = 2, and varies linearly. The possible reason for this variation are not known yet, and similar dependence has been observed in some of the other WSMs.

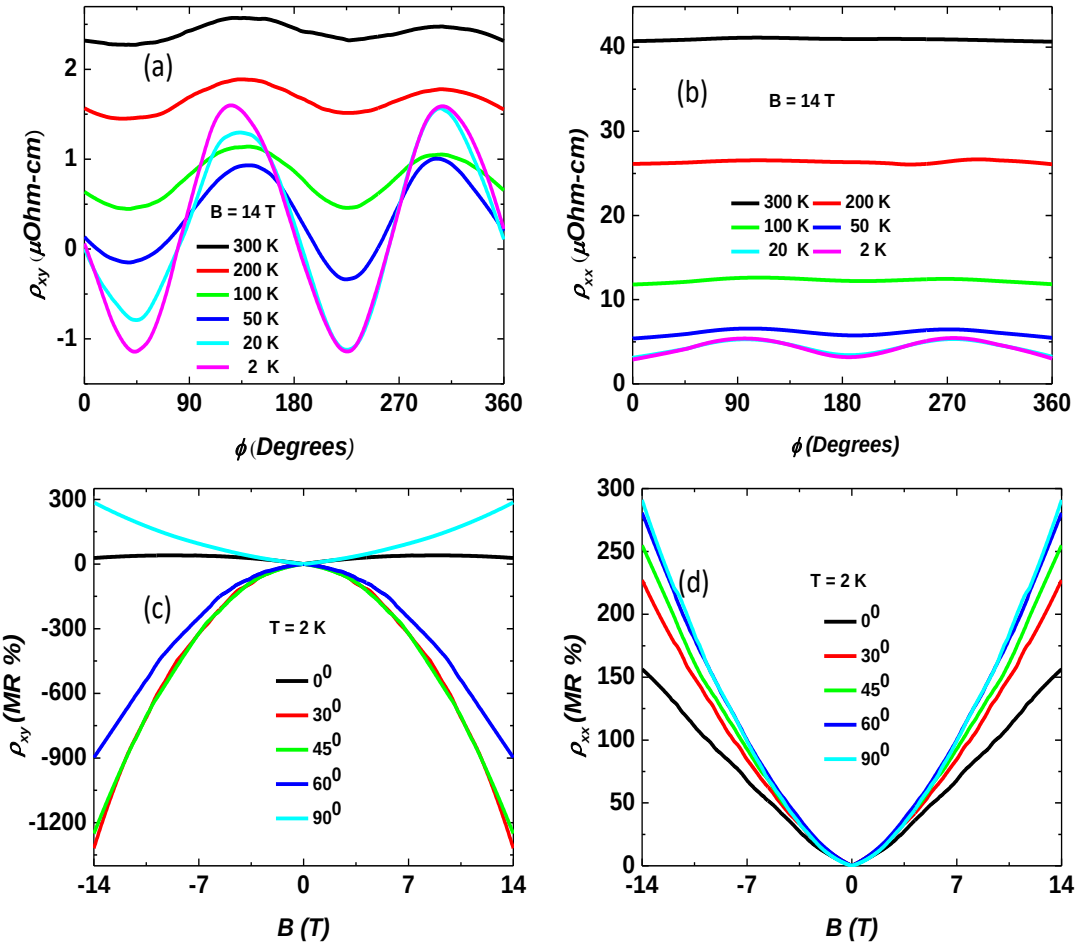

Figure 4.10: (a) & (b) Angular dependence of unsymmeterized planer hall resistivity (ρ_{xy}^{PH})and longitudinal resistivity (ρ_{xx}) at different temperature at magnetic field 14 T. (c) & (d)The symmeterized ρ_{xy}^{PH} and ρ_{xx} at 2 K.

We next investigate the robustness and the intrinsic nature of the PHE, by taking the temperature dependent ρ_{xy}^{PH} - ϕ and ρ_{xx} - ϕ data at maximum applied magnetic field of 14 T. It is clear from the data shown in the figure 4.10 (a) that PHE survives up to a room temperature, whereas the magnitude of ρ_{xx} - ϕ decreases rapidly with T as can be seen from figure 4.10 (b). The periodic nature of the ρ_{xy}^{PH} - ϕ curves is nearly maintained up

to room temperature and is not destroyed by the electron -phonon scattering. This is due to the fact that the topological and the chiral nature of the Dirac/Weyl electrons makes them immune to the backscattering from the defects and the other electron-electron and electron-phonon scattering mechanism. This is also why such topological systems show very large mobility and MR. The observation of PHE up to high temperature thus confirms the intrinsic nature of this effect which is driven by the large Berry curvature between the Weyl nodes. Recent observation of the chiral anomaly induced negative MR, anomalous Hall effect and PHE in GdPtBi, $Co_3Sn_2S_2$ and nonmagnetic $ZrTe_5$, strongly suggest that all three phenomena have a common, intrinsic origin. Moreover, it is a direct indication that the PHE does not require the ferromagnetic nature of the sample and previously observed PHE in semiconducting and metallic ferromagnets might have the origin from the Berry curvature effect.

Figure 4.10 (c) & (d) show the magnetic field dependence of the two in plane resistivities measured at various fixed angles ϕ and at temperature of 2 K. On varying the angle from 0°to 90°, the magnitude of the ρ_{xy}^{PH} first increases and then decreases, which is a hallmark signature of the PHE as expected theoretically. The in plane anisotropic nature of the ρ_{xx} is evident from the field dependent measurements at various in plane ϕ, as shown in the figure 4.10 (d). On the other hand, we could not resolve the negative MR in the coplanar and collinear current and magnetic fields configuration. This can be seen from the figure 4.10 (d).

4.3.2 $PdTe_2$

In order to compare the Dirac nature of the bands in $PtTe_2$ with that in $PdTe_2$, we have performed similar magneto-transport measurements and analysis on $PdTe_2$ single crystals. Figure 4.11 shows electrical resistivity ρ versus temperature T for a single crystal of $PdTe_2$ measured with an ac current of amplitude $I = 2$ mA applied within the *ab*-plane of the crystal. Metallic behaviour is observed in the whole T range (1.8 K to 300 K) of measurements. The residual resistivity ratio RRR $= \rho(300\ K)/\rho(1.8\ K) \approx 238$ indicates the high quality of the crystal. The top inset shows an optical image of an as-grown $PdTe_2$ crystal.

Figure 4.12 shows the magneto resistance (MR) data on a $PdTe_2$ crystal. The main panel in Fig. 4.12 shows the magnetic field dependence of the MR measured at $T = 2$ K as a function of the angle between $B \leq 9$ T and the direction of the electrical current I, which was always applied in the same direction within the *ab*-plane of the crystal. The MR for all angles increases monotonically with B. The magnitude of MR reaches large values of about 600% for $B \perp I$. As for $PtTe_2$, no negative contribution to the MR was

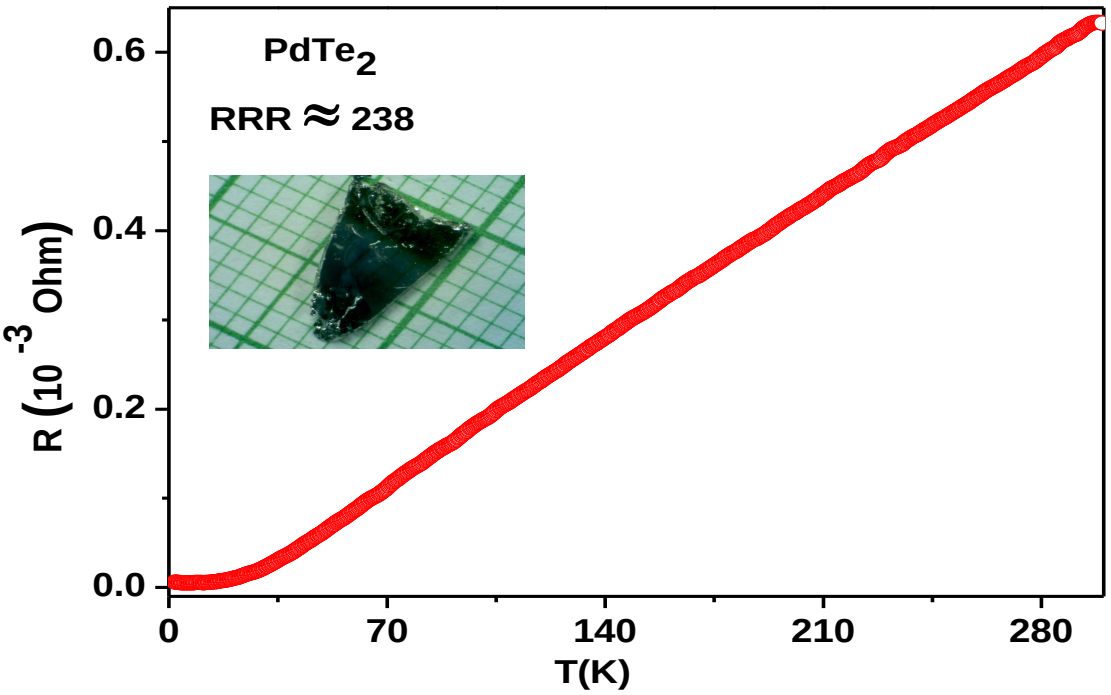

Figure 4.11: Temperature dependent electrical resistivity of $PtTe_2$ single crystal. A current I = 2 mA is applied in the crystallographic ab plane. Upper inset shows an optical image of a $PtTe_2$ crystal placed on a millimeter grid.

observed for $B \parallel I$ indicating the absence of the Chiral anomaly. The MR as a function of $B \perp I$ at various temperatures T is shown in the inset of Figure 4.5 and shows that the magnitude of MR has a very strong T dependence dropping drastically as one increases T from 2 K.

Figure 4.13 shows the magnetic field dependence of the magnetization data for $PdTe_2$ for both $B \parallel c$ and $B \parallel ab$ directions, measured at different temperatures. Figures 4.13 (a1) and (b1) show the pronounced dHvA oscillations for both directions of magnetic field. It should be noted that the amplitude of the quantum oscillations in $PdTe_2$ is relatively larger than in $PtTe_2$ single crystals and persist up to a temperature more than 30 K. The presence of the multiple frequencies in the two field orientations indicates an even more complex bulk band structure for $PdTe_2$ consisting of multiple Fermi pockets at the Fermi level.The FFT of the oscillations are shown in Figs. 4.13 (a2) and (b2) and reveal six main frequencies for $B \parallel c$ which we label as χ_1(9.13 T), χ_2(112.7 T), χ_3(231.5 T), χ_4(456.9 T), χ_5(913.9 T), and χ_6(2568 T), and 3 major frequencies for $B \parallel ab$ which we label as η_1(435.8 T), η_2(889 T), and η_3(1030.5 T) respectively. The calculated effective masses for the different frequencies for $B \parallel c$ are listed in Table 4.3 and lie in the range 0.14–0.43. The value of the cross sectional area calculated using the Onsager relation for the lowest effective mass Fermi orbit χ_1 comes out to be 0.87×10^{-3}, which is very

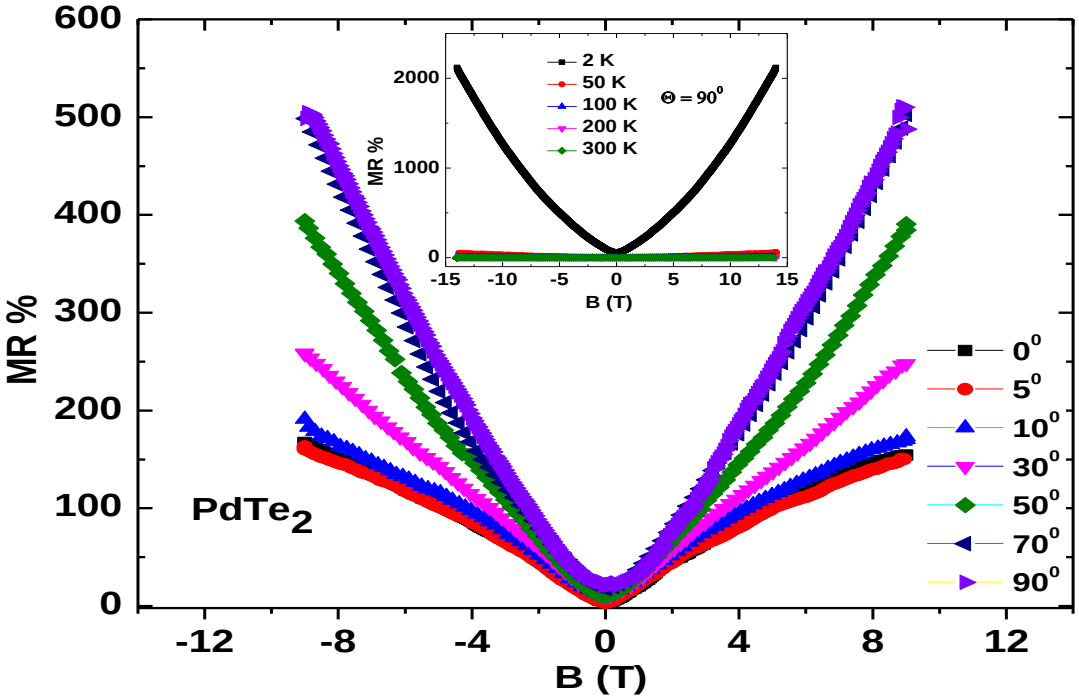

Figure 4.12: Magnetoresistance (MR) for a $PdTe_2$ single crystal as a function of the magnetic field $B \leq 9$ T applied at various angles to the direction of the current I which was always applied within the *ab*-plane. Inset shows the MR measured at various T with $B \perp I$ for $B \leq 14$ T.

small compared to the area for other orbits observed for $B \parallel c$. The value of the lowest effective mass for the $B \parallel ab$ direction is found to be 0.26 which is higher than estimated for $B \parallel c$ direction. Despite the difference in the effective masses in the two directions, the mobility calculated from a Dingle fitting for the two directions are very similar as shown in Table 4.4, in sharp contrast to the case of $PtTe_2$. These results are consistent with a recent magnetization and ARPES study on the $PdTe_2$ single crystals [44].

The Landau level fan diagrams for the two directions are given in Figs. 4.13 (c1) and (c2). The intercepts are $0.36(2)$ and $0.48(2)$ for $B \parallel c$ and $B \parallel ab$, respectively. The corresponding values of the Berry phase are $\phi_B = 0.97(4)\pi$ [or $0.47(4)\pi$] and $1.21(4)\pi$ [or $0.71(4)$] for $B \parallel c$ and $B \parallel ab$. The value ϕ_B for $B \parallel c$ is very close to π. The Berry phase for $B \parallel ab$ deviates from the value π. We note that the Fermi level in $PdTe_2$, like in $PtTe_2$, is too far above from the 3D Dirac point which is observed in the ARPES measurements [44, 45, 46, 104].

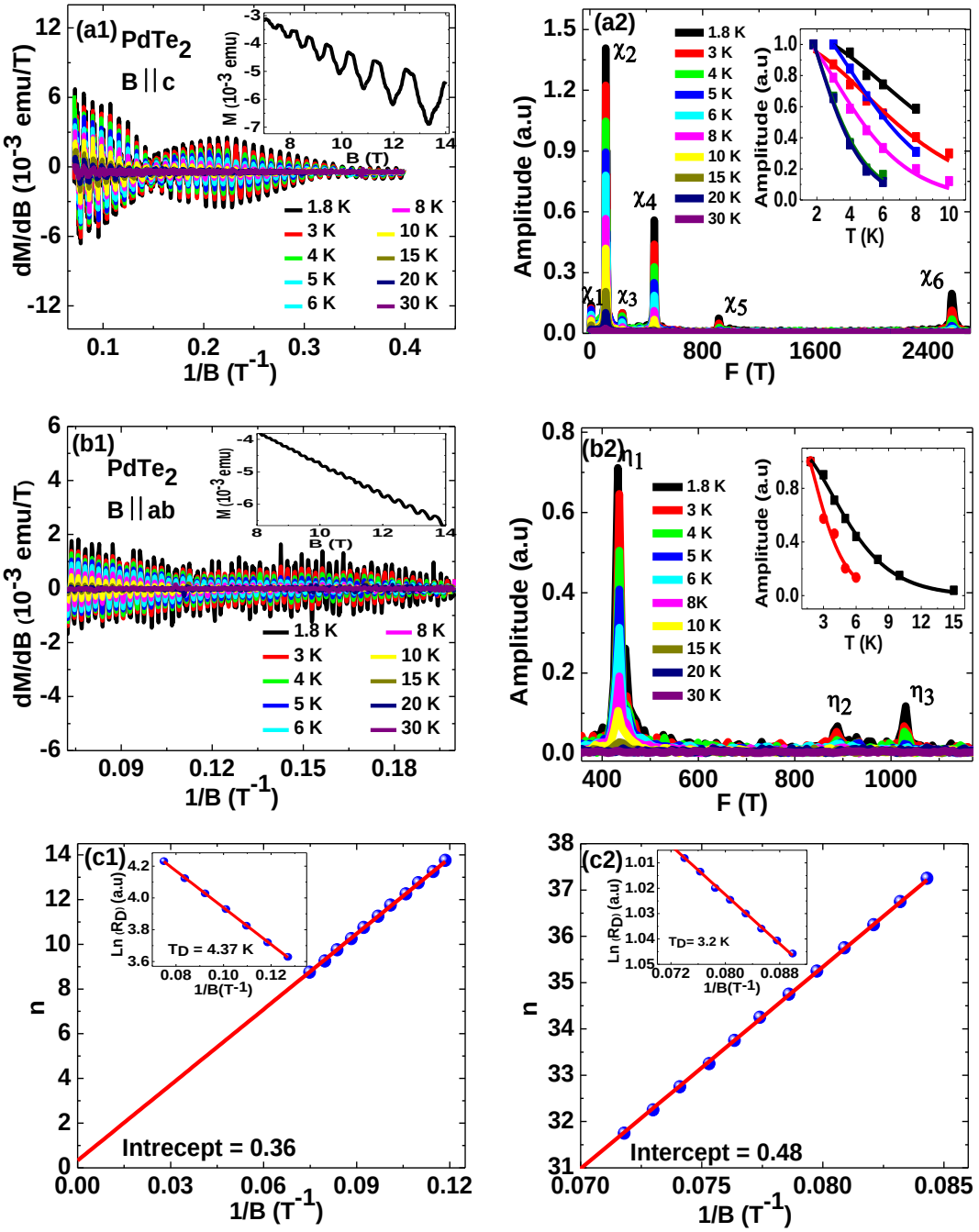

Figure 4.13: (a1 and b1) Similar set of magnetization data for $PdTe_2$. Magnetization oscillation data for $PdTe_2$ in the two directions $B \parallel c$ and $B \parallel ab$, at various temperatures. Inset shows row magnetization data at 1.8 K. (a2 and b2) shows the temperature dependence of FFT spectra and fitting of the temperature dependent amplitude is shown in the inset for the two cases. (c1 and c2) The landau level fan diagrams for the two cases. Inset shows the Dingle fitting.

Table 4.3: Fermi surface parameters for $PdTe_2$ obtained from the dHvA frequencies shown in Figs. 4.13 (a2) and (b2)

Compound	F (T)	$A(^{-2})(10^{-2})$	$K_f(^{-1})(10^{-2})$	m^*/m	$v_f(m/s)(10^5)$	$E_f(meV)$
$PdTe_2, B \parallel c$	9.13	0.087	1.7	0.14 ± 0.01	1.4 ± 0.1	15.58 ± 1
	112.7	1.1	5.84	0.18 ± 0.01	3.7 ± 0.1	139.97 ± 7
	228.7	2.2	8.4	0.22 ± 0.01	4.4 ± 0.2	241.9 ± 15
	456.9	4.37	11.8	0.27 ± 0.01	5 ± 0.2	383.4 ± 19
	913.9	8.75	16.7	0.41 ± 0.01	4.7 ± 0.2	514 ± 27
	2568	24.6	28	0.43 ± 0.02	7.5 ± 0.3	1373.9 ± 73
$PdTe_2, B \parallel ab$	435.8	4.17	6.5	0.26 ± 0.0098	2.9 ± 0.1095	124 ± 7.003
	889	8.5	16.5	–	–	–
	1035.5	9.8	17.7	0.46 ± 0.02	4.4 ± 0.2	505.8 ± 32

Table 4.4: Parameters obtained from a Dingle fitting to the dHvA data shown in Fig. 4.13

Compound	$T_D(K)$	$\tau(10^{-13}s)$	l (nm)	$\mu(cm^2/V-s)$
$PdTe_2, B \parallel c$	4.37 ± 0.1796	2.8 ± 0.11507	103.6 ± 7.883	2735 ± 112.43
$PdTe_2, B \parallel ab$	3.2 ± 0.1704	3.8 ± 0.2024	110 ± 10.01	2570 ± 233.9

4.4 Discussion and Conclusion

We have presented a detailed magneto-transport study on single crystals of the di-Tellurides $PtTe_2$ and $PdTe_2$ with an emphasis on trying to ascertain the possible topological nature of the bands contributing to the transport. Prominent dHvA quantum oscillations are observed for both materials in both directions of applied magnetic fields. From an analysis of the magnetization data on the two materials, it is found that the Fermi surface of both systems is highly anisotropic in nature which is evident from the different number of the oscillation frequencies in the two field directions. Additionally for $PtTe_2$ a very large difference in the value of the mobility (more than three times) in the two crystal orientations is observed and would be consistent with expectations of highly anisotropic transport resulting from the tilted nature of the Dirac cone in the $PtTe_2$. The Berry phase for $PtTe_2$ is close to π for $B \parallel c$ while it deviates from π for $B \parallel ab$. We speculate that this could be due to a combination of the Fermi level being away from the Dirac point and the presence of other topologically trivial bands at the Fermi level. This anisotropy is almost absent in case of $PdTe_2$ as the calculated mobility in the two crystal orientations is of the same magnitude. The bands in $PdTe_2$ are indeed three dimensional Dirac bands characterized by the Berry phase close to π in both in plane and out of plane crystal orientations.

A word of caution is in order here. An unambiguous identification of the Berry phase from quantum oscillations is complicated for systems with multiple bands making up the Fermi surface resulting in multiple frequencies in the oscillation data. Each frequency

will contribute to the phase. The analysis is further complicated if the Dirac node sits away from the Fermi energy. Additionally, if one ends up with a large Landau band index n in the Landau fan diagram analysis, then a larger extrapolation is required to reach the quantum limit to determine the intercept and hence the phase. This results in a larger error in the phase. For the ATe_2 materials, all these difficulties are present.

We have tried to circumvent the problem of multiple frequencies by analyzing the frequency with the largest amplitude in the FFT data. The validity of this approach is confirmed after the fact, when the slope in the Landau fan diagram equals the frequency of the band we used to construct the Landau fan diagram. For PTe_2 we chose the frequencies $\alpha_1 = 93.3$ T for the $B \parallel c$ and $\beta_4 = 225.6$ T in case of $B \parallel ab$. The slopes obtained from the fits of the Landau fan diagram are 94.7 and 228.2 T for the two directions. These values are very close to the frequencies for α_1 and β_4 and hence validates our approach above.

We have estimated the Berry phase ϕ_B close to π for both $PtTe_2$ and $PdTe_2$ when $B \parallel c$. We point out that the Landau index n for these two cases is 7 and 8, respectively, which is a reasonably small index. Therefore we believe that the extrapolation to estimate the intercept can be trusted. Measurements at lower temperatures and higher magnetic fields are desirable to reach even smaller Landau index so that the extrapolation to the quantum limit has an even smaller error. We note that for $PdTe_2$ there have been SdH measurements at T = 1.7 K for $B \parallel c$ with fields up to 35 T and a Landau fan diagram was constructed which reached n = 1 [44]. This study estimated a Berry phase of π from these measurements which is consistent with what we conclude from our data even though we start from a larger n. This gives us confidence that even for $PtTe_2$, our conclusion of $\phi_B \approx \pi$ could be valid although future experiments in higher fields can be used to confirm these results. Our results therefore suggest that $PtTe_2$ like $PdTe_2$, could also be a Type-II Dirac semi-metal.

we have also observed the planar Hall effect in single crystals of the nonmagnetic type-II Dirac semimetal $PtTe_2$. The PHE is observable up to room temperature suggesting the robustness of the relativistic carriers against the electron-phonon scattering. The Dirac/Weyl node in $PtTe_2$ is known to lie about 0.8 eV below the Fermi level. We note that recently PHE has also been reported in the iso-structural material $PdTe_2$ which is also a Type-II Weyl semi-metal. The Weyl node in $PdTe_2$ is also situated away from the Fermi energy. Thus our observation of PHE for a system like $PtTe_2$ therefore suggests that PHE can be used as a crucial transport diagnostic for topological character even for band structures with Dirac nodes slightly away from the Fermi energy. Here this is worth emphasizing that this effect is generally observed in magnetic thin films having anisotropic magnetization. However, here this effect is observed in a nonmagnetic semimetal with a Fermi level too high from Dirac node (0.8 eV). Currently the possible origin of planar

Hall effect in these nonmagnetic Dirac semimetals is not completely understood and further systematic experimental and theoretical efforts are required to pinpoint the correct origin of this effect.
In addition to this we would like to discuss Landau level fan diagram analysis of another quantum oscillation study on $A\text{Te}_2$ (A = Pt, Pd) in Ref. [136]. In this work also the authors have reported a low carrier effective masses and high mobilities for the two materials. Their Landau level fan diagram analysis however, is different. In order to obtain the contribution from an individual orbit out of the multi-frequency quantum oscillation data, they have used a low-pass filter of 50 T, to get the contribution from the lowest frequency orbit 8 T for $PdTe_2$, in the $B \parallel c$ direction. From the Landau level fan diagram obtained from this analysis, they conclude that the Berry phase for this orbit is different from π.

We point out that by applying a low-pass filter, one can not get a unique Landau level diagram as the location of the maxima and minima in the oscillation data obtained after applying the filter depend on the type of filter has been applied. In Fig. 4.14 we show the result of applying different low pass filters to the dHvA data for $PdTe_2$ for $B \parallel c$. It is clear that different filters give oscillations with slightly different locations of the maxima and minima, which are used to construct the Landau level fan diagram. This suggests that the Landau fan diagram and any numbers obtained from an analysis of the same will strongly depend on the filter applied.

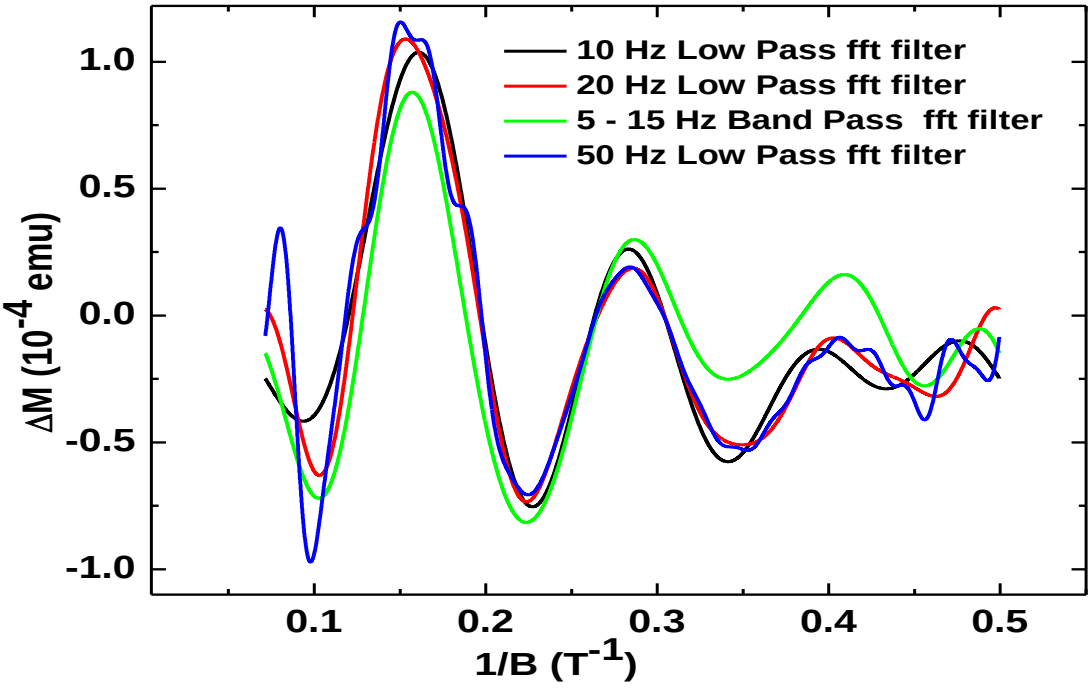

Figure 4.14: Oscillatory signal obtained after applying various low-pass filters to the dHvA data for $PdTe_2$ in the $B \parallel c$ direction. The oscillations clearly depend on what filter is applied.

CHAPTER 5

Fermi surface topology and large magnetoresistance in the topological semimetal candidate XBi (X = La, Pr)

5.1 Introduction

A topic of immense current interest is trying to combine topological character with strong electronic correlations. The rare-earth monopnictides RA (R = rare earth; A = Sb, Bi) are candidate materials for hosting correlated electrons with topological properties. All of these materials except YbBi, crystallize in a rock-salt type structure but exhibit different magnetic properties [137, 138]. Similar to the TSMs, rare earth based monopnictides have been found to exhibit XMR and very high mobility [139, 140, 141, 142, 143, 144]. But the topological character of the bands participating in the transport is still intensely debated, due to some contrasting reports. For instance, the electronic band structure of LaBi is regarded as topologically nontrivial, consisting of two Dirac cones at the X point, whereas other groups claim observation of only one Dirac cone at the X point in the ARPES experimental studies. Some other groups have shown that the bands near X point have a Dirac nodal line in character instead of Dirac cone [145, 146]. Other compounds in this series, such as LaAs, LaSb, PrSb, ScSb, YSb,TmSb, LuBi [139, 143, 147, 148, 149, 150, 151], show similar transport properties as LaBi, despite the fact that all of them are reported to be topologically trivial. Among Lanthanum based monopnictides LaBi has the largest spin-orbit coupling, which inverts the bulk band order to form multiple Dirac cones band structure,, making this system more interesting for further study. Further, it would be interesting to study the RX materials with a magnetic rare

earth since the 4 f-correlated electrons might influence the topological properties [152]. Most of the magnetic RX materials, however, show long ranged magnetic order at low temperatures [153], hindering a study of low-temperature magnetotransport properties. PrBi is special in this context since it has a partially filled 4 f shell but does not order at least down to 1.8 K [154]. A recent ARPES study on PrBi has revealed a nontrivial Z_2 band structure topology in the bulk characterized by an odd number of Dirac cones [152]. On the other hand, the isostructural materials PrSb and ScSb are found to be topologically trivial by band structure calculations, partly owing to the reduced spin-orbit coupling due to replacement of Bi by Sb in these materials. PrBi is thus a novel material in which the presence of f electrons, in addition to the possible topological band structure found in ARPES, raises the prospect of realizing a strongly correlated version of topological semimetals. In this chapter we present the detail low-temperature magnetotransport properties of single crystals of XBi (X = La, Pr).

5.2 Experimental Details

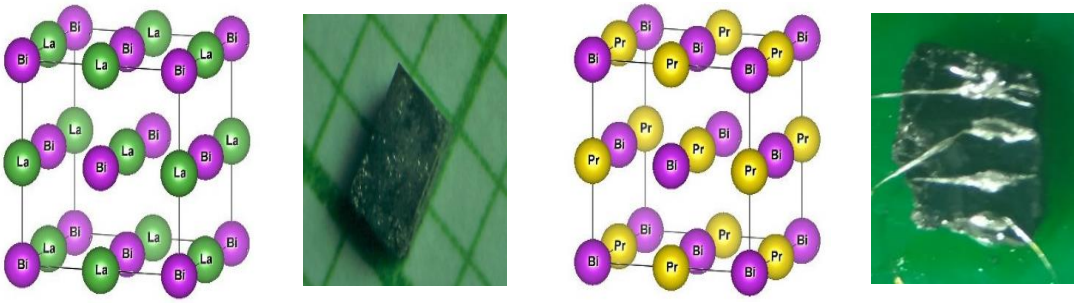

Figure 5.1: (a1) and (a2) shows the crystal structure of LaBi and PrBi. XBi (X La, Pr) crystallize in simple rock salt type face centered cubic structure. (b1) and (b2) Single crystal images of LaBi and PrBi respectively.

High quality single crystals of XBi (X = La, Pr) were grown by using the Indium flux. The details of amount of flux and temperature profile has been provided in chapter 2. The resulting single crystals of XBi (X = La, Pr) are shown in Fig. 5.1 (b1) and (b2) respectively. The typical size for LaBi crystal was 2 $\times$ 1 $\times$ 1 mm and for PrBi crystal it was 3.5 $\times$ 2 $\times$ 1 mm. The chemical composition and uniformity of stoichiometry for crystals of XBi (X = La, Pr) were confirmed by EDX taken at various spots on cystals. Single crystal X-ray diffraction on these crystals confirmed the rock salt type structure with Fm3m (225) space group (Fig. 5.1 (a1) and (a2)). The x-ray diffraction pattern did not show presence of any impurity phases. The Lattice parameters of XBi (X = La,

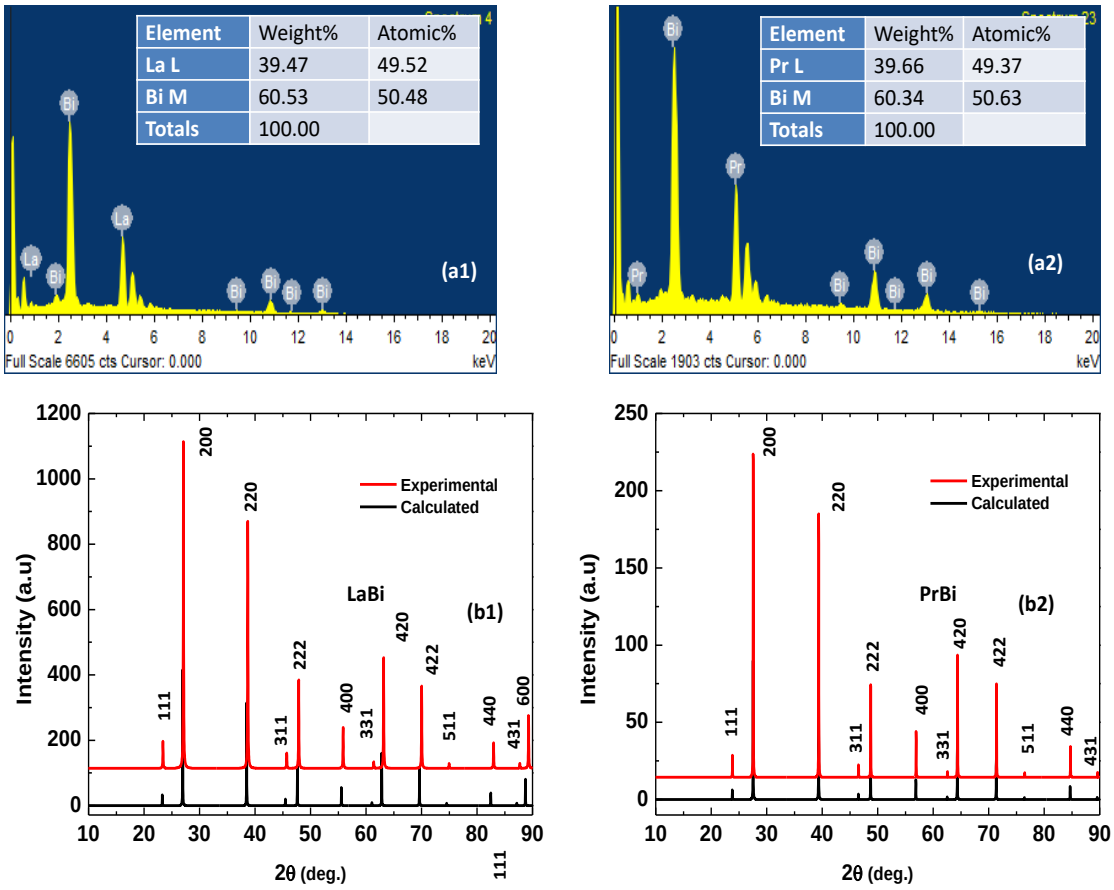

Figure 5.2: Results of chemical analysis (a1) and (a2) and PXRD pattern simulated from SC XRD data using Mercury software (b1) and (b2) on LaBi and PrBi, respectively.

Table 5.1: Lattice constants of XBi (X = La, Pr)

Compound	a(Å)	b(Å)	c(Å)	V(Å^{-3})
LaBi	6.577	6.577	6.577	284.5
PrBi	6.47	6.47	6.47	270.84

Pr) deduced from single crystal XRD are listed in table 5.1. The lattice constants of PrBi is smaller than LaBi which is expected due to Lanthanide contraction. The results of chemical analysis and powder x-ray diffraction for XBi (X = La, Pr) are shown in Fig. 5.2.

5.3 Results and Discussion

5.3.1 LaBi

Fig. 5.3 (a) shows temperature dependent resistivity ρ(T) data of LaBi single crystals, which in zero field exhibit a typical metallic character down to 2 K. A large residual re-

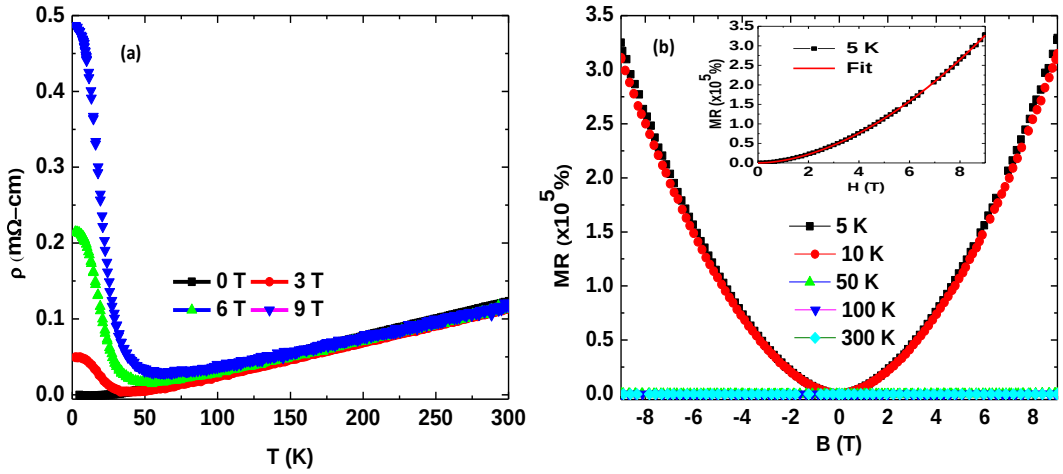

Figure 5.3: (a) Temperature dependence of resistivity at various magnetic fields. (b) Transverse magnetoresistance at various temperatures. Inset show the power law behavior of MR at 5 K.

sistivity ratio RRR [ρ(300K)/ ρ(2K)] = 665, indicates the high quality of the measured single crystal. At zero applied magnetic field these crystals display a saturation in ρ(T) at low temperature regime. However, on application of a perpendicular magnetic field, resistivity shows an unusual upturn before saturating at lower temperatures. This effect has been generally attributed to the field induced metal to insulator transition (MIT) due to an opening of a gap at the Dirac point by applied magnetic field [155, 156]. However, there can be other mechanisms which can be possible in a highly mobile electronic system. For instance, there are theoretical arguments that this field induced MIT may originate from the exitonic gap formation in an applied magnetic field [157]. The true nature of this MIT is still under debate and future experiments and theoretical efforts can shed light on the correct physical mechanism. Our experimental observations shown in the Fig. 5.3 (a) clearly indicates that this is a field induced MIT, as the resistivity in a field of 9 T surpasses the room temperature value of resistivity. Transverse MR measured at different temperatures (5 K-300 K) is shown in the Fig. 5.3 (b). The nature of the weak field MR at low temperatures can be fitted with the simple Kohler's equation $\rho(B) \sim aB^n$, where B is magnetic field and n is an exponent. A value of n = 1.8 is extracted from the fit, which is near to the quadratic field dependence of the MR, indicating a three dimensional charge carrier transport in LaBi. MR at low temperatures shows a non-saturating linear character which reaches to an extremely large value of 3.25×10^5 % at 2 K. This value of MR is nearly one order of magnitude higher than the values reported previously for LaBi [158, 159].

Fig. 5.4, shows the raw magnetization (M) versus magnetic field (B) data in the $B \parallel c$ at T = 2 K. Pronounced dHvA oscillations can be observed which starts from field as

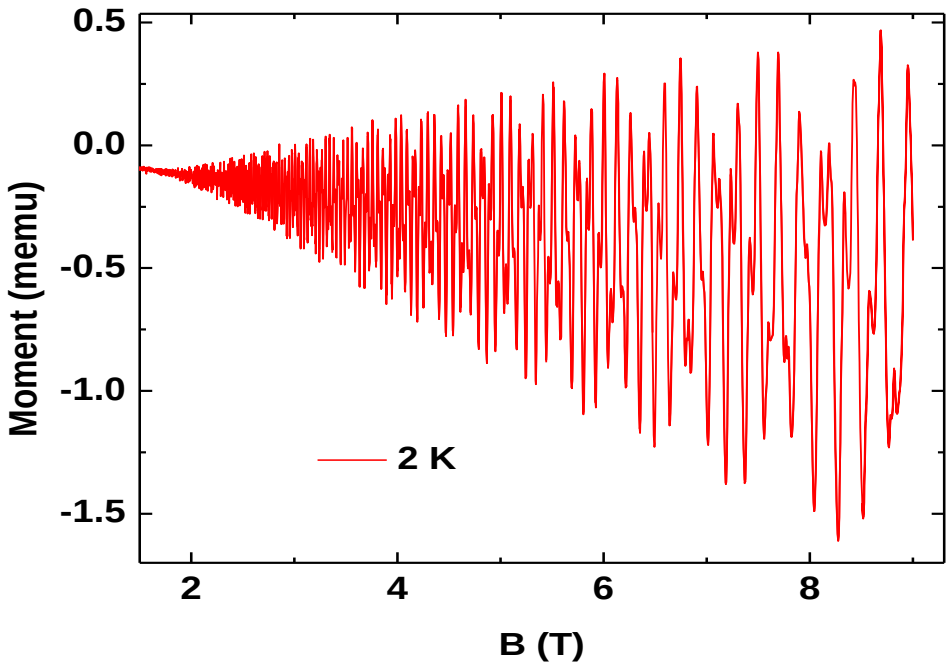

Figure 5.4: Raw magnetization data for LaBi at temperature 2 K. Beautiful dHvA oscillation are observed starting from magnetic field close to 2 T

low as 2 T. From the Fig. 5.5 (a) clear large amplitude dHvA oscillations after a linear background subtraction which survive up to a temperature of 20 K can be seen. This is suggestive of the highly mobile charge carriers in these crystals. In order to analyze the Fermi surface properties of LaBi, we obtain a fast Fourier transform (FFT) spectrum of these quantum oscillations, which is shown in Fig. 5.5 (b). From the FFT, we can clearly identify the presence of two oscillation frequencies F(α) = 273 T and F(β) = 603 T. The presence of these two frequencies indicates the presence of the two Fermi surface pockets in the band structure of LaBi. The Fermi surface area of both Fermi pockets has been calculated by the Onsager relation for frequency $F = A_F(\varphi/2\pi^2)$, where $\varphi = h/e$, is the flux quantum and other quantities have usual meaning unless specified. The calculated Fermi surface area for both frequencies is listed in table 5.2.

The temperature and field dependence of the oscillations in the magnetization data is given by the L-K formula,

$$\Delta M \propto -R_T R_D \sin(2\pi[\frac{F}{B} - (\frac{1}{2} - \phi)]) \tag{5.1}$$

where, $R_D = exp(-\lambda T_D)$ is the Dingle factor, $T_D = \hbar/2\pi K_B \tau$ is the Dingle temperature, and the temperature dependent damping of the oscillations is accounted for by the factor $R_T = \lambda T/\sinh(\lambda T)$, with $\lambda = (2\pi^2 K_B m^*/\hbar e B)$ and m^* the effective cyclotron mass. The two damping factors R_T and R_D are used to calculate important band parame-

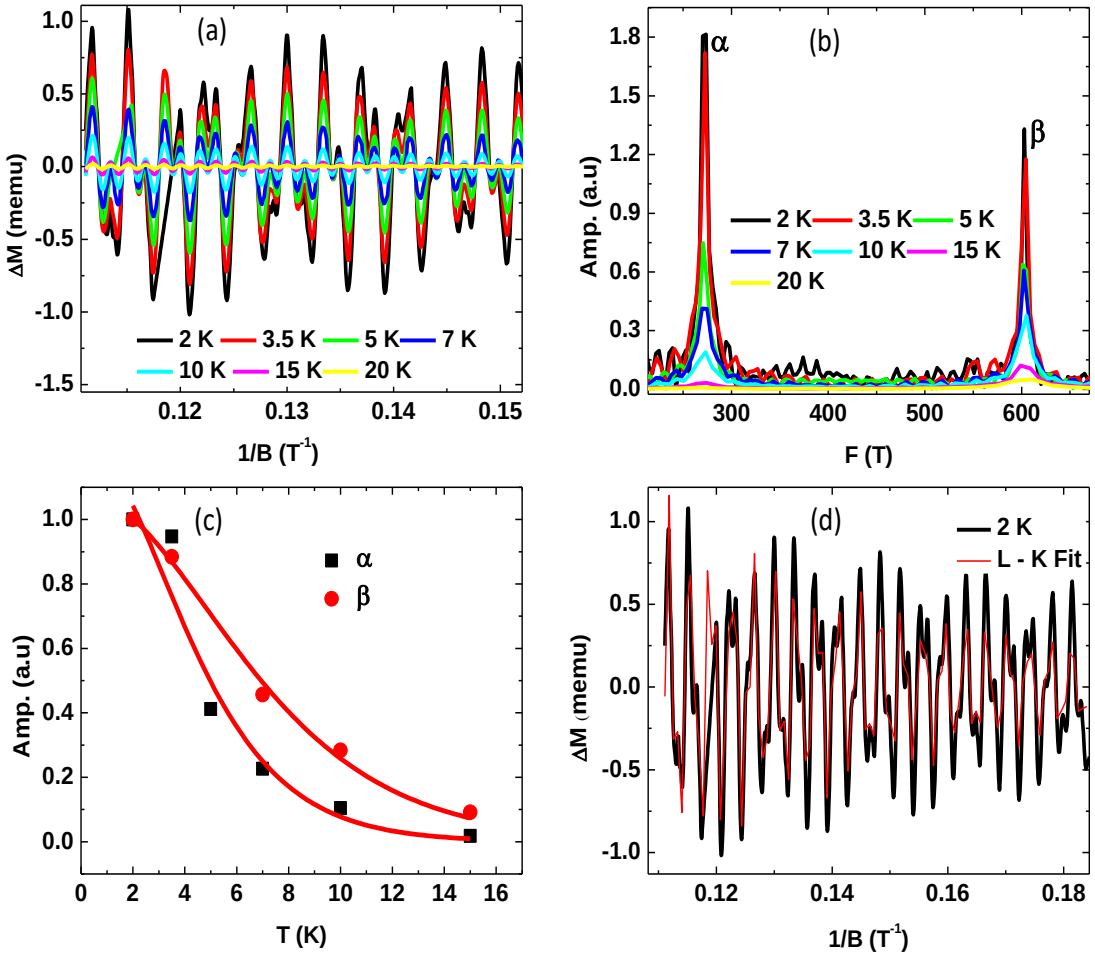

Figure 5.5: (a) dHvA oscillations at various temperature after background subtraction. (b) FFT spectra at various temperatures. (c) Temperature dependence of FFT amplitude, fitted with L-K formula. (d) The L-K fit to the dHvA data at 2 K.

ter such as effective mass m^* and quantum mobility μ of the charge carriers, respectively. The effective mass has been calculated from fitting T dependence of FFT amplitude as shown in figure Fig. 5.5. The effective mass and the quantum mobility thus calculated for the two frequencies are also listed in table 5.2 and table 5.3. A low values of effective mass ($0.19m_0$ and $0.12m_0$) along with high values of the quantum mobility (2450 $cm^2/V-s$ and 1772 $cm^2/V-s$) suggest the presence of relativistic charge carriers in LaBi. It should be noted from the large difference in the values of the mobility for the two Fermi pockets that the pocket alpha is Dirac type. We confirm this claim by fitting the quantum oscillation data by the full L-K formula, given by equation 5.1. Fig. 5.5 (d) shows the experimental magnetization data fitted with the two–band L-K formula. The Berry phase (ϕ_B) has been calculated using a relation $\phi = \phi_B/2\pi - \delta$. Here, δ is an additional phase shift which depends on the dimensionality of the Fermi surface and takes the value 0 or $\pm 1/8$ ($-$ for electron like and $+$ for the hole like) for two and three dimension,

Table 5.2: Fermi surface parameters for LaBi obtained from the dHvA data shown in Fig. 5.5

.

F (T)	A_F(Å^{-2})(10^{-2})	K_F(Å^{-1})(10^{-2})	m^*/m	$v_F(m/s)(10^5)$	ϕ_B
273	2.6	9.1	0.19 ± 0.017	5.5	(- 0.77 ± 0.003)π
603	5.7	13.56	0.12 ± 0.017	13	(- 0.09 ± 0.005)π

Table 5.3: Parameters obtained from Dingle temperature

.

$T_D(K)$	$\tau(10^{-13}s)$	l (nm)	$\mu(cm^2/V-s)$
4.57 ± 0.10	2.65	145.7	2450
10 ± 0.17	1.21	157.3	1772

respectively. In our Berry phase calculations we have taken $\delta = -1/8$ for α pocket and $\delta = +1/8$ for β pocket [160]. The value of Berry phase for α (electron pocket) and β (hole pocket) Fermi pocket are (-0.77 ± 0.003)π and (-0.09 ± 0.005)π, respectively. Clearly, the Berry phase for the α pocket is closer to a value of π, which corresponds to the Dirac bands. On the other hand, for the other pocket β we find a Berry phase ≈ 0 which is consistent with a topologically trivial band.

5.3.2 PrBi

Experimental results

In order to compare the Dirac nature of the bands in PrBi, a rare earth monopnictide consisting of partially filled f -electron shells with those in LaBi, we have performed similar magneto-transport measurements and analysis on PrBi single crystals. The temperature-dependent resistivity ($\rho(T)$) at various field of the PrBi single crystals with the magnetic field parallel (B $\parallel$ I) and perpendicular (B $\perp$ I) to the current I are shown in Fig. 5.6. A large value of the zero field residual resistivity ratio, ρ(300 K)/ ρ(2 K) = 374, indicates the high quality of the single crystals used in this study. The zero-field resistivity follows a linear T dependence from 300 K to 100 K, as can be seen in Fig. 5.6, (a1). Below T = 100 K, the resistivity falls rapidly and nearly saturates in the low temperature regime T = 10 K.

The application of magnetic fields drives a metal to insulator like transition (MIT) at low temperatures for both perpendicular (B $\perp$ I) and in-plane magnetic field (B $\parallel$ I) orientations, as can be seen from Fig. 5.6 (a1) and (b1). This MIT-like feature in $\rho(T)$ is more prominent in the B $\perp$ I configuration and exceeds the room temperature value of resistivity in the low-T regime at a field of 9 T [see Fig. 5.6 (a1)]. The $\rho(T)$ in magnetic field goes through a minimum at a temperature ($T_m \approxeq 15$ K), shows a sharp upturn below T_m, before eventually saturating at lower temperatures. This low-temperature behavior of

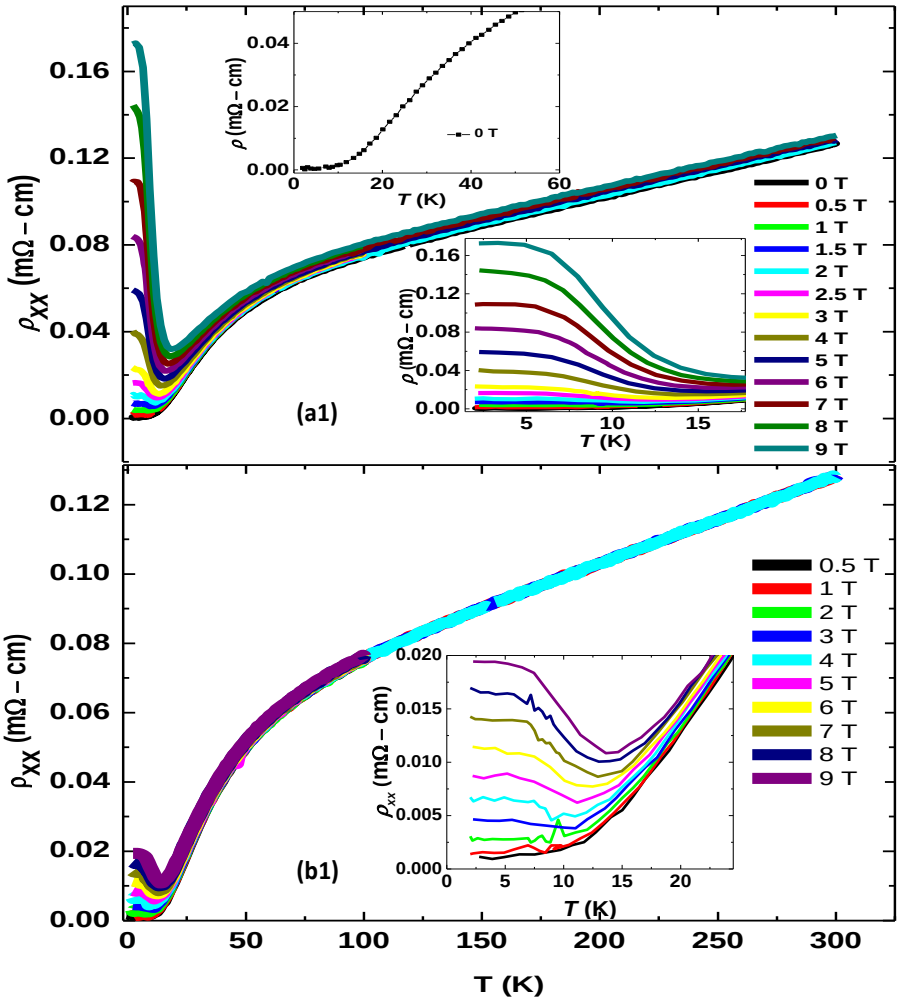

Figure 5.6: (a1), (b1) Temperature dependence of ρ_{xx} in the two configurations B $\perp$ I and B $\parallel$ I, at various magnetic fields. Upper inset of (a1) shows the zero-field behavior of ρ_{xx} at low temperature. Lower insets of (a1) and (b1) show enlarged view of ρ_{xx} at low temperature, at various fields.

$\rho(T)$ in fields is highlighted in the lower insets of Fig. 5.6 (a1) and (b1). The minimum in ρ(T, H) can also be seen in the d$\rho(T)$/dT vs T plot shown in the inset of Fig. 5.6 (b2). Similar field-driven MIT features have been observed in the topological semimetals WTe_2, NbP, and TaAs [56, 161, 162].

Since the $\rho(T)$ appears to have a larger response for B $\perp$ I, we show the MR for the B $\perp$ I configuration at various temperatures in Fig. 5.7 (a2). The MR for B $\parallel$ I is qualitatively similar but smaller in magnitude. The MR for temperatures above T_m is quite small. For lower temperatures, the MR increases dramatically. The MR at 2 K in a field of 9 T reaches a very large value of $\sim 4.2 \times 10^4\%$, which is comparable to values observed in other monopnictide compounds [140, 143, 144]. The MR has a nearly

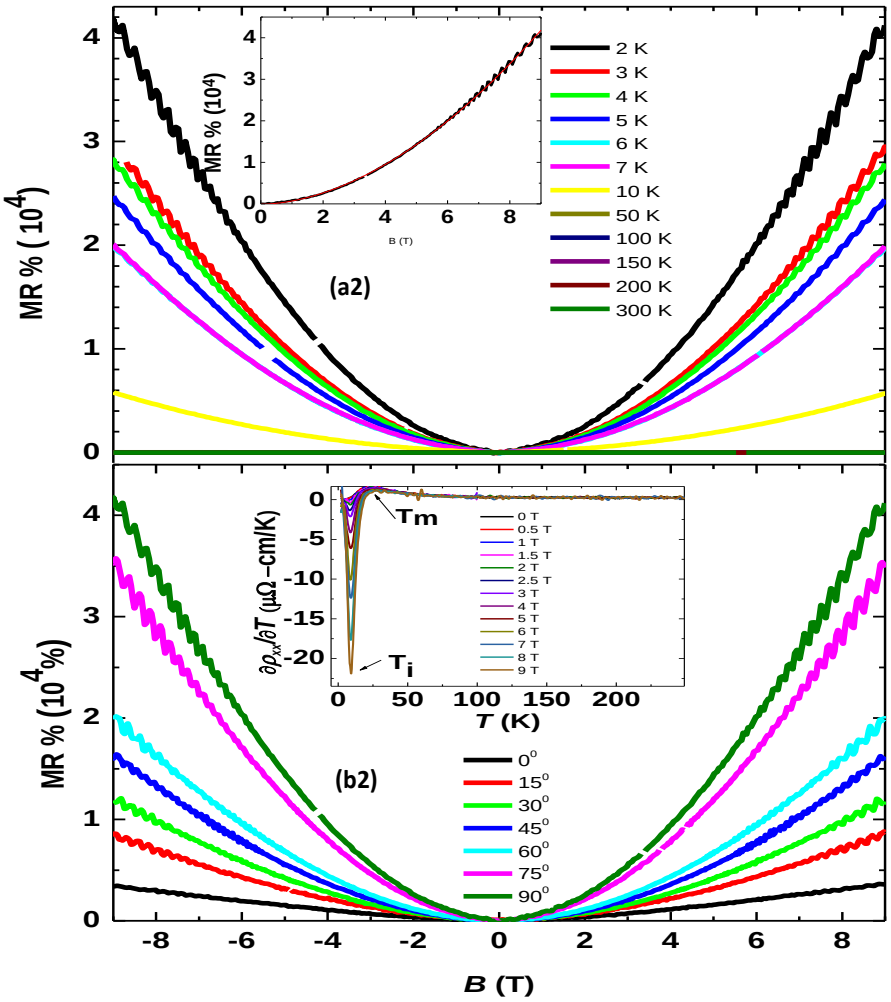

Figure 5.7: (a2) Magnetic field dependence of ρ_{xx} in the direction $B \perp I$ at various temperatures. Inset shows the power-law behavior of MR. (b2) Magnetic field dependence of ρ_{xx} at 2 K by varying the (out of plane) angle between B and I. Inset shows dρ_{xx}/dT vs temperature at various fields.

parabolic B dependence and is nonsaturating up to 9 T. We successfully fit the MR with a power-law dependence, $\propto B^m$ [inset of Fig. 5.7 (a2)], with an exponent m = 1.82. This nearly quadratic behavior is a characteristic feature of three-dimensional charge transport in multiband metals. Below 5 K, SdH quantum oscillations riding on top of the smooth quadratic MR can be clearly observed at higher fields, and these oscillations become stronger with decreasing temperature, as can be seen in Fig. 5.7 (a2).

The angular dependence of the MR at T = 2 K is presented in Fig. 5.7 (b2), as the out of plane angle between the magnetic field B and the current I is varied starting from B||I, for which the angle is 0°. It can be seen that the MR for B||I is an order of magnitude smaller than for B $\perp$ I. The MR for all angles shows a quadratic B dependence. Additionally,

quantum oscillations can be seen in the MR data at all angles.

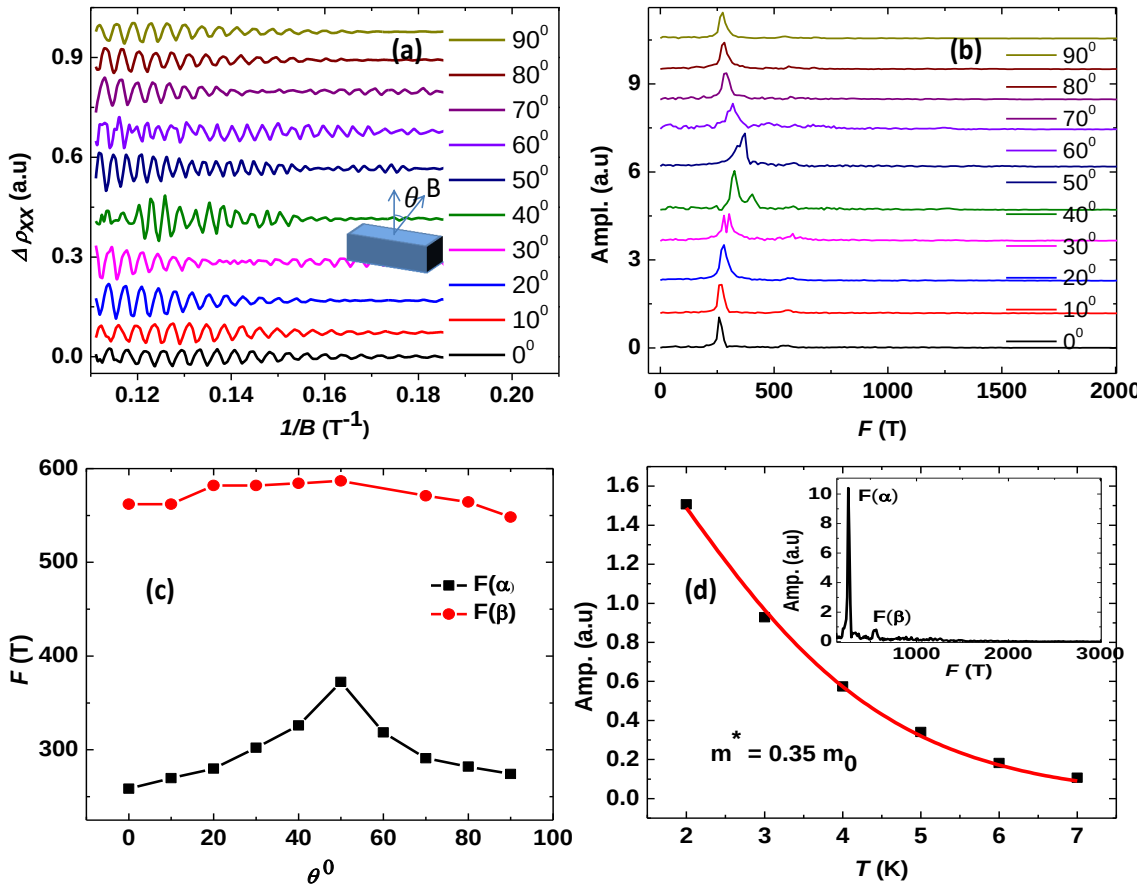

Figure 5.8: (a) Background subtracted SdH oscillations at various angles, at 2 K. (b) The FFT spectra at different angles. (c) The angular dependence of the frequencies $F(\alpha)$ and $F(\beta)$. (d) Fitting of the temperature-dependent amplitude in the FFT spectra by the L-K formula.

We next study the Fermi surface topography of PrBi by measuring the angle dependence of the quantum oscillations in the MR data, taken at 2 K. In order to extract clear oscillations, a polynomial background has been subtracted from the MR at each angle. The resulting periodic oscillations at several angles are plotted against the inverse of the magnetic field Fig. 5.8 (a). It is clear from these data that the oscillations do not vanish and remain pronounced as we rotate the magnetic field from the B $\perp$ I to the B $\parallel$ I configuration. This suggests that the charge carriers in PrBi are of three dimensional character. A fast Fourier transform (FFT) of the quantum oscillation data in Fig. 5.8 (a) for each angle was done and is shown in Fig. 5.8 (b). The FFTs shown in Fig. 5.8 (b) for different angles are shifted by arbitrary amounts for clarity. From the FFT of the data we find two fundamental frequencies, which for B $\perp$ I are $F(\alpha) = 258.49$ and $F(\beta) = 561.94$ [inset Fig. 5.8 (d)].

From Fig. 5.8 (b) the angular evolution of the two frequencies $F(\alpha)$ and $F(\beta)$ can

be seen. With increasing angle we observe a gradual shifting of the α frequency towards higher values. In addition, a new frequency emerges as the tilt angle reaches $\theta = 30^{\circ}$. This frequency vanishes or merges into another frequency as we approach $\theta = 50^{\circ}$. This type of frequency shifting/splitting has been observed in other monopnictides such as TmSb and CeSb, suggesting a similar Fermi surface [163, 164, 165]. This angular variation has been proposed to result from the quasi two dimensional character of the Fermi surface in the case of LaBi [160]. However, the observed variation in frequency can also result from an likely the case here due to the α electron pockets at the X point in the Brillouin zone. We have plotted the values of the two main frequencies as a function of the angle in Fig. 5.8 (c). From the angular variation, it can be seen that the frequency $F(\alpha)$ shows a monotonic increase in value up to an angle $\theta = 50^{\circ}$, and decreases thereafter reaching close to its $\theta = 0^{\circ}$ value at $\theta = 90^{\circ}$. This behavior is consistent with an anisotropic elliptical Fermi surface orbit for the α band. The other frequency $F(\beta)$ remains almost unchanged for the entire variation in the tilt angle. This frequency corresponds to the hole pockets centered at the γ point in the first Brillouin zone. We thus conclude that the quantum oscillations observed in the PrBi single crystals primarily originate from the three dimensional bands instead of the two dimensional ones. In addition to this, we have measured the MR in the longitudinal magnetic field configuration B $\parallel$ I to look for any signature of the chiral anomaly induced negative MR. We did not detect any negative MR. We have also carried out temperature and magnetic field dependent magnetization measurements on the same PrBi crystal.

The temperature dependence of the magnetization measurement reveals the paramagnetic nature of PrBi [see Fig. 5.9 (a)]. The plateau below 10 K is consistent with previous reports [143, 166] and most likely arises from Van Vleck temperature independent paramagnetism. We did not observe any signature of long-range ordering down to 2 K, and by fitting the data above 160 K to a Curie Weiss law [inset of Fig. 5.9 (a)] we estimated an effective magnetic moment $\mu_{eff} = 3.42\ \mu_B$. This value is close to the previous report [153] and suggest the trivalent nature of Pr atom. The high quality of our PrBi single crystals allowed us to observe pronounced quantum oscillations (dHvA) in magnetization measurements as well and are shown in Fig. 5.9 (b). The FFT of these oscillations reveals three fundamental frequencies. The frequencies $F(\alpha)$ = 264.4 T and $F(\beta)$ = 571.2 T are close to the frequencies found from the SdH oscillation data presented above. An additional frequency [apart from F(2β) = 1131.8 T, the second harmonic of the β band], F(γ) = 1517.9 T, is also observed in the T = 2 K data and has a very small amplitude, which is most likely the reason it was not observed in the SdH oscillations. For this reason we are unable to track the temperature dependence of the frequency of the γ band.

We next calculate the transport parameters corresponding to the two main frequencies

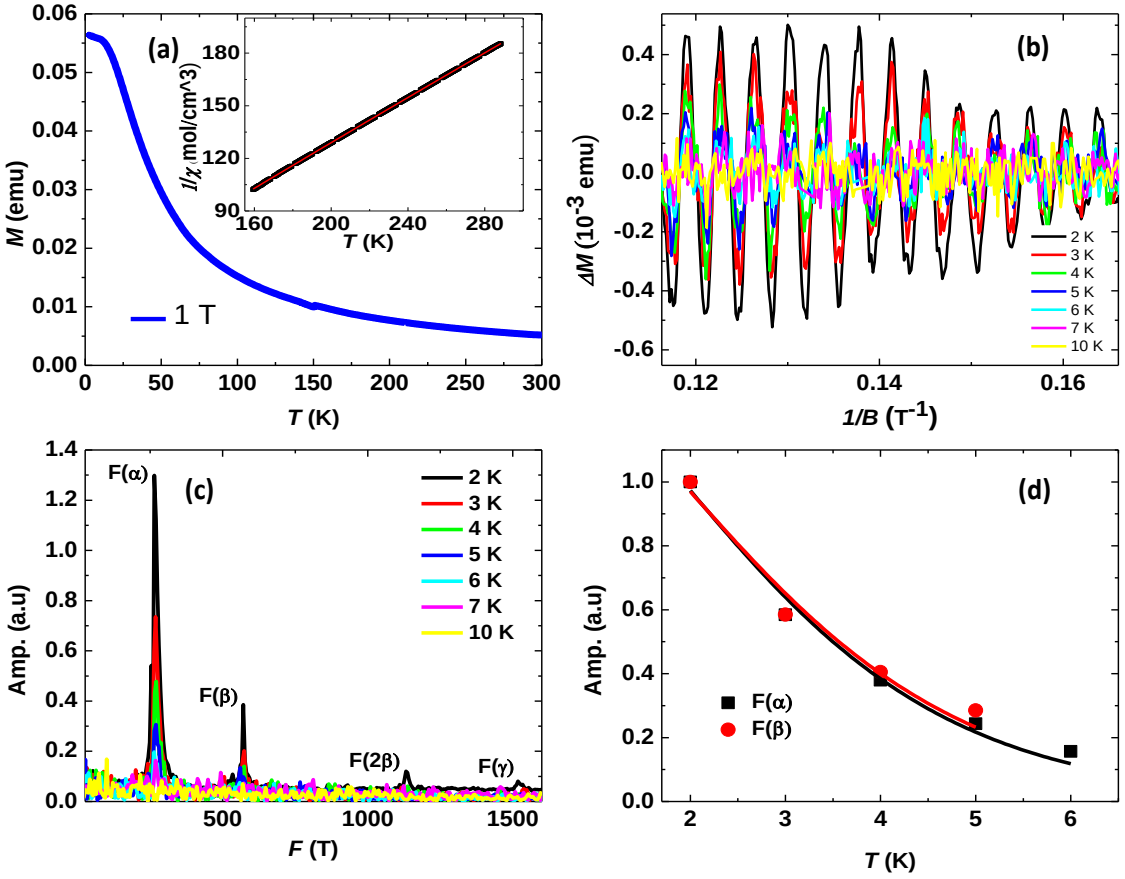

Figure 5.9: (a) Temperature dependence of the magnetic moment of PrBi in an applied field of 1 T. (b) The temperature-dependent dHvA oscillations obtained after background subtraction. (c) Temperature dependence of the FFT spectra. (d) Fitting of temperature-dependent FFT spectra using L-K formula

$F(\alpha)$ and $F(\beta)$ found in the SdH and dHvA oscillations. The area of the extremal orbits corresponding to these two frequencies can be calculated using the Onsager relation, $F = A_F(\varphi/2\pi^2)$, where $\varphi = h/e$, is flux quantum, A_F is Fermi surface area, h is plank constant and e is the charge of the electron. By assuming a circular cross section of the cyclotron orbits at the Fermi level, we have calculated the values of the Fermi momentum k_f and Fermi energy E_f. The calculated area of the Fermi surface for the two frequencies extracted from SdH and dHvA oscillations is given in table 5.4. The area/carrier concentration corresponding to the hole orbit (β pockets) is much larger than the electron orbit (α pockets), which implies the dominance of hole carriers in the low-temperature regime. This is further confirmed by the Hall data, which we present later. The amplitude of the quantum oscillations in resistivity and magnetization can be described by the equations

$$\Delta\rho \propto -R_T R_D \cos(2\pi[\frac{F}{B} - (\frac{1}{2} + \beta + \delta)]) \tag{5.2}$$

$$\Delta M \propto -R_T R_D \sin(2\pi[\frac{F}{B} - (\frac{1}{2} + \beta + \delta)]) \tag{5.3}$$

where different symbols have their usual meaning as explained in the results section of LaBi. The fitting of the SdH oscillations yields effective mass for the α pocket $m^* = 0.35m_0$, where m_0 is the rest mass of electron. Almost similar value of the effective mass $m^* = 0.32m_0$, for the α pocket is obtained by fitting the dHvA oscillation amplitudes. In addition, the effective mass for the β pocket is found to be $0.31m_0$, which is comparable to the effective mass corresponding to the α pocket. These values of the effective mass for the two pockets are much higher (massive) than those observed in typical Dirac semimetals [161, 167] and are comparable to values found for other monopnictides in this series [140, 143]. Our results suggest that it is unlikely that the conduction in PrBi is primarily from the Dirac bands. This would be consistent with ARPES studies that find the Dirac node to be located much below ($\approx$ 0.35 eV) the Fermi level [152].

By fitting field-dependent damping of the oscillation amplitude (α pocket) with $R_D = exp(-\lambda T_D)$, we calculate a Dingle temperature of T_D = 2.62 K. The corresponding quantum lifetime is calculated to be $\tau = 4.6 \times 10^{-13}$s, and calculated quantum mobility is $\mu = 2310\ cm^2/$Vs. A high value of carrier mobility has been suggested to be a signature of the Dirac carriers in LaBi and related compounds, but our data on PrBi show that a high mobility can also be possible from three-dimensional bands. Other parameters obtained from a Dingle fitting of the quantum oscillation data are given in table 5.5.

In order to probe the possible topological nature of the bands in PrBi, we have constructed the Landau fan diagram from the quantum oscillation data as shown in Fig. 5.10 (a). To construct the Landau fan diagram, we assign an integer value to the minima in the oscillation data of σ_{xx}. The extrapolated value of the intercept n = 0.54(2) is close to the theoretical value (0.5) expected for a topologically nontrivial system.However, it is worth mentioning that there will most likely be a large uncertainty in determining the intercept on the n axis due to the large value of the Landau index (30) that we have to extrapolate from. To get an alternate estimate of the Berry phase, we have performed a multifrequency Lifshitz Kosevich (L-K) fit of the 2 K dHvA data shown in Fig. 5.10 (c). To reduce the number of free parameters in equation 5.3, the values of effective masses were fixed to the values estimated above and shown in table 5.4. The L-K fit is shown in the Fig. 5.10 (c). From the fit we estimate a Berry phase for the α Fermi pocket to be $(0.95 \pm 0.01)\pi$. This is consistent with the Landau faN diagram analysis described above and strongly indicates the Dirac nature of fermions. Fig. 5.10 (d) shows the Hall resistivity at various temperatures. At higher temperatures, the slope of the Hall resistivity is negative and almost linear, indicating that the dominant carriers are electrons at high temperature. As the temperature is decreased below 10 K, the slope of the Hall resistivity

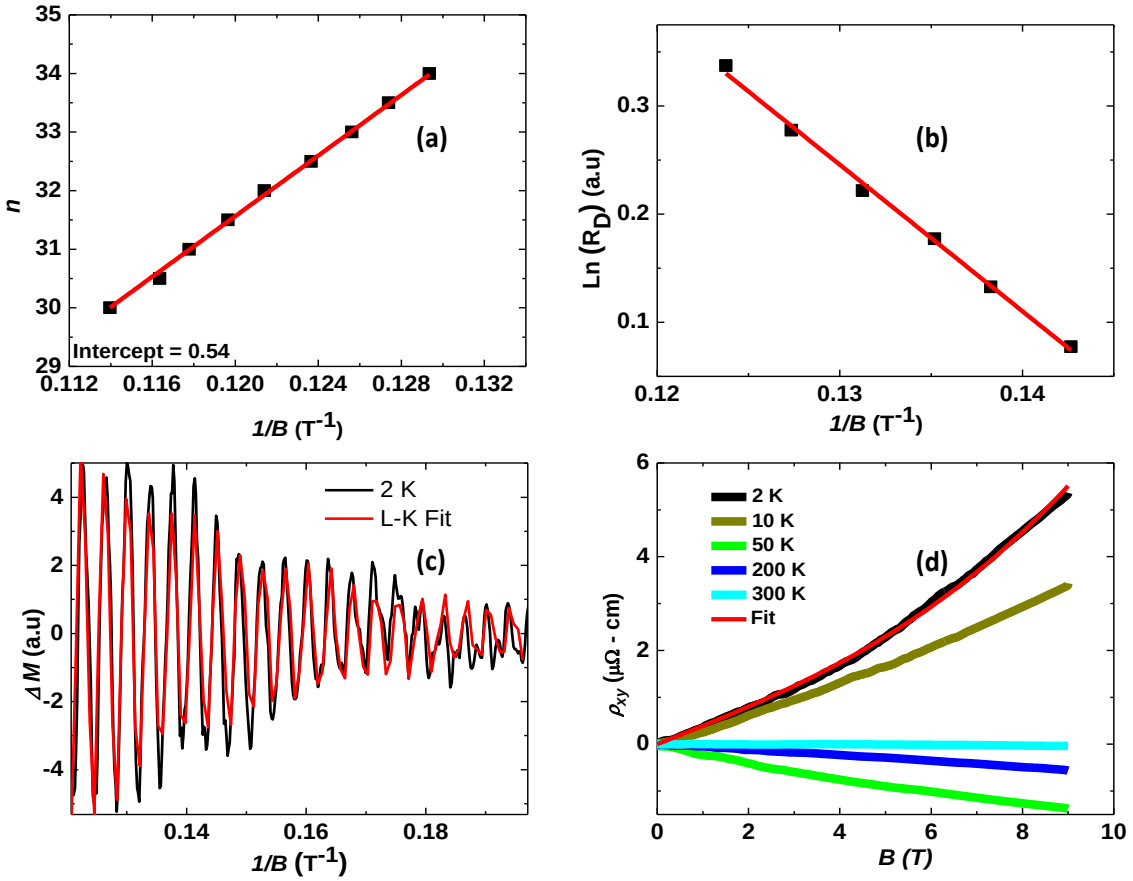

Figure 5.10: (a)Landau fan diagram extracted from the quantum oscillation data showing the Landau band index n vs reciprocal of the field 1/B. The extrapolated intercept is close to what is expected (0.5) for a topologically nontrivial system. (b) Dingle fitting at 2 K. (c) The L-K fit to the dHvA data at 2 K. (d) The Hall resistivity vs field at various temperatures. The solid curve through the data at T = 2 K is a fit by a two band model

changes to a positive value with a weak nonlinearity at the higher fields. The nonlinearity becomes more pronounced at T = 2 K, as shown in Fig. 5.10 (d). The change in the sign of the Hall resistivity indicates that there is a change in the dominant carrier type from electron to holes with decreasing temperature. The nonlinear nature of the Hall resistivity also indicates that PrBi has contributions from two kinds of carriers. For a quantitative analysis, the Hall resistivity data at T = 2 K were fitted by using a two-band model [168],

$$\rho_{yx} = \frac{B}{e}\frac{(n_h\mu_h^2 - n_e\mu_e^2) + (n_h - n_e)(\mu_h\mu_e)^2B^2}{(n_h\mu_h + n_e\mu_e)^2 + (n_h - n_e)^2(\mu_h\mu_e)^2B^2} \tag{5.4}$$

Here n_h, μ_h and n_e, μ_e are carrier density and mobility of holes and electrons respectively. The fit, shown as the solid curve through the T = 2 K data in Fig. 5.10 (d), indicates that the electron and hole carrier density are approximately the same, $\approx \sim 0.45 \times 10^{19} cm^{-}3$, indicating the nearly compensated semimetal nature of PrBi. The obtained

Table 5.4: Fermi surface parameters for PrBi obtained from the SdH and dHvA data shown in Fig. 5.8 and 5.9

	F (T)	$A_F(\text{Å}^{-2})(10^{-2})$	$K_F(\text{Å}^{-1})(10^{-2})$	m^*/m	$v_F(m/s)(10^5)$	$E_F(meV)$	$n(cm^{-3})(10^{19})$
SdH	258.49	2.474	8.876	0.35 ± 0.007	2.93 ± 0.06	170.21 ± 10	2.36
	561.94	5.378	13.08	–	–	–	7.56
dHvA	264.40	2.530	8.980	0.32 ± 0.018	3.24 ± 0.18	190.70 ± 32	2.40
	571.19	5.466	13.20	0.31 ± 0.027	4.90 ± 0.42	423.9 ± 109	7.70
	1517.9	14.52	21.50	–	–	–	33.6

Table 5.5: Parameters obtained from a Dingle fitting of the SdH data shown in Fig. 5.10 (b).

$T_D(K)$	$\tau(10^{-13}s)$	l (nm)	$\mu(cm^2/V-s)$
2.62 ± 0.1	4.6 ± 0.2	133 ± 8	2310 ± 148

mobilities of charge carriers are $3 \times 10^3 cm^2/V-s$.

Computational details

We use density functional theory (DFT) to calculate the band structure and Fermi surface of PrBi. The density functional theory calculations in the generalized gradient approximation (GGA) framework were carried out using plane-wave and pseudopotential methods as implemented in the Quantum Espresso package [169, 170]. A kinetic energy cutoff of 65 Ry was used for the plane-wave expansion of valence wave functions. Electronic structure was determined with and without spin-orbit coupling. The Perdew-Burke-Ernzerhof (PBE) [171] exchange-correlation functional was used with fully relativistic and scalar-relativistic ultrasoft pseudopotentials for spin-orbit interaction (SOI) and nonspin- orbit interaction (non-SOI), respectively. For the selfconsistent calculations a $24 \times 24 \times 24$ k-point mesh was used to sample the reduced Brillouin zone (BZ). A finer k-point mesh of $50 \times 50 \times 50$ was used to generate the Fermi surface (FS). The FS was visualized using the XCRYSDEN software [172]. The maximally localized Wannier function method [173] was employed to calculate the dHvA frequencies using the SKEAF code [174].

Theoretical results

In Table 5.6, we compare the calculated lattice parameters of PrBi with experiments. We performed structural optimization (atoms positions and cell parameters were allowed to vary) to calculate cell parameters for the non-SOI case. For the calculations with SOI included, the lattice parameter a was obtained by performing energy calculations at various constant a values and these data were fit by the Birch-Murnaghan equation of state.

As can be seen from Table 5.6, the GGA gives the unit-cell volume and lattice parameter to within about 1% of the experimental parameters for both non-SOI and SOI calculations.

Table 5.6: Calculated lattice parameters and unit cell volume compared with experimental values.

Cell parameters	Non-SOI	SOI	expt
$a = b = c$ (Å)	6.53	6.54	6.47
volume (Å^3)	278.45	279.73	270.84

Electronic band structure

The electronic structure and partial density of states of PrBi without and with spin-orbit coupling are shown in Fig. 5.11, panels (a) and (b) and panels (c) and (d), respectively. Fig. 5.11 illustrates the semi-metallic behavior of PrBi with a small density of states at the Fermi level. For both non spin-orbit and spin-orbit calculations we find that, close to the Γ and X high-symmetry points of the Brillouin zone, energy bands cross the Fermi level (E_F), creating hole pockets at the Γ point and electron pockets at the X points. For the non-spin-orbit case, four bands cross E_F, with three hole-like bands at Γ point and one electron-like band at X point as can be seen in Fig. 5.11. The inclusion of spin-orbit coupling splits the bands and now there are three doubly-degenerate bands crossing the E_F. Out of these three bands, two are hole-like near Γ and one is electron-like near X as can be seen in Fig. 5.11 (c).

As can be seen from Fig. 5.11 (b), for non-SOI calculations, near the Fermi level the valence band is primarily a mixture of Bi p-orbitals. On the other hand, the conduction band mainly consists of Pr d-orbitals with small contribution of Bi p-orbitals. The strong spin-orbit interaction splits degenerate Bi p-orbitals into $p_{3/2}$ and $p_{1/2}$ orbitals with a splitting of ≈ 1.9 eV. The $p_{1/2}$ orbital goes into the valence band around -1.2 eV and the $p_{3/2}$ orbitals contribute near the Fermi level and the valence band. The Pr d-orbitals split into e_g and t_{2g}, and SOI further splits t_{2g} into doubly degenerate and non-degenerate orbitals.

The band-structure between Γ and X has some important features. For the non SOI case shown in Fig. 5.11 (a) Bi(p) and Pr(d) orbitals cross close to the X point between Γ and X. With SOI, there is a band inversion below E_F along Γ-X creating a hole pocket and a gap of 0.7 eV opens up at the X point. The direct band gap at Γ point reduces from 0.26 eV for non-SOI to 0.15 eV for SOI. The overlap between the valence band at Γ and conduction band at X is 0.65 eV for PrBi with SOI.The electronic band structure of PrBi with and without spin-orbit interactions are consistent with a recent report using VASP implementation of DFT [152].

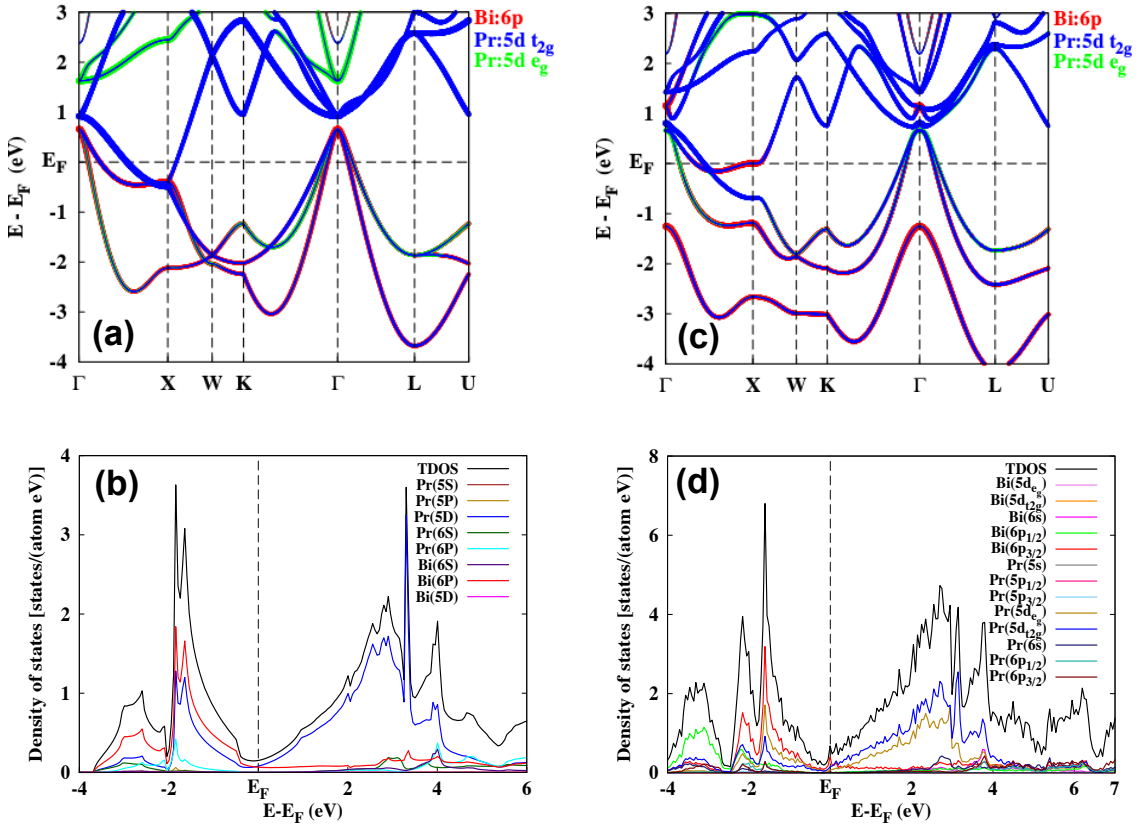

Figure 5.11: (a) Electronic band structure and (b) partial density of states for non-spin-orbit calculation. (c) Electronic band structure and (d) partial density of states with spin-orbit included. Also shown in (b) and (d) is the total density of states (TDOS).

Fermi surface

Figure 5.12 displays the Fermi surface (FS) of PrBi with SOI. DFT predicts a spherically symmetric and a star-shaped hole-pocket at Γ shown in Fig. 5.12 (a) and (b), respectively. Additionally, an electron-pocket is found at X as shown in Fig 5.12 (c). The three FS pockets are consistent with three quantum oscillation frequencies observed in experiments. The combined FS and a slice of the FS along the (001) plane are shown in Fig. 5.12 (d) and (e), respectively. To compare with experiments, in Table 5.7 we list the dHvA frequencies predicted by DFT for both with and without inclusion of spin-orbit interaction on DFT-optimized and experimental lattice parameters. The magnetic field H is parallel to the z-axis. To calculate dHvA frequencies we have used the maximally localized Wannier function to generate the Fermi surface. From Table 5.7 we note that the dHvA frequencies have a significant dependence on spin-orbit interaction and volume. So in order to compare with experiment it is very important the DFT calculations capture the correct picture of spin-orbit interaction. We observe that the quantum oscillation frequencies α and β are overestimated and γ is underestimated in DFT calculations. However,

the calculated quantum oscillation frequencies of PrBi without spin-orbit interaction agree fairly well with the experimental data.

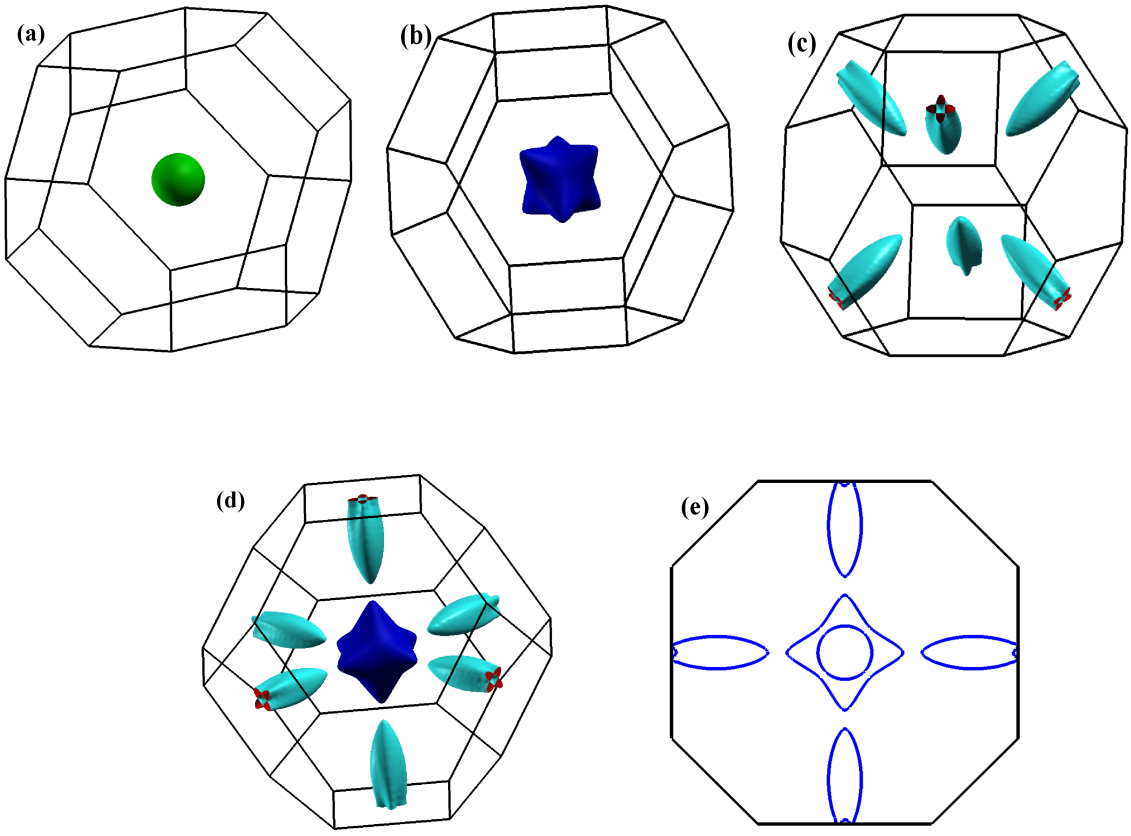

Figure 5.12: (a)–(c) The Fermi surface of PrBi in the first Brillouin zone for each band crossing the Fermi energy. (d) The total Fermi surface including all crossing bands. (e) The Fermi surface slice for (001) plane. In (a) and (b) we show the two hole pockets of the FS at the point and in (c) we show the electron pockets at each X point of the BZ.

Table 5.7: Comparison between DFT-calculated and experimentally observed de Haas-van Alphen (dHvA)/Shubnikov de Haas (SdH) frequencies in (kT). The α is the electron band near X, and β and γ are the hole pockets near Γ. DFT without SOI predicts an extra hole-pocket (β_2) near Γ. Effective mass m^* in m_e is given in parenthesis.

	DFT-Calculated			Experiment
	with-SOI Optimized	no-SOI Exp-lattice	no-SOI Optimized	
α	0.42(0.47)	0.58(0.57)	0.30 (0.15)	0.264
β	0.67(0.16)	0.68(0.16)	0.52(0.10)	0.57
γ	1.3 (0.34)	1.27(0.32)	0.11(0.23)	1.52
β_2	-	-	1.47 (0.34)	

5.4 Conclusion

We have presented a detailed magnetotransport study on high-quality single crystals of the rare earth monopnictides XBi (X = La, Pr). An extremely large nonsaturating magnetoresistance (10^5 %) has been observed, which is due to the compensated semimetallic nature of LaBi and PrBi. The temperature-dependent resistivity in zero magnetic field shows a typical semimetallic character, and a field-induced metal-insulator-like transition is observed at low temperatures. The value of MR and mobility for the Dirac band in LaBi has been found to be larger in comparison to the values reported previously. This is due to the improved quality of the single crystals of LaBi. Fermi surface parameters have been calculated from dHvA quantum oscillations. A small value of effective mass is consistent with the Dirac nature of charge carriers in LaBi. Berry phase has been calculated fitting the quantum oscillation data by full L-K fit analysis. From this fitting, a non-trivial Berry phase close to π for α Fermi pocket clearly suggests the presence of topologically non trivial Dirac type carriers in LaBi.

Magnetic measurements of PrBi are consistent with a localized trivalent Pr^{3+} valence state and reveal paramagnetic temperature dependent behavior down to a temperature of T = 2 K. Thus PrBi is a potential material to observe topological properties in the presence of electronic correlations. Hall measurements reveal a two-carrier compensated nature of transport in PrBi. Pronounced quantum oscillations are observed in the magnetoresistance and magnetization data. We map out the Fermi surface (FS) of PrBi by angle-dependent SdH and dHvA quantum oscillation measurements that reveal a three-dimensional FS made up of two hole bands at the point and an electron band at the X point in the BZ. Our magnetotransport measurements reveal effective masses for the α and β Fermi surface pockets that are quite large and unlikely to arise from Dirac bands. The high mobility that we estimate is therefore somewhat surprising since a high mobility has usually been connected to transport of Dirac electrons in topological materials. The three

FS pockets observed in quantum oscillations are consistent with our electronic-structure calculations. These results are consistent with recent ARPES measurements [175]. The electronic structure calculations also reveal a band inversion along the -X directions leading to expectations of topologically nontrivial effects. A Landau fan diagram analysis gives a value of π for the Berry phase. This is supported by an L-K fitting of the quantum oscillation data, which also gave a Berry phase close to π. This suggests the presence of topologically nontrivial charge carriers in PrBi. Future quantum oscillation measurements to higher fields are desirable to get a more reliable estimate of the Berry phase.

CHAPTER 6

Superconductivity in the topological materials $PdTe_2$ and $Pd:Bi_2Te_3$

6.1 $PdTe_2$

Topological Superconductors (TSCs) have become the focus of recent research because they are theoretically predicted to host Majorana fermion excitation, which can be of vital importance in topological Quantum computation [3, 66] . Previously, Majorana fermions have been theoretically predicted and experimentally observed in the TI/s-wave superconductors heterostructure [176, 177]. The zero energy bound states in the energy gap of a s-wave SC in proximity to the TI mimic the Majorana fermion excitations. Later on, it was conceived of a topological superconducting state in a single stoichiometric compound, instead of the proximity driven topological superconducting state. The superconducting state in $PdTe_2$ below the critical temperature $T_c \approx 1.5$ K was discovred in 1961 [178]. Recently, there has been theoretical prediction that the band structure in the Pt and Pd based tellurides consists of tilted three dimensional linear bands, also classified as the type-II Dirac semimetals. Subsequently, ARPES and magnetotransport measurements have confirmed that $PdTe_2$ is Type-II Dirac semimetal [45, 179]. From our recent quantum oscillations measurements study on the two compounds (chapter3), we have concluded that multiple bands contribute to the transport, including a band with a nontrivial Berry phase [180]. $PdTe_2$ is an interesting material, where topological band structure and superconducting state coexist and therefore there have been speculation that $PdTe_2$ may emerges as a topological superconductor. It was observed that intercalation of

5% Cu in $PdTe_2$ raises its T_c from 1.7 K to 2.4 K [179]. However, its isostructural type-II Dirac semimetal $PtTe_2$ is not a superconductor. It was predicted that, in general, Marojana modes are not stable in Type-I TSMs [3]. However presence of electron and hole pocket in Type-II TSMs favors the large carrier concentration and superconductivity [44]. While there are now several theoretical studies on TSC in type-I topological materials [181, 182], to our knowledge there is only one theoretical study of superconductivity in type-II topological materials [183]. That study showed that unconventional superconductivity with a nodal gap structure will emerge if the superconductivity in $PdTe_2$ involves electrons in the tilted topological band [183]. TSC in $PdTe_2$ is thus an exciting possibility, which needs to be carefully examined.

Recent magnetization and transport experiment shows that $PdTe_2$ is a type-1 superconductor [184]. There magnetization data shows superconductivity with T_c = 1.64 K and quadratic temperature dependent critical field with $H_c(0)$ = 13.46 mT. The nature of superconductivity in $PdTe_2$ is also investigated by STM and STS measurements [185, 186]. However some reports shows that $PdTe_2$ is a type-1 superconductor with multiple critical fields [184, 187]. In this chapter, we present the results of electrical transport, and heat capacity measurements on high quality single crystals of the superconducting type-II Dirac semimetal $PdTe_2$ to explore the possible unconventional (topological) nature of the superconducting state. The electrical transport and heat capacity down to 0.4 K were measured using the He3 option of a quantum design physical property measurement system (QD-PPMS).

Figure 6.1 shows the electrical resistivity ρ versus temperature T measured in zero magnetic field with a current $I = 0.5$ mA applied within the crystallographic ab-plane. The $\rho(T)$ shows metallic behaviour with $\rho(300\,\mathrm{K}) \approx 70\ \mu\Omega\,\mathrm{cm}$ and $\rho(2\,\mathrm{K}) \approx 0.94\ \mu\Omega\,\mathrm{cm}$, giving a residual resistivity ratio $RRR \approx 75$. This RRR is larger than reported earlier indicating that the $PdTe_2$ crystals are of high quality. The lower inset in Fig. 6.1 shows the $\rho(T)$ data below $T = 3$ K and the abrupt drop to zero resistance below $T_c = 1.75$ K confirms the superconductivity in $PdTe_2$. This value of $T_c = 1.75$ K is higher than previous reports [102, 184], further confirm the high quality of single crystals.

Figure 6.2 (a) show the heat capacity C versus temperature T data for $PdTe_2$ between $T = 0.4$ and 3 K measured in $H = 0$ and $H = 500$ Oe magnetic field. A sharp anomaly at $T_c = 1.72$ K in the $H = 0$ data indicates that the superconductivity previously reported using only transport measurements, is bulk in nature. No anomaly is observed down to the lowest temperatures measured in $H = 500$ Oe, suggesting that the superconductivity has been completely suppressed. This is confirmed by our heat capacity data in various magnetic field which will be presented later. The $H = 500$ Oe data was treated as the normal state data and was fit to the expression $C = \gamma T + \beta T^3$. The fit gave the values

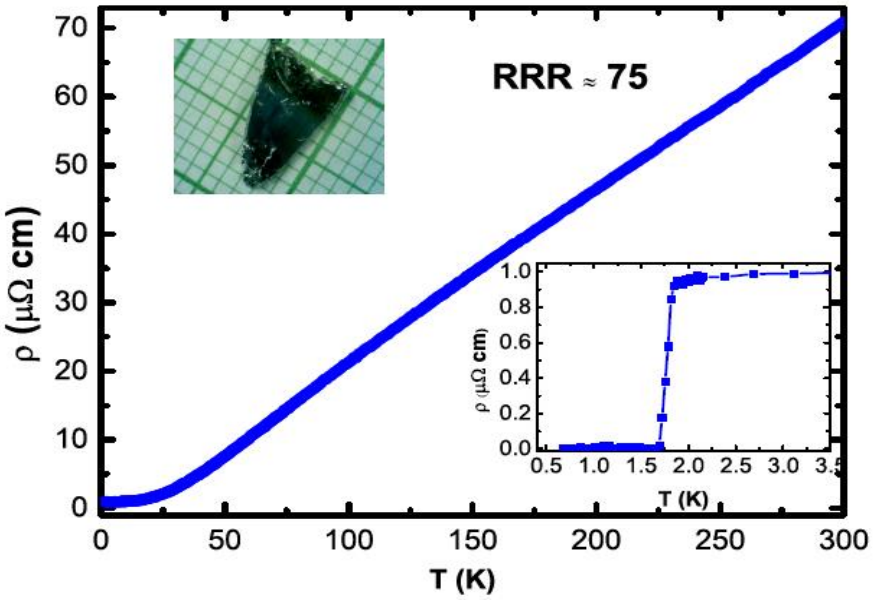

Figure 6.1: Electrical resistivity ρ versus T for $PdTe_2$ measured in zero applied magnetic field with a current $I = 0.5$ mA applied in the crystallographic *ab*-plane. The top inset shows an optical image of a $PdTe_2$ crystal placed on a milimeter grid. The bottom inset shows the $\rho(T)$ data below 3 K to highlight the superconducting transition with $T_c \approx$ 1.75 K.

$\gamma = 6.01(3)$ mJ/mol K^2 and $\beta = 0.66(1)$ mJ/mol K^4. The lattice part βT^3 was then subtracted from the $C(T)$ data at $H = 0$ to obtain the electronic part of the heat capacity C_{el}. The electronic heat capacity divided by temperature C_{el}/T versus T is shown in Fig. 6.2 (b). An extremely sharp transition at the onset of superconductivity is observed at $T_c = 1.72$ K. The normal state Sommerfeld coefficient $\gamma = 6.01$ mJ/mol K^2 is indicated by an extrapolation (dashed line in Fig. 6.2 (b)) to $T = 0$ of the normal state data. An equal entropy construction (not shown) gave almost the same $T_c = 1.69$ K, indicating no broadening or smearing out of the superconducting transition due to sample inhomogeneties or imperfections.

The data at the lowest temperatures were fit by the expression $C_{el}/T = \gamma_{res} + Aexp(-\Delta/T)$, where γ_{res} is the residual Sommerfeld coefficient from the non-superconducting fraction of the sample and the second term is a phenomenological exponential decay expected for a gapped (*s*-wave superconductor) system. The fit shown in Fig. 6.2 (b) as the solid curve through the data below $T = 0.5$ K, gave the value $\gamma_{res} = 0.4$ mJ/mol K^2. With the total $\gamma = 6.01$ mJ/mol K^2, this suggests that $\approx 7\%$ of the sample volume is non-superconducting. An excellent fit of the low temperature C_{el} data to an exponential dependence suggests a conventional *s*-wave superconducting order parameter.

The magnitude of the anomaly in heat capacity at the superconducting transition is

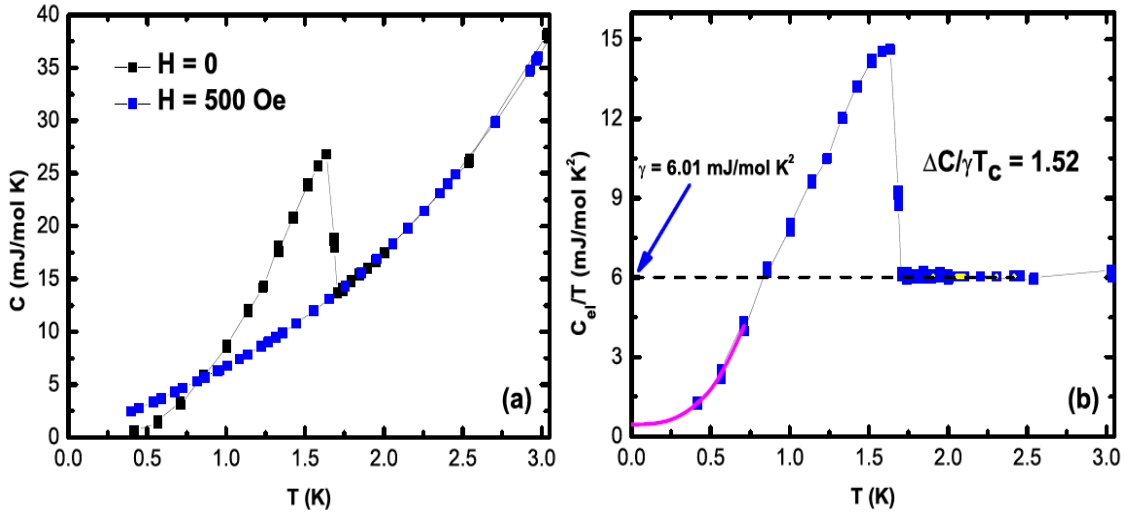

Figure 6.2: (a) Heat capacity C versus T for $PdTe_2$ measured in $H = 0$ and $H = 500$ Oe. (b) Electronic contribution to the heat capacity divided by temperature C_{el}/T. The horizontal dash-dot line is the value $\gamma = 6.01$ mJ/mol K^2 and the solid curve through the lowest T data is a fit by a gapped model.

another measure of the nature (weak or strong coupling, single or multi-gap) of superconductivity. From the data in Fig. 6.2 (b) we estimate $\Delta C/\gamma T_c \approx 1.52$, which is close to the value 1.43 expected for a conventional, weak-coupling, single gap BCS superconductor. This further supports the conventional nature of superconductivity in $PdTe_2$.

Heat capacity measurements at various magnetic fields are shown in Fig. 6.3 (a). As expected, the superconducting transition temperature is monotonically suppressed to lower temperatures and its magnitude becomes smaller at higher fields. From an equal entropy construction for the $C(T)$ data at each H, we extract the T_c at that H and use it to draw a critical-field H_c versus temperature ($H_c - T$) phase diagram. From the $C(T)$ data at various H, the lattice part was subtracted to get the electronic part C_{el}. This data is shown in Fig. 6.3 (b), plotted as C_{el}/T . The data for each H were fit by the expression $C_{el}/T = \gamma_{res} + Aexp(-\Delta/T)$ to get $\gamma_{res}(H)$. For an s-wave superconductor one expects $\gamma_{res}(H) \propto H$. Whereas for a nodal superconductor, $\gamma_{res}(H) \propto H^{1/2}$ is expected, which is called the Volovik effect [188]. Fig. 6.4 (b) shows that $\gamma_{res}(H)$ follows a linear in H dependence, further supporting conventional superconductivity in $PdTe_2$.

The $H_c - T$ phase diagram is shown in Fig. 6.4 (a) and follows a conventional behaviour expected for a BCS superconductor. In particular, we were able to fit the data with the phenomenological expression $H_c(T) = H_c(0)[1 - (T/T_c)^2]$, with the $T = 0$ critical field $H_c(0)$, and the critical temperature T_c as fit parameters. The fit shown as the solid curve through the data in Fig. 6.4 (a) gave the values $H_c(0) = 195(2)$ Oe and $T_c = 1.78$ K, respectively.

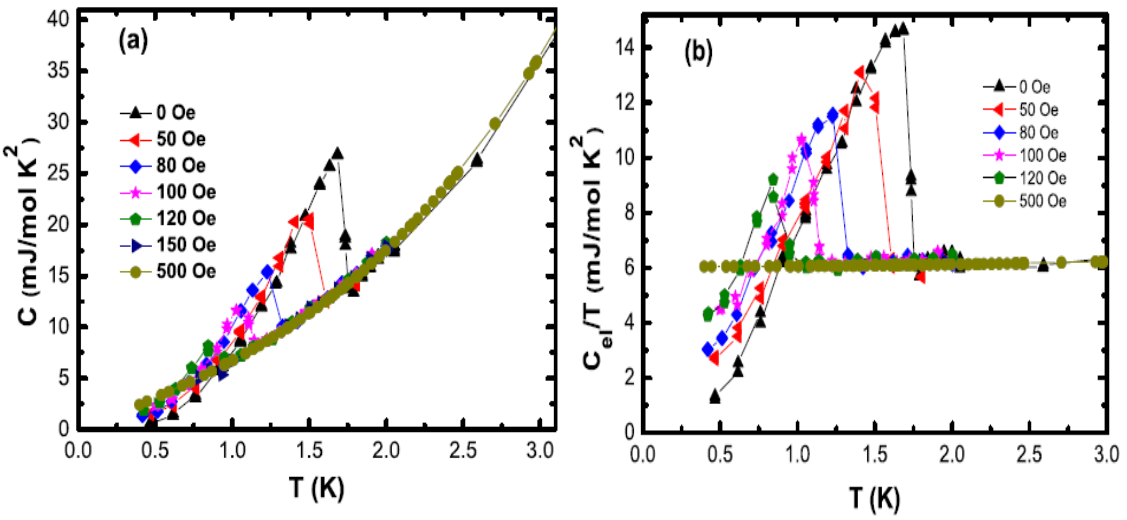

Figure 6.3: (a) Heat capacity C versus T for $PdTe_2$ between $T = 0.4$ and 3 K, measured in various magnetic fields H. (b) The electronic contribution to the heat capacity C_{el} divided by T at various H

In summary, $PdTe_2$ is an interesting material where a superconducting state below $T_c \approx 1.7$ K coexists with a Topological band structure. Specifically, $PdTe_2$ has previously been shown to be a Type-II Dirac semi-metal raising the possibility of hosting a Topological superconducting state. A recent theoretical study of superconductivity in type-II Weyl metals, relevant for $PdTe_2$, predicts a superconducting state with nodes in the gap function [183]. Such a state leads to a $C_{el} \sim T^3$ behavior in the superconducting state in the lowtemperature limit. This in turn would lead to a reduced jump in the heat capacity at T_c. Nodes in the gap function also lead to the observation of the Volovik effect in a magnetic field, $C_{el}/T \sim \sqrt{H}$ [188].

In this study we have used thermodynamic measurements on high quality single crystals of $PdTe_2$ to probe the nature of the superconductivity. Our heat capacity measurements confirm bulk superconductivity at $T_c = 1.7$ K and show that the anomaly at T_c is characterized by the ratio $\Delta C/\gamma T_c \approx 1.5$ which is close to the value 1.43 expected for a weak-coupling, single-band BCS superconductor. The electronic contribution to the heat capacity C_{el} at the lowest temperatures shows an exponential T dependence which points to a gapped s-wave superconductivity. From H dependent $C(T)$ measurements, we find $C_{el}/T \sim H$, in contrast with behavior expected for nodal superconductivity. Additionally, the critical field versus temperature phase diagram shows a behaviour expected for a conventional superconductor. Therefore, all our results strongly indicate that inspite of the presence of a topological band in the electronic band-structure of $PdTe_2$ which contributes to the transport properties, the superconductivity in $PdTe_2$ is completely conventional and has no Topological character.

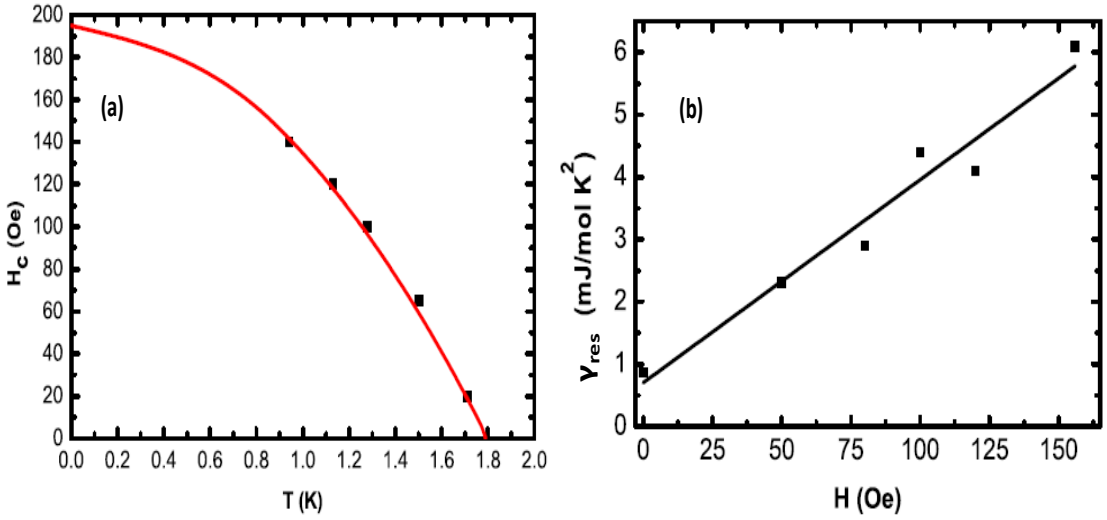

Figure 6.4: (a) The critical magnetic field H_c versus temperature T phase diagram extracted from the C versus T data measured at various H. The solid curve through the data is a fit by a phenomenological dependence. (b) The $T = 0$ value of the Sommerfeld coefficient $\gamma_{res} = C_{el}/T$ vs H. The solid line through the data is a linear fit.

While there are very few direct predictions of signatures of TSC in heat capacity measurements, most theoretical work on TSC predict unconventional order parameterswith point or line nodes in the SC gap structure. Nodes in the gap structure would lead to a nonexponential T dependence of th electronic heat capacity in the SC state as T $\longrightarrow$ 0. There are also predictions of mixed order parameters with an s-wave component plus other unconventional components to the SC gap. In such cases, depending on the fraction of the unconventional component, the heat capacity could be exponential (mostly s-wave component) or might deviate from it. However, because of this extra non-s-wave component, the entropy balance w necessarily lead to the jump in the heat capacity at T_c to become smaller than the BCS value. In our case, the jump is close to and, in fact, slightly larger than the BCS value. Thus, our heat capacity results rule out such scenarios. So, in the least, our results put strong constraints on what kind of TSC, if any at all, could exist in $PdTe_2$.

6.2 Pd:Bi_2Te_3

Recent theoretical prediction and experiment observation confirm that superconductors derived from TIs are favorable candidates for realizing TSCs [189, 190]. The high spin orbit coupling in TIs favours the unconventional elecrton pairing in superconductors derived from TIs. Now, there are several material systems experimentally shown to host superconductivity in a topological material. Such material systems includes Cu

intercalated Bi_2Se_3 [191], the topological crystalline material $Sn_{1-x}In_xTe$ [77], Cu intercalated $(PbSe)_5(Bi_2Se_3)_6$ [176], Sr intercalated Bi_2Se_3 [192], Nb intercalated Bi_2Se_3 [193] and Pd intercalated Bi_2Te_3 [194]. While there are several studies reporting on the superconducting properties of the other material systems, there is only a single report on the occurrence of superconductivity in $Pd_xBi_2Te_3$ [194]. Since TSCs have been predicted to be avenues to host Majorana Fermions as emergent quasi-particles, it is therefore important to study in detail the superconducting properties of various candidate topological superconductors candidate.

Here we present synthesis, electrical transport, and magnetic properties of novel Pd intercalated topological insulator Bi_2Te_3. We construct magnetic field vs. temperature H–T and pressure vs. temperature P–T phase diagrams for superconductivity in this material.

Single crystals and polycrystalline samples of $Pd_xBi_2Te_3$ ($x \approx 1$) were grown using a Bridgeman technique or by conventional solid state reaction, respectively. The XRD patterns were obtained at room temperature using a Rigaku Geigerflex diffractometer with Cu Kα radiation. Chemical analysis was done using energy dispersive spectroscopy (EDS) on a JEOL SEM. Electrical transport was measured using a Quantum Design Physical Property Measurement System (PPMS). Magnetic susceptibility $\chi(T)$ at various pressures $P \leq 1.3$ GPa were measured using a Cu-Be pressure cell with the VSM option of a Quantum Design PPMS.

Large shiny crystals could be easily cleaved from the as grown boule. Chemical analysis gave the approximate chemical stoichimotery $Pd_{0.93}Bi_2Te_3$ which we will call $PdBi_2Te_3$. Some crystals were crushed into powder for X-ray diffraction measurements. The PXRD measurements shown in Fig. 6.5 confirmed the majority phase to be Bi_2Te_3 with lattice parameters a = 4.378(5) Å, c = 30.499(7) Å which are close to those of Bi_2Te_3 (a = 4.375 Å, c = 30.385 Å) but with a slightly enhanced c-axis parameter which is most likely due to Pd intercalation between layers. We note that it is difficult to predict whether the lattice parameters will increase or decrease on intercalation, and by how much. We point to two examples of intercalated layered materials which become superconducting. For one material the lattice parameters increase on intercalation while for the other they decrease. These examples are Cu_xTiSe_2 [195] and Zn_xZrNCl [196], respectively. For Cu_xTiSe_2 the lattice parameters increase from $a = 3.54$ Å and $c = 6.01$ Å to $a = 3.546$ Å and $c = 6.045$ Å after intercalation. These changes are less than 0.5 %. For Zn_xZrNCl, the lattice parameters decrease from $a = 3.595$ Å and $c = 27.640$ Å to $a = 3.580$ Å and $c = 27.592$ Å after intercalation. A decrease of less than 0.5 %. For our samples we find an increase of similar magnitude. The PXRD data shows the presence of secondary phases such as $PdTe_2$, BiPdTe, and $Pd_{72}Bi_{19}Te_9$. This is consistent with the

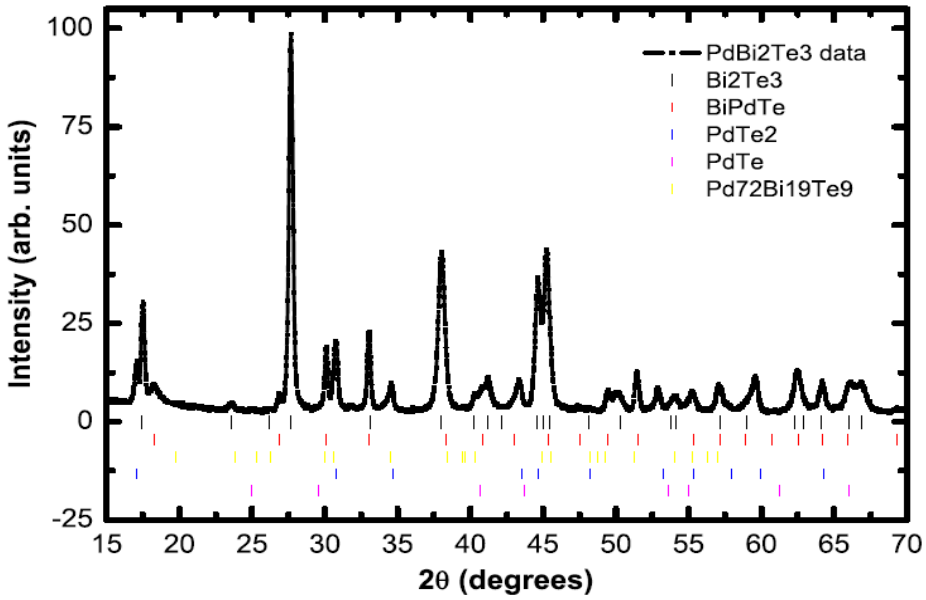

Figure 6.5: Powder x-ray diffraction (PXRD) data for $PdBi_2Te_3$. The vertical bars below the data are the expected Bragg positions for the various phases suspected to be present in the sample.

earlier report [194]. We point out that none of the observed impurity phases are reported to superconduct above $T = 2$ K and therefore do not interfere with our goal in the present work which is to study the effect of magnetic field and pressure on superconductivity in $PdBi_2Te_3$. The phase PdTe is a known superconductor with $T_c \approx 4.5$ K. However, we did not observe any trace of superconductivity at 4.5 K in our measurements.

Magnetic susceptibility was measured for two different polycrystalline samples. The percentage superconducting volume fraction (in a zero field cooled measurement) given as 4π times the volume magnetic susceptibility $\chi_V = M/H$ versus T data for two $PdBi_2Te_3$ samples between $T = 2$ K and 8 K measured in various applied magnetic fields are shown Figs. 6.6 (a) and (b). The onset $T_c = 5.5$ K and the small superconducting fraction (VF) of about 1.5% are consistent with the previous report [191]. The small value of VF in $PdBi_2Te_3$ could be due to presence of anticite defects in Bi_2Te_3 which might makes difficulty in the interclation of Pd in between the layers of Bi_2Te_3. The inset in Fig. 6.6 (a) shows the data on a scale where the onset of the superconducting transition for various magnetic fields can be seen clearly. As expected, the onset T_c shifts to lower temperatures with increasing magnetic fields. Figure 6.6 (b) insets show the construction (intersection of linear extrapolations of the data above and below T_c) that was used to determine the onset T_c. From these data, the onset T_c at various magnetic fields H was extracted and an H–T phase diagram drawn. These data are plotted in Fig. 6.8.

Figure 6.7 (a) shows the ac electrical resisitivity ρ of $PdBi_2Te_3$ for $T \leq 8$ K mea-

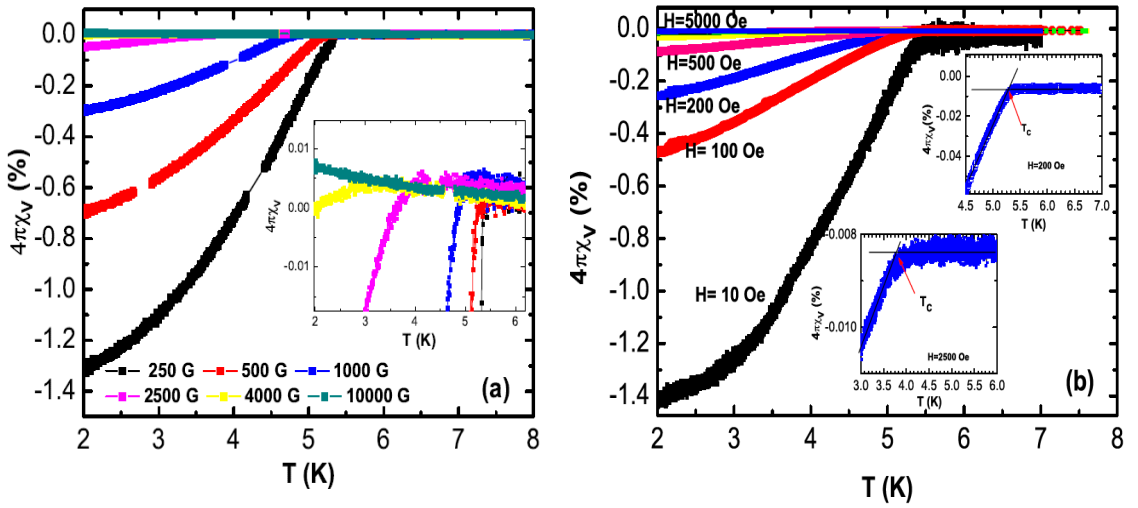

Figure 6.6: Magnetic susceptibility χ versus temperature T data below $T = 8$ K measured in various magnetic fields H for two different samples of $PdBi_2Te_3$. The data is plotted as the superconducting volume fraction $4\pi\chi_V$. The inset in (a) shows the data on a scale so that the suppression of the onset of superconductivity with increasing magnetic fields can be seen clearly. The inset in (b) shows the construction used to detrmine the onset T_c for different H.

sured at various magnetic fields. At $H = 0$ we observe the onset of superconductivity at $T_c = 5.5$ K. This onset T_c is depressed to lower temperatures with increasing H. The ρ values do not fall to zero in the superconducting state which is consistent with the earlier report.[191]. However, the Meissner effect and the depression of T_c with H confirms superconductivity in $PdBi_2Te_3$. The onset T_c at various magnetic fields H were extracted from these data and an H–T phase diagram was drawn. These data are also plotted in Fig. 6.8 (b).

Figure 6.7 (b) shows the low temperature magnetization versus temperature data at two pressures: $P = 0$ and $P = 1.28$ GPa. In these measurements, Sn was used as a manometer. The superconducting T_c for Sn (not shown) at various pressures was used to determine the pressure. To reveal the superconductivity of $PdBi_2Te_3$ over the background of the pressure cell we had to apply a fairly large magnetic field of $H = 100$ Oe. Figure 6.7 (b) inset shows a typical magnetization plot where the superconducting transition can be seen as a sudden downturn of the data on top of a paramagnetic signal from the cell. This paramagnetic background signal was subtracted from the raw data to give plots shown in the main panel of Figure 6.7 (b). Figure 6.7 (b)shows that the T_c for $PdBi_2Te_3$ is suppressed to lower temperatures on increasing pressure. Similar measurements were performed at pressures $P \approx 0, 0.2, 0.6, 0.9, 1.28$, respectively. These data were used to extract the onset T_c for each P. Figure 6.8 (a) shows the P–T phase diagram for $PdBi_2Te_3$ for $P \leq 1.3$ GPa. We find that the T_c is suppressed approximately linearly with pressure at

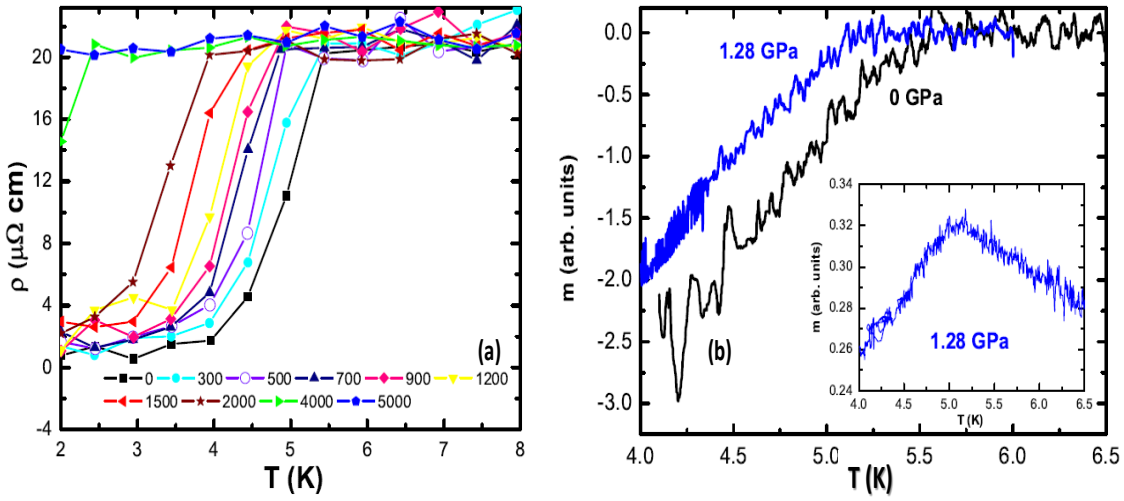

Figure 6.7: (a) Low temperature resistivity ρ versus temperature T for $PdBi_2Te_3$ at various applied magnetic fields H. (b) Magnetization versus temperature at different pressures measured in a magnetic field of $H = 100$ Oe. The inset shows the magnetization data of the pressure cell plus the $PdBi_2Te_3$ sample highlighting the abrupt downturn of the data on the onset of superconductivity.

a rate $dT_c/dP \approx -0.28$ K/GPa. The effect of pressure on T_c of $PdBi_2Te_3$ can be explained by McMillan equation [197, 198]

$$T_c = \frac{\hbar < \omega >}{1.20} exp\left\{\frac{-1.40(1+\lambda)}{\lambda - \mu^*(1+0.62\lambda)}\right\}, \tag{6.1}$$

where $< \omega >$ is an average phonon frequency, λ is the electron phonon coupling parameter and μ^* is the Coulomb repulsion term. The volume (V) derivative of equation 6.1 can be written as

$$\frac{d\ln T_c}{d\ln V} = -B\frac{d\ln T_c}{dp} = \gamma + \Delta\left\{\frac{d\ln \eta}{d\ln V} + 2\gamma\right\}, \tag{6.2}$$

where B is the bulk modulus, $\gamma \equiv = -d\ln < \omega > /d\ln V$ the Gruneisen parameter, $\eta = N(E_f) < I^2 >$, I^2 is the average squared electronic matrix element, $\Delta = 1.04\lambda[1+1.38\mu^*][\lambda - \mu^*(1+0.62\lambda)]^{-2}$. For simple metallic superconductors typical value of $2\gamma \approx +3$ to $+5$ and $d\ln\eta/d\ln V \approx -1$. Since value of $-\gamma$ is small and Δ is always positive the sign of dT_c/dP is negative. Therefore due to lattice stiffening with pressure, T_c decreases in simple metals. For example T_c for Sn suppressed to lower temperature linearly with pressure P at a rate of $dT_c/dP \approx -0.482$ K/GPa [199].

In summary, we have synthesized single crystals and polycrystals of Pd intercalated Bi_2Te_3, confirmed the occurrence of superconductivity with a $T_c = 5.5$ K, and studied the superconducting properties under magnetic field H and externally applied pressure P. The

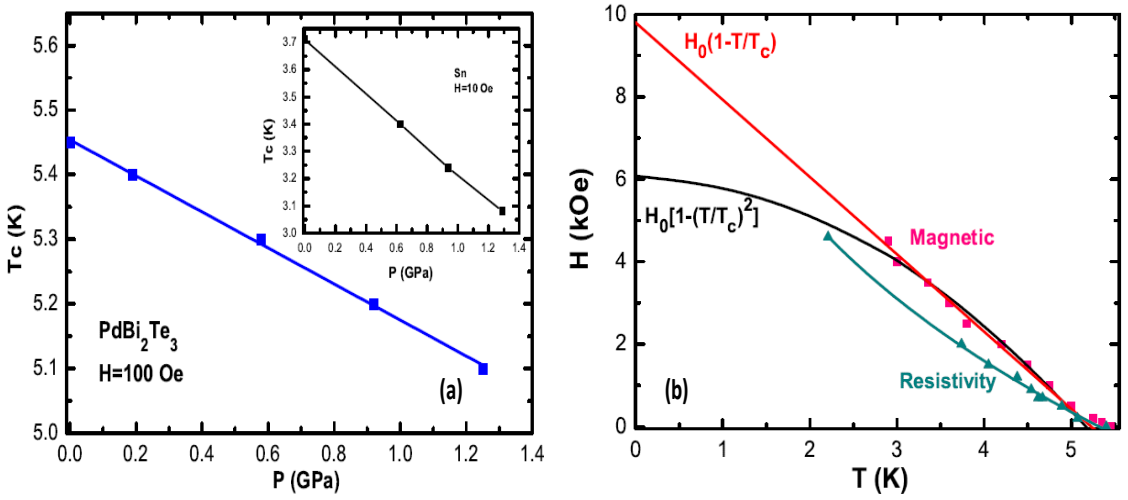

Figure 6.8: (a) Pressure P dependence of the superconducting transition temperature T_c for $PdBi_2Te_3$. Inset shows the P-vs-T_c for Sn which was used as a manometer. (b) The magnetic field-temperature phase diagram for $PdBi_2Te_3$ determined from the magnetic and electrical transport measurements. The curves through the data are fits to different models.

magnetic field-temperature (H–T) phase diagram extracted from both electrical transport and magnetic measurements show an upward curvature near T_c as has been previously observed for several unconventional superconductors like high T_c cuprates and organic superconductors [200, 201] as well as for the multi-gap superconductor MgB_2 [202]. We tried to fit our H–T data using phenomenological models that have been used previously for conventional BCS type superconductors. Figure 6.8 (b) shows results of our attempts to fit the H–T data obtained using the magnetic measurements described above with the expression $H(T) = H_0[1 - (\frac{T}{T_c})^n]$, for fixed $n = 1$ or 2, where H_0 is the $T = 0$ critical field. It can be seen from Fig. 6.8 (b) that the fit for $n = 2$ is extremely poor and the fit for $n = 1$ is satisfactory only at lower temperatures away from the $H = 0$ critical temperature $T_c = 5.5$ K. The H_0 obtained in these fits range approximately from 6 to 10 kOe. If n is allowed to vary as a fit parameter, the best fit is obtained for $n < 1$ confirming the unconventional upward curvature. For example, the fit giving $n \approx 0.4$ is shown as the solid curve through the H–T data obtained from the resistivity measurements. This $H(T)$ behavior is unusual and suggests the possibility of unconventional superconductivity in $PdBi_2Te_3$.

Additionally, from high pressure magnetic measurements we found that T_c is suppressed to lower temperatures approximately linearly with pressure P at a rate $dT_c/dP \approx -0.28$ K/GPa. This suppression of T_c with pressure is expected for conventional electron-phonon mediated superconductivity and occurs due to the stiffening of the lattice with

pressure. The H–T and P–T phase diagrams therefore give seemingly conflicting results about the nature (conventional or unconventional) of superconductivity in $PdBi_2Te_3$. We note that MgB_2 also shows such conflicting behaviors [202, 203]. MgB_2 is an electron-phonon mediated superconductor and hence its T_c decreases with pressure P. The unconventional upward curvature in its H–T phase diagram most likely arises due to its two-gap nature. The reason for such behavior in $PdBi_2Te_3$ is not understood at present.

CHAPTER 7

Summary and Outlook

7.1 Summary

In this thesis, we have investigated the topological character and nature of Fermi surfaces of some topological quantum materials by utilizing electrical, magnetic and heat capacity measurements. In these magnetotransport measurements, we have explored the electrical and magnetic characteristics of the topological band structure by performing various experiments such as, angle dependent MR and magnetization measurements, in-plane resistivity measurements for the planar Hall effect, and low-temperature heat-capacity measurements. We have successfully identified the topological character of some of the semimetals. wW have also grown high quality single crystals of the $Bi_{1-x}Sb_x$ ($0 \leq x \leq .16$), $PdTe_2$, $Pd_xBi_2Te_3$ ($x \approx 1$) and $PtTe_2$, XBi (X = La, Pr) by modified Bridgman and flux growth techniques, respectively.

In our study the detailed magnetotransport properties of high quality single crystals of $Bi_{1-x}Sb$, covering a large TI range x = 0.032 – 0.16 has been carried out. The quality of these crystals has been found to be unprecedented in comparison to the other reports, which is reflected by the very large MR, exceptionally large mobility and the mean free path of the carriers. We have for the first time, shown the topological phase transition from the trivial to nontrivial topological state by analyzing the cyclotron orbit phase of the carriers, also known as the quantized Berry phase. Additionally, we have pinned down the topological critical point, where a Dirac semimetal evolves into a strong topological insulator as we changes the spin-orbit interaction strength (by increasing the Sb doping concentration). From the Landau fan diagram analysis of the quantum oscillation data

around this quantum critical point, we track the evolution of the Berry phase across the topological transition around $x \approx 0.03$. A signature of the Weyl state is the observation of a chiral anomaly. We provide clear evidence that in addition to the crystal at x = 0.032 which is at the topological phase transition, samples at x = 0.072 and 0.16 also show pronounced chiral magnetic effect with a negative LMR which is strongly suppressed on increasing the angle between B and I. We have addressed the additional microscopic mechanisms, other than chiral anomaly, responsible for the appearance of the negative MR in a very high mobility crystal with chemical inhomogeneity causing the conductivity fluctuations. Additionally, the non-linear I–V is observed for x = 0.16 crystals only when B$\|$ I, thus confirming the Weyl state of the $Bi_{1-x}Sb$. The negative LMR for x = 0.16 was the strongest. These observations strongly indicate that a WSM state exists for other compositions of x even far away from the topological phase transition at x = 0.03.

Second part of this thesis work is devoted to the angle and temperature dependent magnetotransport measurements on high quality single crystals of ATe_2 (A = Pd, Pt), a theoretically predicted type-II Dirac semimetal family consisting of tilted bulk Dirac cone. Multiple frequencies for both field orientations (B $\|$ c and B $\|$ ab) have been observed in the fast Fourier transform (FFT) spectra of the quantum oscillation data which suggests multiple Fermi pockets crossing the Fermi level. The number and positions of the frequencies suggest different band structures for $PdTe_2$ and $PtTe_2$. Extracted transport parameters for $PtTe_2$ reveal a strong anisotropy which might be related to the tilted nature of the Dirac cone. Using a Landau level fan diagram analysis we find at least one Fermi surface orbit with a Berry phase of π consistent with Dirac electrons for both $PtTe_2$ and $PdTe_2$. The light effective mass and high mobility are also consistent with Dirac electrons in AT_2 (A = Pd, Pt). Our results therefore suggest that $PdTe_2$ and $PtTe_2$ are three-dimensional Dirac semimetals. Owing to the deeply rooted Dirac points below the Fermi level in the $PtTe_2$ (0.8eV) and $PdTe_2$ (1eV), we could not observe chiral anomaly induced negative MR. However, we have observed the planar Hall effect (PHE) in type-II Dirac semimetal $PtTe_2$, the origin of which is not clear at the moment and further theoretical and experimental investigation of these findings are needed to pin down the exact physical mechanism behind the appearance of this unusual effect, especially in non-magnetic material systems. Interesting part in this observation is that PHE is observable up to room temperature, suggesting the robustness of the relativistic carriers against the electron-phonon scattering. Thus our observation of PHE for a system like $PtTe_2$ therefore suggests that PHE can be used as a crucial transport diagnostic for topological character even for band structures with Dirac nodes slightly away from the Fermi energy. At present, in these non-magnetic systems, anisotropic transport driven by the layered structure of the Van der Waals materials seems to be possible origin of this PHE. Future

work on these material systems focusing on the change of dimensionality and locating the chemical potential in the vicinity of tilted Dirac node will certainly shed light on the microscopic origin of this effect.

In the next part of the work, we have probed the topological character and nature of Fermi surface of XBi (X = La, Pr) by measuring the angle and temperature dependent SdH and dHvA oscillations. An extremely large nonsaturating magnetoresistance (10^5 %) has been observed, which is due to the compensated semimetallic nature of LaBi and PrBi. The FFT spectra of dHvA oscillations of LaBi, reveal two different oscillation frequencies F(α) = 273 T and F(β) = 603 T. The presence of these two frequencies indicates the presence of two Fermi surface pockets in the band structure of LaBi. The Dirac nature of the charge carriers in LaBi has been confirmed by extracting a Berry phase of π by fitting the quantum oscillations by L-K formula. After confirming the presence of Dirac semimetal phase in LaBi, we extended our study to a new material PrBi. PrBi is a novel material in which the presence of f electrons, in addition to the possible topological band structure raises the prospect of realizing a strongly correlated version of topological semimetals. Our magnetic measurements of PrBi are consistent with a localized trivalent Pr^{3+} valence state and reveal paramagnetic temperature dependent behavior down to a temperature of T = 2 K. We map out the Fermi surface (FS) of PrBi by angle-dependent SdH and dHvA quantum oscillation measurements that reveal a three-dimensional FS made up of two hole bands at the point and an electron band at the X point in the BZ. The three FS pockets observed in quantum oscillations are consistent with our electronic-structure calculations. A L-K fitting of the quantum oscillation data as well as a Landau fan diagram analysis gave a Berry phase close to π, suggesting the presence of Dirac fermions in PrBi.

Lastly in the final chapter of this thesis, we examined the nature of superconductivity in $PdTe_2$ and $PdBi_2Te_3$. $PdTe_2$ is an interesting material, where topological band structure and superconducting state coexist. Our heat capacity measurements confirm bulk superconductivity at T_c = 1.7 K and show that the anomaly at T_c is characterized by the ratio $\Delta C / \gamma T_c \approx 1.5$, which is close to the value 1.43 expected for a weak-coupling, single-band BCS superconductor. The electronic contribution to the heat capacity C_{el} at the lowest temperatures shows an exponential T dependence, which points to a gapped s-wave superconductivity. From H dependent C(T) measurements, we find C_{el}/ T $\sim$ H, in contrast with behavior expected for nodal superconductivity. Additionally, the critical field versus temperature phase diagram shows a behavior expected for a conventional superconductor. Thus, our measurements strongly indicate that the superconductivity in $PdTe_2$ is conventional in nature despite the presence of topologically nontrivial electrons contributing to the transport. The superconductors derived from TIs are favorable candidates for realiz-

ing TSCs. We studied the superconducting properties of $PdBi_2Te_3$ under magnetic field H and externally applied pressure P. We confirm superconductivity with a $T_c \approx 5.5$ K. The H–T phase diagram extracted from both electrical transport and magnetic measurements show an upward curvature near T_c as has been previously observed for several unconventional superconductors like high T_c cuprates and organic superconductors as well as for the multi-gap superconductor MgB_2. From high pressure magnetic measurements we found that T_c is suppressed to lower temperatures approximately linearly with pressure which is expected for conventional superconductors. The H–T and P–T phase diagrams therefore give seemingly conflicting results about the nature (conventional or unconventional) of superconductivity in $PdBi_2Te_3$. A future detailed study is needed to confirm nature of superconductivity in $PdBi_2Te_3$.

7.2 Outlook

The research on topological phases of matter has been greatly intensified due to its fundamental importance and possible technological applications in spintronics and quantum computation. Last decade has witnessed great improvement in the synthesis and understanding of topological materials. However there are some challenges in the research field of topological materials. One of these challenges is the complete bulk conduction suppression in case of the topological insulators and thus the realization of the surface Dirac states dominant transport. This is known as topological transport regime, where chemical potential lies near the Dirac point in the bulk band gap, with no impurity band. First Bi and Sb based alloy solution was discovered as the first topological insulator along with other Bi and Sb based binary tellurides and selenides. However, all these material systems were found to be highly bulk conducting owing to the defect generated residual carrier density. However recent transport experiments shows that bulk conductance of Bi_2Se_3 can be reduced by Ca doping. Another promising way to get rid of bulk state is the growth of epitaxial thin films. BiSbTeSe2 is one of the most bulk insulating topological insulator candidate materials till date, but still plagued by the spatially fluctuating electronic band structure due to the formation of local electron-hole puddle. This optimization process of removing electron-hole puddle is being carried out by growing these crystals in various growth conditions, while this thesis is being written.

Apart from TIs, DSMs/WSMs have been the focus of intense recent research. However, various research groups around the globe are still looking for realization of intrinsic Weyl/Dirac semimetals, with no interference from the presence of the other trivial Fermi pockets near the Fermi level. In existing majority of DSMs/WSMs, trivial Fermi pockets coexist with Weyl/topological Fermi pockets, which makes it difficult in interpreting the

experimental results. For example $PdTe_2$ and $PtTe_2$ (studied in the present thesis) have several trivial Fermi pockets which complicate the truly intrinsic character of the tilted Dirac cone in these materials. Research groups worldwide including ours are still searching for ideal topological semimetals which exhibit single pair of Weyl points with Weyl points being close to the Fermi energy. For example the Dirac points in $PdTe_2$ and $PtTe_2$ lies 1 eV and 0.8 eV below the Fermi level respectively. In this direction Pt/Pd doping in $IrTe_2$ has been suggested to cause the Dirac point to approach the Fermi level. This work is currently in progress in our Novel Materials Lab. By following current findings on these material systems, we are hopeful of locating the topological superconducting state in the Pd/Pt doped $IrTe_2$. Further it could be possible to tune the Fermi level close to Dirac/Weyl point by external parameters such as pressure. A topic of immense current interest is trying to combine topological character with strong electronic correlations. The Kondo insulator SmB_6 and the pyrochlore iridates $R_2Ir_2O_7$ are examples of materials that are candidates to show exotic properties from a combination of topology and electron correlations. The Experimental realization of Majorana fermions in TSCs is still an open issue. These Majorana excitations are of fundamental as well as technological interest and can also be utilized in fault-tolerant Quantum computation. There may be several other potentially useful application for topolgical systems.

Bibliography

[1] M. Z. Hasan and C. L. Kane, Rev. Mod. Phys. **82**, 3045 (2010).

[2] N. P. Armitage, E. J. Mele, and A. Vishwanath, Rev. Mod. Phys. **90**, 015001 (2018).

[3] M. Sato and Y. Ando, Reports on Progress in Physics **80**, 076501 (2017).

[4] K. v. Klitzing, G. Dorda, and M. Pepper, Phys. Rev. Lett. **45**, 494 (1980).

[5] L. LANDAU and E. LIFSHITZ, in *Statistical Physics (Third Edition)*, edited by L. LANDAU and E. LIFSHITZ (Butterworth-Heinemann, Oxford, 1980) third edition ed., pp. 1 – 33.

[6] B. M. Victor, Proceedings of the Royal Society of London. A. Mathematical and Physical Sciences **392**, 45 (1984).

[7] D. J. Thouless, M. Kohmoto, M. P. Nightingale, and M. den Nijs, Phys. Rev. Lett. **49**, 405 (1982).

[8] C. L. Kane and E. J. Mele, Phys. Rev. Lett. **95**, 226801 (2005).

[9] B. A. Bernevig and S.-C. Zhang, Phys. Rev. Lett. **96**, 106802 (2006).

[10] X.-L. Qi and S.-C. Zhang, Physics Today **63**, 33 (2010), https://doi.org/10.1063/1.3293411 .

[11] C. L. Kane and E. J. Mele, Phys. Rev. Lett. **95**, 146802 (2005).

[12] L. Fu and C. L. Kane, Phys. Rev. B **74**, 195312 (2006).

[13] M. König, S. Wiedmann, C. Brüne, A. Roth, H. Buhmann, L. W. Molenkamp, X.-L. Qi, and S.-C. Zhang, Science **318**, 766 (2007), https://science.sciencemag.org/content/318/5851/766.full.pdf .

[14] L. Fu, C. L. Kane, and E. J. Mele, Phys. Rev. Lett. **98**, 106803 (2007).

[15] R. Roy, Phys. Rev. B **79**, 195322 (2009).

[16] J. E. Moore and L. Balents, Phys. Rev. B **75**, 121306 (2007).

[17] L. Fu and C. L. Kane, Phys. Rev. B **76**, 045302 (2007).

[18] D. Hsieh, D. Qian, L. Wray, Y. Xia, Y. S. Hor, R. J. Cava, and M. Z. Hasan, Nature **452**, 970 EP (2008).

[19] H. Zhang, C.-X. Liu, X.-L. Qi, X. Dai, Z. Fang, and S.-C. Zhang, Nature Physics **5**, 438 EP (2009), article.

[20] Y. Xia, D. Qian, D. Hsieh, L. Wray, A. Pal, H. Lin, A. Bansil, D. Grauer, Y. S. Hor, R. J. Cava, and M. Z. Hasan, Nature Physics **5**, 398 EP (2009).

[21] Y. L. Chen, J. G. Analytis, J.-H. Chu, Z. K. Liu, S.-K. Mo, X. L. Qi, H. J. Zhang, D. H. Lu, X. Dai, Z. Fang, S. C. Zhang, I. R. Fisher, Z. Hussain, and Z.-X. Shen, Science **325**, 178 (2009), https://science.sciencemag.org/content/325/5937/178.full.pdf .

[22] D. Hsieh, Y. Xia, D. Qian, L. Wray, F. Meier, J. H. Dil, J. Osterwalder, L. Patthey, A. V. Fedorov, H. Lin, A. Bansil, D. Grauer, Y. S. Hor, R. J. Cava, and M. Z. Hasan, Phys. Rev. Lett. **103**, 146401 (2009).

[23] Y. Jiang, Y. Wang, M. Chen, Z. Li, C. Song, K. He, L. Wang, X. Chen, X. Ma, and Q.-K. Xue, Phys. Rev. Lett. **108**, 016401 (2012).

[24] Z. Wang, Y. Sun, X.-Q. Chen, C. Franchini, G. Xu, H. Weng, X. Dai, and Z. Fang, Phys. Rev. B **85**, 195320 (2012).

[25] A. A. Burkov, Nature Materials **15**, 1145 (2016).

[26] S. M. Young, S. Zaheer, J. C. Y. Teo, C. L. Kane, E. J. Mele, and A. M. Rappe, Phys. Rev. Lett. **108**, 140405 (2012).

[27] S.-M. Huang, S.-Y. Xu, I. Belopolski, C.-C. Lee, G. Chang, B. Wang, N. Alidoust, G. Bian, M. Neupane, C. Zhang, S. Jia, A. Bansil, H. Lin, and M. Z. Hasan, Nature Communications **6**, 7373 EP (2015), article.

[28] T. Liang, Q. Gibson, M. N. Ali, M. Liu, R. J. Cava, and N. P. Ong, Nature Materials **14**, 280 EP (2014).

[29] X. Huang, L. Zhao, Y. Long, P. Wang, D. Chen, Z. Yang, H. Liang, M. Xue, H. Weng, Z. Fang, X. Dai, and G. Chen, Phys. Rev. X **5**, 031023 (2015).

[30] Y. Ando, Journal of the Physical Society of Japan **82**, 102001 (2013).

[31] S. Murakami, New Journal of Physics **9**, 356 (2007).

[32] S. M. Young, S. Chowdhury, E. J. Walter, E. J. Mele, C. L. Kane, and A. M. Rappe, Phys. Rev. B **84**, 085106 (2011).

[33] S.-Y. Xu, Y. Xia, L. A. Wray, S. Jia, F. Meier, J. H. Dil, J. Osterwalder, B. Slomski, A. Bansil, H. Lin, R. J. Cava, and M. Z. Hasan, Science **332**, 560 (2011), https://science.sciencemag.org/content/332/6029/560.full.pdf .

[34] M. Brahlek, N. Bansal, N. Koirala, S.-Y. Xu, M. Neupane, C. Liu, M. Z. Hasan, and S. Oh, Phys. Rev. Lett. **109**, 186403 (2012).

[35] J. A. Steinberg, S. M. Young, S. Zaheer, C. L. Kane, E. J. Mele, and A. M. Rappe, Phys. Rev. Lett. **112**, 036403 (2014).

[36] Z. Wang, H. Weng, Q. Wu, X. Dai, and Z. Fang, Phys. Rev. B **88**, 125427 (2013).

[37] H. Weyl, Zeitschrift für Physik **56**, 330 (1929).

[38] X. Wan, A. M. Turner, A. Vishwanath, and S. Y. Savrasov, Phys. Rev. B **83**, 205101 (2011).

[39] A. A. Burkov and L. Balents, Phys. Rev. Lett. **107**, 127205 (2011).

[40] H. Weng, C. Fang, Z. Fang, B. A. Bernevig, and X. Dai, Phys. Rev. X **5**, 011029 (2015).

[41] B. Q. Lv, H. M. Weng, B. B. Fu, X. P. Wang, H. Miao, J. Ma, P. Richard, X. C. Huang, L. X. Zhao, G. F. Chen, Z. Fang, X. Dai, T. Qian, and H. Ding, Phys. Rev. X **5**, 031013 (2015).

[42] S.-Y. Xu, I. Belopolski, N. Alidoust, M. Neupane, G. Bian, C. Zhang, R. Sankar, G. Chang, Z. Yuan, C.-C. Lee, S.-M. Huang, H. Zheng, J. Ma, D. S. Sanchez, B. Wang, A. Bansil, F. Chou, P. P. Shibayev, H. Lin, S. Jia, and M. Z. Hasan, Science **349**, 613 (2015), https://science.sciencemag.org/content/349/6248/613.full.pdf .

[43] R. C. Xiao, P. L. Gong, Q. S. Wu, W. J. Lu, M. J. Wei, J. Y. Li, H. Y. Lv, X. Luo, P. Tong, X. B. Zhu, and Y. P. Sun, Phys. Rev. B **96**, 075101 (2017).

[44] F. Fei, X. Bo, R. Wang, B. Wu, J. Jiang, D. Fu, M. Gao, H. Zheng, Y. Chen, X. Wang, H. Bu, F. Song, X. Wan, B. Wang, and G. Wang, Phys. Rev. B **96**, 041201 (2017).

[45] H.-J. Noh, J. Jeong, E.-J. Cho, K. Kim, B. I. Min, and B.-G. Park, Phys. Rev. Lett. **119**, 016401 (2017).

[46] M. Yan, H. Huang, K. Zhang, E. Wang, W. Yao, K. Deng, G. Wan, H. Zhang, M. Arita, H. Yang, Z. Sun, H. Yao, Y. Wu, S. Fan, W. Duan, and S. Zhou, Nature Communications **8**, 257 (2017).

[47] K. Deng, G. Wan, P. Deng, K. Zhang, S. Ding, E. Wang, M. Yan, H. Huang, H. Zhang, Z. Xu, J. Denlinger, A. Fedorov, H. Yang, W. Duan, H. Yao, Y. Wu, S. Fan, H. Zhang, X. Chen, and S. Zhou, Nature Physics **12**, 1105 EP (2016).

[48] K. Koepernik, D. Kasinathan, D. V. Efremov, S. Khim, S. Borisenko, B. Büchner, and J. van den Brink, Phys. Rev. B **93**, 201101 (2016).

[49] T. E. O'Brien, M. Diez, and C. W. J. Beenakker, Phys. Rev. Lett. **116**, 236401 (2016).

[50] M. Udagawa and E. J. Bergholtz, Phys. Rev. Lett. **117**, 086401 (2016).

[51] A. A. Soluyanov, D. Gresch, Z. Wang, Q. Wu, M. Troyer, X. Dai, and B. A. Bernevig, Nature **527**, 495 EP (2015).

[52] H. Yi, Z. Wang, C. Chen, Y. Shi, Y. Feng, A. Liang, Z. Xie, S. He, J. He, Y. Peng, X. Liu, Y. Liu, L. Zhao, G. Liu, X. Dong, J. Zhang, M. Nakatake, M. Arita, K. Shimada, H. Namatame, M. Taniguchi, Z. Xu, C. Chen, X. Dai, Z. Fang, and X. J. Zhou, Scientific Reports **4**, 6106 EP (2014), article.

[53] C. Zhang, A. Narayan, S. Lu, J. Zhang, H. Zhang, Z. Ni, X. Yuan, Y. Liu, J.-H. Park, E. Zhang, W. Wang, S. Liu, L. Cheng, L. Pi, Z. Sheng, S. Sanvito, and F. Xiu, Nature Communications **8**, 1272 (2017).

[54] P. Li, Y. Wen, X. He, Q. Zhang, C. Xia, Z.-M. Yu, S. A. Yang, Z. Zhu, H. N. Alshareef, and X.-X. Zhang, Nature Communications **8**, 2150 (2017).

[55] W. Gao, N. Hao, F.-W. Zheng, W. Ning, M. Wu, X. Zhu, G. Zheng, J. Zhang, J. Lu, H. Zhang, C. Xi, J. Yang, H. Du, P. Zhang, Y. Zhang, and M. Tian, Phys. Rev. Lett. **118**, 256601 (2017).

[56] M. N. Ali, J. Xiong, S. Flynn, J. Tao, Q. D. Gibson, L. M. Schoop, T. Liang, N. Haldolaarachchige, M. Hirschberger, N. P. Ong, and R. J. Cava, Nature **514**, 205 EP (2014).

[57] M. M. Parish and P. B. Littlewood, Nature **426**, 162 (2003).

[58] A. A. Abrikosov, Phys. Rev. B **58**, 2788 (1998).

[59] S. L. Adler, Phys. Rev. **177**, 2426 (1969).

[60] J. S. Bell and R. Jackiw, Il Nuovo Cimento A (1965-1970) **60**, 47 (1969).

[61] H.-J. Kim, K.-S. Kim, J.-F. Wang, M. Sasaki, N. Satoh, A. Ohnishi, M. Kitaura, M. Yang, and L. Li, Phys. Rev. Lett. **111**, 246603 (2013).

[62] Q. Li, D. E. Kharzeev, C. Zhang, Y. Huang, I. Pletikosic, A. . V. Fedorov, R. . D. Zhong, J. . A. Schneeloch, G. . D. Gu, and T. Valla, Nature Physics **12**, 550 EP (2016).

[63] Z. Wang, Y. Zheng, Z. Shen, Y. Lu, H. Fang, F. Sheng, Y. Zhou, X. Yang, Y. Li, C. Feng, and Z.-A. Xu, Phys. Rev. B **93**, 121112 (2016).

[64] J. Xiong, S. K. Kushwaha, T. Liang, J. W. Krizan, M. Hirschberger, W. Wang, R. J. Cava, and N. P. Ong, Science **350**, 413 (2015).

[65] S. Nandy, G. Sharma, A. Taraphder, and S. Tewari, Phys. Rev. Lett. **119**, 176804 (2017).

[66] S. R. Elliott and M. Franz, Rev. Mod. Phys. **87**, 137 (2015).

[67] J. Alicea, Reports on Progress in Physics **75**, 076501 (2012).

[68] E. Majorana, Il Nuovo Cimento (1924-1942) **14**, 171 (2008).

[69] N. Read and D. Green, Phys. Rev. B **61**, 10267 (2000).

[70] G. E. Volovik, Journal of Experimental and Theoretical Physics Letters **70**, 609 (1999).

[71] C. Kallin and A. J. Berlinsky, Journal of Physics: Condensed Matter **21**, 164210 (2009).

[72] L. Fu and C. L. Kane, Phys. Rev. Lett. **100**, 096407 (2008).

[73] L. Fu and C. L. Kane, Phys. Rev. B **79**, 161408 (2009).

[74] J. R. Williams, A. J. Bestwick, P. Gallagher, S. S. Hong, Y. Cui, A. S. Bleich, J. G. Analytis, I. R. Fisher, and D. Goldhaber-Gordon, Phys. Rev. Lett. **109**, 056803 (2012).

[75] M. Kriener, K. Segawa, Z. Ren, S. Sasaki, and Y. Ando, Phys. Rev. Lett. **106**, 127004 (2011).

[76] T. Asaba, B. J. Lawson, C. Tinsman, L. Chen, P. Corbae, G. Li, Y. Qiu, Y. S. Hor, L. Fu, and L. Li, Phys. Rev. X **7**, 011009 (2017).

[77] A. S. Erickson, J.-H. Chu, M. F. Toney, T. H. Geballe, and I. R. Fisher, Phys. Rev. B **79**, 024520 (2009).

[78] J. L. Zhang, S. J. Zhang, H. M. Weng, W. Zhang, L. X. Yang, Q. Q. Liu, S. M. Feng, X. C. Wang, R. C. Yu, L. Z. Cao, L. Wang, W. G. Yang, H. Z. Liu, W. Y. Zhao, S. C. Zhang, X. Dai, Z. Fang, and C. Q. Jin, Proceedings of the National Academy of Sciences **108**, 24 (2011), https://www.pnas.org/content/108/1/24.full.pdf .

[79] H.-J. Kwon, V. M. Yakovenko, and K. Sengupta, Low Temperature Physics **30**, 613 (2004), https://doi.org/10.1063/1.1789931 .

[80] L. Fu, Phys. Rev. Lett. **104**, 056402 (2010).

[81] K. T. Law, P. A. Lee, and T. K. Ng, Phys. Rev. Lett. **103**, 237001 (2009).

[82] I. C. Fulga, A. R. Akhmerov, J. Tworzydło, B. Béri, and C. W. J. Beenakker, Phys. Rev. B **86**, 054505 (2012).

[83] G. Dhanaraj, K. Byrappa, V. Prasad, and M. Dudley, *Springer handbook of crystal growth* (Springer Science & Business Media, 2010).

[84] B. D. Cullity and S. R. Stock, *Elements of X-ray Diffraction*, Vol. 3 (Prentice hall New Jersey, 2001).

[85] A. Larson and R. Von Dreele, Los Alamos National Laborator Report LAUR , 86 (1994).

[86] Y. Liu and R. E. Allen, Phys. Rev. B **52**, 1566 (1995).

[87] B. Lenoir, M. Cassart, J.-P. Michenaud, H. Scherrer, and S. Scherrer, Journal of Physics and Chemistry of Solids **57**, 89 (1996).

[88] D. Shin, Y. Lee, M. Sasaki, Y. H. Jeong, F. Weickert, J. B. Betts, H.-J. Kim, K.-S. Kim, and J. Kim, Nature Materials **16**, 1096 EP (2017).

[89] Y.-H. Su, W. Shi, C. Felser, and Y. Sun, Phys. Rev. B **97**, 155431 (2018).

[90] Z. J. Yue, X. L. Wang, and S. S. Yan, Applied Physics Letters **107**, 112101 (2015).

[91] D. Hsieh, Y. Xia, L. Wray, D. Qian, A. Pal, J. H. Dil, J. Osterwalder, F. Meier, G. Bihlmayer, C. L. Kane, Y. S. Hor, R. J. Cava, and M. Z. Hasan, Science **323**, 919 (2009).

[92] J. G. Analytis, R. D. McDonald, S. C. Riggs, J.-H. Chu, G. S. Boebinger, and I. R. Fisher, Nature Physics **6**, 960 EP (2010).

[93] D. Shoenberg, *Magnetic oscillations in metals* (Cambridge university press, 2009).

[94] M. Z. Hasan, Physics **3**, 62 (2010).

[95] L. Onsager, The London, Edinburgh, and Dublin Philosophical Magazine and Journal of Science **43**, 1006 (1952).

[96] H. Murakawa, M. S. Bahramy, M. Tokunaga, Y. Kohama, C. Bell, Y. Kaneko, N. Nagaosa, H. Y. Hwang, and Y. Tokura, Science **342**, 1490 (2013).

[97] Z. Ren, A. A. Taskin, S. Sasaki, K. Segawa, and Y. Ando, Phys. Rev. B **85**, 155301 (2012).

[98] Z. Ren, A. A. Taskin, S. Sasaki, K. Segawa, and Y. Ando, Phys. Rev. B **82**, 241306 (2010).

[99] D.-X. Qu, Y. S. Hor, J. Xiong, R. J. Cava, and N. P. Ong, Science **329**, 821 (2010).

[100] A. A. Taskin and Y. Ando, Phys. Rev. B **84**, 035301 (2011).

[101] R. C. Xiao, C. H. Cheung, P. L. Gong, W. J. Lu, J. G. Si, and Y. P. Sun, Journal of Physics: Condensed Matter **30**, 245502 (2018).

[102] O. J. Clark, M. J. Neat, K. Okawa, L. Bawden, I. Marković, F. Mazzola, J. Feng, V. Sunko, J. M. Riley, W. Meevasana, J. Fujii, I. Vobornik, T. K. Kim, M. Hoesch, T. Sasagawa, P. Wahl, M. S. Bahramy, and P. D. C. King, Phys. Rev. Lett. **120**, 156401 (2018).

[103] Y. Xu, F. Zhang, and C. Zhang, Phys. Rev. Lett. **115**, 265304 (2015).

[104] M. . S. Bahramy, O. . J. Clark, B.-J. Yang, J. Feng, L. Bawden, J. . M. Riley, I. Markovic, F. Mazzola, V. Sunko, D. Biswas, S. . P. Cooil, M. Jorge, J. . W. Wells, M. Leandersson, T. Balasubramanian, J. Fujii, I. Vobornik, J. E. Rault, T. . K. Kim,

M. Hoesch, K. Okawa, M. Asakawa, T. Sasagawa, T. Eknapakul, W. Meevasana, and P. . D. . C. King, Nature Materials **17**, 21 EP (2017), article.

[105] Y. Li, Y. Xia, S. A. Ekahana, N. Kumar, J. Jiang, L. Yang, C. Chen, C. Liu, B. Yan, C. Felser, G. Li, Z. Liu, and Y. Chen, Phys. Rev. Materials **1**, 074202 (2017).

[106] S. Borisenko, Q. Gibson, D. Evtushinsky, V. Zabolotnyy, B. Büchner, and R. J. Cava, Phys. Rev. Lett. **113**, 027603 (2014).

[107] K. Zhao, E. Golias, Q. H. Zhang, M. Krivenkov, A. Jesche, L. Gu, O. Rader, I. I. Mazin, and P. Gegenwart, Phys. Rev. B **97**, 115166 (2018).

[108] J. Gooth, A. C. Niemann, T. Meng, A. G. Grushin, K. Landsteiner, B. Gotsmann, F. Menges, M. Schmidt, C. Shekhar, V. Süß, R. Hühne, B. Rellinghaus, C. Felser, B. Yan, and K. Nielsch, Nature **547**, 324 EP (2017).

[109] N. Kumar, K. Manna, Y. Qi, S.-C. Wu, L. Wang, B. Yan, C. Felser, and C. Shekhar, Phys. Rev. B **95**, 121109 (2017).

[110] J. Hu, Z. Tang, J. Liu, X. Liu, Y. Zhu, D. Graf, K. Myhro, S. Tran, C. N. Lau, J. Wei, and Z. Mao, Phys. Rev. Lett. **117**, 016602 (2016).

[111] S. Huang, J. Kim, W. A. Shelton, E. W. Plummer, and R. Jin, Proceedings of the National Academy of Sciences **114**, 6256 (2017), https://www.pnas.org/content/114/24/6256.full.pdf .

[112] J. Hu, Y. Zhu, X. Gui, D. Graf, Z. Tang, W. Xie, and Z. Mao, Phys. Rev. B **97**, 155101 (2018).

[113] N. Nagaosa, J. Sinova, S. Onoda, A. H. MacDonald, and N. P. Ong, Rev. Mod. Phys. **82**, 1539 (2010).

[114] C.-Z. Chang, J. Zhang, X. Feng, J. Shen, Z. Zhang, M. Guo, K. Li, Y. Ou, P. Wei, L.-L. Wang, Z.-Q. Ji, Y. Feng, S. Ji, X. Chen, J. Jia, X. Dai, Z. Fang, S.-C. Zhang, K. He, Y. Wang, L. Lu, X.-C. Ma, and Q.-K. Xue, Science **340**, 167 (2013).

[115] X.-L. Qi and S.-C. Zhang, arXiv preprint arXiv:1001.1602 (2010).

[116] A. A. Zyuzin and A. A. Burkov, Phys. Rev. B **86**, 115133 (2012).

[117] M. Hirschberger, S. Kushwaha, Z. Wang, Q. Gibson, S. Liang, C. Belvin, B. . A. Bernevig, R. . J. Cava, and N. . P. Ong, Nature Materials **15**, 1161 EP (2016).

[118] Y. J. Wang, J. X. Gong, D. D. Liang, M. Ge, J. R. Wang, W. K. Zhu, and C. J. Zhang, "Planar hall effect in type-ii weyl semimetal wte2," (2018), arXiv:1801.05929 .

[119] H. Li, H.-W. Wang, H. He, J. Wang, and S.-Q. Shen, Phys. Rev. B **97**, 201110 (2018).

[120] M. Wu, G. Zheng, W. Chu, Y. Liu, W. Gao, H. Zhang, J. Lu, Y. Han, J. Zhou, W. Ning, and M. Tian, Phys. Rev. B **98**, 161110 (2018).

[121] N. Kumar, S. N. Guin, C. Felser, and C. Shekhar, Phys. Rev. B **98**, 041103 (2018).

[122] P. Li, C. Zhang, J. Zhang, Y. Wen, and X. Zhang, Physical Review B **98**, 121108 (2018).

[123] R. Singha, S. Roy, A. Pariari, B. Satpati, and P. Mandal, Phys. Rev. B **98**, 081103 (2018).

[124] R. Gopal, Y. Singh, *et al.*, arXiv preprint arXiv:1810.04867 (2018).

[125] H. X. Tang, R. K. Kawakami, D. D. Awschalom, and M. L. Roukes, Phys. Rev. Lett. **90**, 107201 (2003).

[126] D. Y. Shin, S. J. Chung, S. Lee, X. Liu, and J. K. Furdyna, Phys. Rev. B **76**, 035327 (2007).

[127] T. Liang, J. Lin, Q. Gibson, S. Kushwaha, M. Liu, W. Wang, H. Xiong, J. A. Sobota, M. Hashimoto, P. S. Kirchmann, Z.-X. Shen, R. J. Cava, and N. P. Ong, Nature Physics **14**, 451 (2018).

[128] Q. Li, D. E. Kharzeev, C. Zhang, Y. Huang, I. Pletikosić, A. Fedorov, R. Zhong, J. Schneeloch, G. Gu, and T. Valla, Nature Physics **12**, 550 (2016).

[129] F. Arnold, C. Shekhar, S.-C. Wu, Y. Sun, R. D. Dos Reis, N. Kumar, M. Naumann, M. O. Ajeesh, M. Schmidt, A. G. Grushin, *et al.*, Nature communications **7**, 11615 (2016).

[130] R. Dos Reis, M. Ajeesh, N. Kumar, F. Arnold, C. Shekhar, M. Naumann, M. Schmidt, M. Nicklas, and E. Hassinger, New Journal of Physics **18**, 085006 (2016).

[131] C.-L. Zhang, S.-Y. Xu, I. Belopolski, Z. Yuan, Z. Lin, B. Tong, G. Bian, N. Alidoust, C.-C. Lee, S.-M. Huang, T.-R. Chang, G. Chang, C.-H. Hsu, H.-T. Jeng,

M. Neupane, D. S. Sanchez, H. Zheng, J. Wang, H. Lin, C. Zhang, H.-Z. Lu, S.-Q. Shen, T. Neupert, M. Zahid Hasan, and S. Jia, Nature Communications **7**, 10735 EP (2016), article.

[132] J. Yang, W. L. Zhen, D. D. Liang, Y. J. Wang, X. Yan, S. R. Weng, J. R. Wang, W. Tong, L. Pi, W. K. Zhu, and C. J. Zhang, "Giant planar hall effect survives in a weyl semimetal with ultrahigh mobility and current jetting," (2018), arXiv:1807.06229 .

[133] D. Kim, P. Syers, N. P. Butch, J. Paglione, and M. S. Fuhrer, Nature Communications **4**, 2040 EP (2013), article.

[134] N. Bansal, Y. S. Kim, M. Brahlek, E. Edrey, and S. Oh, Phys. Rev. Lett. **109**, 116804 (2012).

[135] A. A. Taskin, S. Sasaki, K. Segawa, and Y. Ando, Phys. Rev. Lett. **109**, 066803 (2012).

[136] W. Zheng, R. Schönemann, N. Aryal, Q. Zhou, D. Rhodes, Y.-C. Chiu, K.-W. Chen, E. Kampert, T. Förster, T. J. Martin, G. T. McCandless, J. Y. Chan, E. Manousakis, and L. Balicas, Phys. Rev. B **97**, 235154 (2018).

[137] T. Tsuchida and W. E. Wallace, The Journal of Chemical Physics **43**, 2087 (1965), https://doi.org/10.1063/1.1697079 .

[138] N. Nereson and G. Arnold, Journal of Applied Physics **42**, 1625 (1971), https://doi.org/10.1063/1.1660369 .

[139] F. F. Tafti, Q. D. Gibson, S. K. Kushwaha, N. Haldolaarachchige, and R. J. Cava, Nature Physics **12**, 272 EP (2015), article.

[140] L.-K. Zeng, R. Lou, D.-S. Wu, Q. N. Xu, P.-J. Guo, L.-Y. Kong, Y.-G. Zhong, J.-Z. Ma, B.-B. Fu, P. Richard, P. Wang, G. T. Liu, L. Lu, Y.-B. Huang, C. Fang, S.-S. Sun, Q. Wang, L. Wang, Y.-G. Shi, H. M. Weng, H.-C. Lei, K. Liu, S.-C. Wang, T. Qian, J.-L. Luo, and H. Ding, Phys. Rev. Lett. **117**, 127204 (2016).

[141] N. Kumar, C. Shekhar, S.-C. Wu, I. Leermakers, O. Young, U. Zeitler, B. Yan, and C. Felser, Phys. Rev. B **93**, 241106 (2016).

[142] N. Wakeham, E. D. Bauer, M. Neupane, and F. Ronning, Phys. Rev. B **93**, 205152 (2016).

[143] F. Wu, C. Y. Guo, M. Smidman, J. L. Zhang, and H. Q. Yuan, Phys. Rev. B **96**, 125122 (2017).

[144] S. Sun, Q. Wang, P.-J. Guo, K. Liu, and H. Lei, New Journal of Physics **18**, 082002 (2016).

[145] J. Nayak, S.-C. Wu, N. Kumar, C. Shekhar, S. Singh, J. Fink, E. E. D. Rienks, G. H. Fecher, S. S. P. Parkin, B. Yan, and C. Felser, Nature Communications **8**, 13942 EP (2017), article.

[146] B. Feng, J. Cao, M. Yang, Y. Feng, S. Wu, B. Fu, M. Arita, K. Miyamoto, S. He, K. Shimada, Y. Shi, T. Okuda, and Y. Yao, Phys. Rev. B **97**, 155153 (2018).

[147] H.-Y. Yang, T. Nummy, H. Li, S. Jaszewski, M. Abramchuk, D. S. Dessau, and F. Tafti, Phys. Rev. B **96**, 235128 (2017).

[148] Y. J. Hu, E. I. P. Aulestia, K. F. Tse, C. N. Kuo, J. Y. Zhu, C. S. Lue, K. T. Lai, and S. K. Goh, Phys. Rev. B **98**, 035133 (2018).

[149] J. Xu, N. J. Ghimire, J. S. Jiang, Z. L. Xiao, A. S. Botana, Y. L. Wang, Y. Hao, J. E. Pearson, and W. K. Kwok, Phys. Rev. B **96**, 075159 (2017).

[150] Y.-Y. Wang, H. Zhang, X.-Q. Lu, L.-L. Sun, S. Xu, Z.-Y. Lu, K. Liu, S. Zhou, and T.-L. Xia, Phys. Rev. B **97**, 085137 (2018).

[151] O. Pavlosiuk, P. Swatek, D. Kaczorowski, and P. Wiśniewski, Phys. Rev. B **97**, 235132 (2018).

[152] P. Li, Z. Wu, F. Wu, C. Cao, C. Guo, Y. Wu, Y. Liu, Z. Sun, C.-M. Cheng, D.-S. Lin, F. Steglich, H. Yuan, T.-C. Chiang, and Y. Liu, Phys. Rev. B **98**, 085103 (2018).

[153] T. Tsuchida and W. E. Wallace, The Journal of Chemical Physics **43**, 2087 (1965), https://doi.org/10.1063/1.1697079 .

[154] T. Tsuchida and W. E. Wallace, The Journal of Chemical Physics **43**, 2885 (1965), https://doi.org/10.1063/1.1697221 .

[155] F. F. Tafti, Q. D. Gibson, S. K. Kushwaha, N. Haldolaarachchige, and R. J. Cava, Nature Physics **12**, 272 EP (2015), article.

[156] Y. Zhao, H. Liu, J. Yan, W. An, J. Liu, X. Zhang, H. Wang, Y. Liu, H. Jiang, Q. Li, Y. Wang, X.-Z. Li, D. Mandrus, X. C. Xie, M. Pan, and J. Wang, Phys. Rev. B **92**, 041104 (2015).

[157] Y. L. Wang, L. R. Thoutam, Z. L. Xiao, J. Hu, S. Das, Z. Q. Mao, J. Wei, R. Divan, A. Luican-Mayer, G. W. Crabtree, and W. K. Kwok, Phys. Rev. B **92**, 180402 (2015).

[158] R. Singha, B. Satpati, and P. Mandal, Scientific Reports **7**, 6321 (2017).

[159] S. Sun, Q. Wang, P.-J. Guo, K. Liu, and H. Lei, New Journal of Physics **18**, 082002 (2016).

[160] N. Kumar, C. Shekhar, S.-C. Wu, I. Leermakers, O. Young, U. Zeitler, B. Yan, and C. Felser, Phys. Rev. B **93**, 241106 (2016).

[161] C. Shekhar, A. K. Nayak, Y. Sun, M. Schmidt, M. Nicklas, I. Leermakers, U. Zeitler, Y. Skourski, J. Wosnitza, Z. Liu, Y. Chen, W. Schnelle, H. Borrmann, Y. Grin, C. Felser, and B. Yan, Nature Physics **11**, 645 EP (2015).

[162] C.-L. Zhang, Z. Yuan, Q.-D. Jiang, B. Tong, C. Zhang, X. C. Xie, and S. Jia, Phys. Rev. B **95**, 085202 (2017).

[163] Y.-Y. Wang, H. Zhang, X.-Q. Lu, L.-L. Sun, S. Xu, Z.-Y. Lu, K. Liu, S. Zhou, and T.-L. Xia, Phys. Rev. B **97**, 085137 (2018).

[164] S. Nimori, G. Kido, D. Li, and T. Suzuki, Physica B: Condensed Matter **211**, 148 (1995), research in High Magnetic Fields.

[165] L. Ye, T. Suzuki, C. R. Wicker, and J. G. Checkelsky, Phys. Rev. B **97**, 081108 (2018).

[166] P. Monachesi, Z. Domański, and M. S. S. Brooks, Phys. Rev. B **50**, 1013 (1994).

[167] T. Liang, Q. Gibson, M. N. Ali, M. Liu, R. Cava, and N. Ong, Nature materials **14**, 280 (2015).

[168] C. M. Hurd, **The Hall Effect in Metals and Alloys (Plenum Press, 1972), New York**.

[169] P. Giannozzi, O. Andreussi, T. Brumme, O. Bunau, M. B. Nardelli, M. Calandra, R. Car, C. Cavazzoni, D. Ceresoli, M. Cococcioni, N. Colonna, I. Carnimeo, A. D. Corso, S. de Gironcoli, P. Delugas, R. A. DiStasio, A. Ferretti, A. Floris, G. Fratesi, G. Fugallo, R. Gebauer, U. Gerstmann, F. Giustino, T. Gorni, J. Jia, M. Kawamura, H.-Y. Ko, A. Kokalj, E. Küçükbenli, M. Lazzeri, M. Marsili, N. Marzari, F. Mauri, N. L. Nguyen, H.-V. Nguyen, A. O. de-la Roza, L. Paulatto, S. Poncé,

D. Rocca, R. Sabatini, B. Santra, M. Schlipf, A. P. Seitsonen, A. Smogunov, I. Timrov, T. Thonhauser, P. Umari, N. Vast, X. Wu, and S. Baroni, Journal of Physics: Condensed Matter **29**, 465901 (2017).

[170] P. Giannozzi, S. Baroni, N. Bonini, M. Calandra, R. Car, C. Cavazzoni, D. Ceresoli, G. L. Chiarotti, M. Cococcioni, I. Dabo, A. D. Corso, S. de Gironcoli, S. Fabris, G. Fratesi, R. Gebauer, U. Gerstmann, C. Gougoussis, A. Kokalj, M. Lazzeri, L. Martin-Samos, N. Marzari, F. Mauri, R. Mazzarello, S. Paolini, A. Pasquarello, L. Paulatto, C. Sbraccia, S. Scandolo, G. Sclauzero, A. P. Seitsonen, A. Smogunov, P. Umari, and R. M. Wentzcovitch, Journal of Physics: Condensed Matter **21**, 395502 (2009).

[171] J. P. Perdew, K. Burke, and M. Ernzerhof, Phys. Rev. Lett. **77**, 3865 (1996).

[172] A. Kokalj, Computational Materials Science **28**, 155 (2003), proceedings of the Symposium on Software Development for Process and Materials Design.

[173] A. A. Mostofi, J. R. Yates, G. Pizzi, Y.-S. Lee, I. Souza, D. Vanderbilt, and N. Marzari, Computer Physics Communications **185**, 2309 (2014).

[174] P. Rourke and S. Julian, Computer Physics Communications **183**, 324 (2012).

[175] P. Li, Z. Wu, F. Wu, C. Cao, C. Guo, Y. Wu, Y. Liu, Z. Sun, C.-M. Cheng, D.-S. Lin, F. Steglich, H. Yuan, T.-C. Chiang, and Y. Liu, Phys. Rev. B **98**, 085103 (2018).

[176] S. Sasaki, K. Segawa, and Y. Ando, Phys. Rev. B **90**, 220504 (2014).

[177] J. D. Sau, R. M. Lutchyn, S. Tewari, and S. Das Sarma, Phys. Rev. Lett. **104**, 040502 (2010).

[178] J. Guggenheim, F. Hulliger, and J. Muller, Helv Phys Acta **34**, 408 (1961).

[179] Y. Liu, J.-Z. Zhao, L. Yu, C.-T. Lin, C. Hu, D.-F. Liu, Y.-Y. Peng, Z.-J. Xie, J.-F. He, C.-Y. Chen, Y. Feng, H.-M. Yi, X. Liu, L. Zhao, S.-L. He, G.-D. Liu, X.-L. Dong, J. Zhang, C.-T. Chen, Z.-Y. Xu, H.-M. Weng, X. Dai, Z. Fang, and X.-J. Zhou, Chinese Physics B **24**, 067401 (2015).

[180] Amit, R. K. Singh, N. Wadehra, S. Chakraverty, and Y. Singh, Phys. Rev. Materials **2**, 114202 (2018).

[181] G. Bednik, A. A. Zyuzin, and A. A. Burkov, Phys. Rev. B **92**, 035153 (2015).

[182] T. Hashimoto, S. Kobayashi, Y. Tanaka, and M. Sato, Phys. Rev. B **94**, 014510 (2016).

[183] M. Alidoust, K. Halterman, and A. A. Zyuzin, Phys. Rev. B **95**, 155124 (2017).

[184] H. Leng, C. Paulsen, Y. K. Huang, and A. de Visser, Phys. Rev. B **96**, 220506 (2017).

[185] S. Das, Amit, A. Sirohi, L. Yadav, S. Gayen, Y. Singh, and G. Sheet, Phys. Rev. B **97**, 014523 (2018).

[186] A. Sirohi, S. Das, P. Adhikary, R. R. Chowdhury, A. Vashist, Y. Singh, S. Gayen, T. Das, and G. Sheet, Journal of Physics: Condensed Matter **31**, 085701 (2019).

[187] M. V. Salis, P. Rodière, H. Leng, Y. K. Huang, and A. de Visser, Journal of Physics: Condensed Matter **30**, 505602 (2018).

[188] G. Volovik, JETP LETTERS C/C OF PIS'MA V ZHURNAL EKSPERIMENTAL'NOI TEORETICHESKOI FIZIKI **58**, 469 (1993).

[189] L. Fu and E. Berg, Phys. Rev. Lett. **105**, 097001 (2010).

[190] L. A. Wray, S.-Y. Xu, Y. Xia, Y. S. Hor, D. Qian, A. V. Fedorov, H. Lin, A. Bansil, R. J. Cava, and M. Z. Hasan, Nature Physics **6**, 855 (2010).

[191] Y. S. Hor, A. J. Williams, J. G. Checkelsky, P. Roushan, J. Seo, Q. Xu, H. W. Zandbergen, A. Yazdani, N. P. Ong, and R. J. Cava, Phys. Rev. Lett. **104**, 057001 (2010).

[192] Z. Liu, X. Yao, J. Shao, M. Zuo, L. Pi, S. Tan, C. Zhang, and Y. Zhang, Journal of the American Chemical Society **137**, 10512 (2015), pMID: 26262431, https://doi.org/10.1021/jacs.5b06815 .

[193] J. Shen, W.-Y. He, N. F. Q. Yuan, Z. Huang, C.-w. Cho, S. H. Lee, Y. S. Hor, K. T. Law, and R. Lortz, npj Quantum Materials **2**, 59 (2017).

[194] Y. Hor, J. Checkelsky, D. Qu, N. Ong, and R. Cava, Journal of Physics and Chemistry of Solids **72**, 572 (2011), spectroscopies in Novel Superconductors 2010.

[195] E. Morosan, H. W. Zandbergen, B. S. Dennis, J. W. G. Bos, Y. Onose, T. Klimczuk, A. P. Ramirez, N. P. Ong, and R. J. Cava, Nature Physics **2**, 544 (2006).

[196] M. A. y de Dompablo, E. Morán, M. Alario-Franco, F. Drymiotis, A. Bianchi, and Z. Fisk, International Journal of Inorganic Materials **2**, 581 (2000), dedicated to Prof Raveau on the occasion of his 60th Birthday.

[197] W. L. McMillan, Phys. Rev. **167**, 331 (1968).

[198] P. B. Allen and R. C. Dynes, Phys. Rev. B **12**, 905 (1975).

[199] A. Eiling and J. S. Schilling, Journal of Physics F: Metal Physics **11**, 623 (1981).

[200] Zavaritsky, V. N., Kabanov, V. V., and Alexandrov, A. S., Europhys. Lett. **60**, 127 (2002).

[201] M. Maple, M. C. de Andrade, J. Herrmann, R. P. Dickey, N. R. Dilley, and S. Han, Journal of Alloys and Compounds **250**, 585 (1997).

[202] Z. X. Shi, M. Tokunaga, T. Tamegai, Y. Takano, K. Togano, H. Kito, and H. Ihara, Phys. Rev. B **68**, 104513 (2003).

[203] S. Deemyad, J. Schilling, J. Jorgensen, and D. Hinks, Physica C: Superconductivity **361**, 227 (2001).